ISSN 2222-5617

МІНІСТЕРСТВО ОСВІТИ І НАУКИ УКРАЇНИ

Вісник Харківського Національного Університету імені В.Н.Каразіна

Серія “Фізика”

Випуск 24

Серія започаткована 1998 р.

Харків 2016

УДК 530.1/539.8

Вісник містить статті, присвячені сучасному стану теоретичних та експериментальних досліджень у галузі фізики Видання призначене для науковців, викладачів, аспірантів та студентів фізичних спеціальностей вищих навчальних закладів та наукових установ.
Видання є фаховим у галузі фіз.-мат. наук (фізика) наказ МОН України №1328 від 21.12.2015.

Затверджено до друку рішенням Вченої ради Харківського національного університету імені В.Н.Каразіна (протокол №1 від 23 січня 2017 р.)

Адреса редакції:
Україна, 61022, Харків, майдан Свободи, 4, Харківський національний університет імені В.Н. Каразіна, фізичний факультет, 057-707-53-83, ruslan.v.vovk@univer.kharkov.ua
Статті пройшли внутрішнє та зовнішнє рецензування.

Свідоцтво про державну реєстрацію КВ №21573-11473Р від 20.08.2015

UDC 530.1/539.8

Bulletin contains articles on the current state of theoretical and experimental research in the field of physics.
The publication is intended for researchers, teachers and students of physical specialties of higher education and research institutions.
The publication is a professional in the field of physics and mathematics science (Physics) ordered MES of Ukraine #1328 from 12.21.2015.

Approved for publication by the decision of the Academic Council of Kharkiv Karazin National University. (Minutes №1 dated January 23, 2017 p.)

Editorial address:

Svobody Sq. 4, 61022, Kharkiv, Ukraine, V.N. Karazin Kharkiv National University, Department of Physics, 057-707-53-83, ruslan.v.vovk@univer.kharkov.ua

All articles reviewed.

Certificate of registration КВ number 21573-11473P on 20.08.2015

Content

Зміст

Вісник ХНУ, серія «Фізика», вип. 24, 2016. с. 6-16

PACS: 74.72.-h Cuprate superconductors.
УДК 538.945+537.312.62

Normal and longitudinal electronic transport of HTS compounds $ReBa_2Cu_3O_{7-\delta}$ (Re = Y or lanthanides) under extreme exposure

K.A. Kotvytska, S.R. Vovk, I. M. Chursina, R.V. Vovk

V.N. Karazin Kharkiv National University, 4 Freedom Square, Kharkiv, 61022, Ukraine

Large part of the theoretical and experimental papers, reflecting the current state of research on normal electric HTSC-compounds $ReBa_2Cu_3O_{7-\delta}$ (Re = Y or lanthanides) in extreme impacts are reviewed. We discuss the crystal structure and defects of these compounds, as well as their impact on the various modes of the electrical conductivity of these compounds at low temperatures and high magnetic fields and high pressures. It is shown that the use of such effects can not only verify the adequacy many theoretical models but outline empirical ways to improve the critical parameters of high-temperature superconductors - compounds.

Keywords: YBaCuO single crystals, hydrostatic pressure, excess conductivity, crossover, coherence length, fluctuation conductivity, pseudogap state, high-temperature superconductivity, critical temperature

Наведено огляд значної частини теоретичних і експериментальних робіт, що відображають сучасний стан досліджень нормального електротранспорту ВТНП-сполук $ReBa_2Cu_3O_{7-\delta}$ (Re = Y або лантаноїди) в умовах екстремальних зовнішніх дій. Детально розглянуто кристалічну структура і структурні дефекти цих сполук, а також їх вплив на різні режими електропровідності при низьких температурах, високих магнітних полях і високому тиску. Показано, що застосування таких впливів дозволяє не тільки перевірити адекватність численних теоретичних моделей, але і окреслити емпіричні шляхи підвищення критичних параметрів ВТНП - сполук.

Ключові слова: монокристали YBaCuO, допування, гідростатичний тиск, надлишкова провідність, кросовер, флуктуаційна провідність, псевдощілинний стан, високотемпературна надпровідність, критична температура

Приведен обзор значительной части теоретических и экспериментальных работ, отражающих современное состояние исследований нормального электротранспорта ВТСП-соединений $ReBa_2Cu_3O_{7-\delta}$ (Re = Y или лантаноиды) в условиях экстремальных воздействий. Детально рассмотрена кристаллическая структура и структурные дефекты этих соединений, а также их влияние на различные режимы электропроводности при низких температурах, высоких магнитных полях и высоких давлениях. Показано, что применение таких воздействий позволяет не только проверить адекватность многочисленных теоретических моделей, но и очертить эмпирические пути повышения критических параметров ВТСП - соединений.

Ключевые слова: монокристаллы YBaCuO, допирование, гидростатическое давление, избыточная проводимость, кроссовер, флуктуационная проводимость, псевдощелевое состояние, ввысокотемпературная сверхпроводимость, критическая температура

2016 marked 30 years since the discovery of the high-temperature superconductivity phenomenon (HTS). During this period there have been published thousands of articles and tens of reviews (see, for example, [2-4]). However, there is no unambiguous explanation of the HTS phenomenon for now. There also no explanations of the pseudogapped state phenomenon, Fermi surface structure, linear dependence phenomenon of electrical resistance et cetera [4]. The roles of spin fluctuations in Cooper pairing, electron-phonon coupling in the HTS emergence remain open problems [5-11]. The shortcomings of experimental research consist in uncertified test samples (high defect films or polyphase objects) [3-10]. The problems in the development of an appropriate theoretical model are connected with a proper account for the multiparticle interaction in systems with strong correlations. It was only made clear that the symmetry of d-type superconductivity, gap, is aeolotropic and it has zero values in nodal directions of Brillouin zone, and the superconductive gap is preceded by the pseudogap [2,3]. But its role in the superconductivity state formation has not been clearly determined yet.

1.1 Crystal structure, defects and electronic transport in 1-2-3 HTS system on the basis of yttrium.

1.1.1. Crystal structure of $YBa_2Cu_3O_{7-\delta}$ compound.

The structure and properties of $YBa_2Cu_3O_{7-\delta}$ are directly related to δ index which characterizes the oxygen vacancy content. The compounds are superconductive and have orthorombic symmetry when $\delta < 0.4$ with $YBa_2Cu_3O_7$ interphase. For $\delta > 0.4$ they become semiconductors with $YBa_2Cu_3O_6$ interphase. Their structure can be regarded

as the perovskite structure with the lack of oxygen [12].]. In general case perovskite represents a pack of BO_6 octahedrons where B - small metal cation (for example, copper) surrounded by 6 oxygen ions. Atom positions between 8 octahedrons centered in cube corners are occupied by large cations of A metal (yttrium). Removing oxygen atoms from the ideal lattice of perovskite we obtain the most oxygen-rich $YBa_2Cu_3O_7$ compound (fig.1).

Its unit cell can be presented in the form of layered sequence perpendicular to ***c*** axis: a) Cu – O in which there are two oxygen vacancies in comparison with the initial perovskite; copper ion Cu (1) situated in this layer has coordination number 4 and it is surrounded by four oxygen ions; b) Ba – O; c) Cu – O where copper ion Cu (2) situated in this layer has coordination number 5 and it is surrounded by five oxygen ions forming a polyhedron; d) yttrium layer in which there are four oxygen vacancies in comparison with the initial perovskite. The cell extension is symmetrical relatively to this yttrium ion layer and the Ba-O and Cu-o layers described earlier are repeated again there.

However, copper ions are situated in atom positions of two types: Cu (1) in the plane of CuO_4, and Cu (2) - in the pyramid with the square base of CuO_5. It is the polyhedron layers separated by yttrium ion layers that define the two-dimensional nature of the structure. The presence of cuprate planes, as well as two-dimensional structure and quasi-two-dimensional structure is a common feature of all high temperature superconductive compounds. The bonding force between cuprate layers are usually quantatively expressed in terms of the anisotropy parameter Γ:

$$\Gamma=(\xi_{ab}/\xi_c)^2=(\lambda_c/\lambda_{ab})^2, \quad (1)$$

where ξ_{ab}, ξ_c и λ_c, λ_{ab} - coherence length and penetration depth through the length and breadth of layers, respectively. In this case the anisotropy value varies from $\Gamma > 29$ for ytrrium HTS, to $\Gamma > 3.10^3$ for bismuth and $\Gamma > 10^5$ for thallium compounds.

Neutron diffraction and electron microscopy methods [13] show with a high resolution that oxygen vacancies are situated in the plane of square CuO_4 but not in the pyramids of CuO_5. With increase of vacancy concentration the Cu - O chains along ***b*** axis become completed, and Cu atoms (1) change their coordination number from 4 to 2 for the most oxygen-deficient $YBa_2Cu_3O_6$ compound.

While comparing cubic and rhombohedral structure of perovskite ($LaCuO_3$) with the structures of $YBa_2Cu_3O_7$ and $YBa_2Cu_3O_6$ compounds it turns out that the chains develop in three dimensional directions in perovskite, only in b direction in $YBa_2Cu_3O_7$, and they do not exist in $YBa_2Cu_3O_6$.

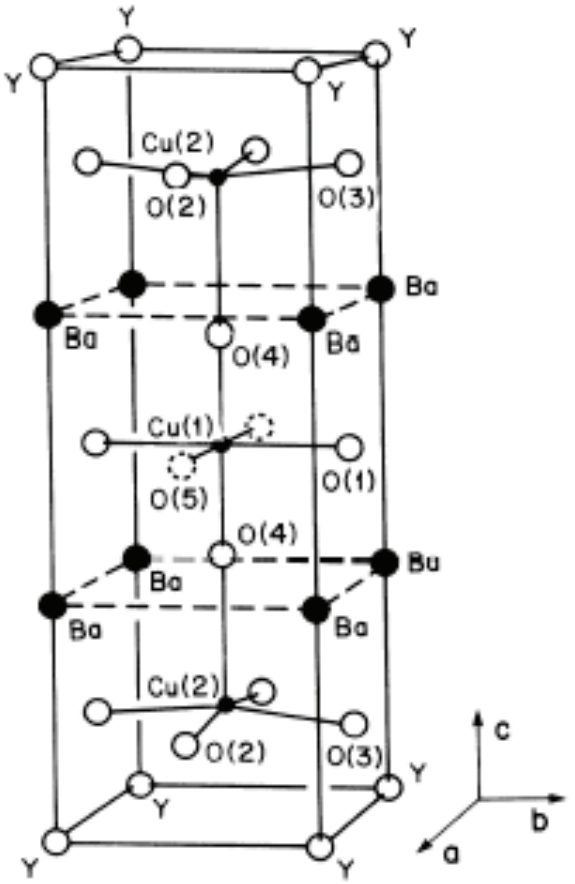

Fig.1 Crystal lattice of $YBa_2Cu_3O_{7-\delta}$ compound according to[12].

1.1.2. Structural defects in $YBa_2Cu_3O_{7-\delta}$ compound. In $YBa_2Cu_3O_{7-\delta}$ pure crystals depending on the oxygen deficit and synthesis technology we observe the following structural defects: point defects as oxygen vacancy defects which are formed in CuO planes, planar defects of (001) type, twin boundaries, dislocations and so called 2√2x2√2 structures [14] observed under oxygen deficit δ = 6.8 - 6.9.

.Planar defects are twin formation planes which are formed under “tetra-ortho” transition and minimize elastic crystal energy. The boundaries of twins represent planes with tetragonal structure as a result of presence of the layers containing oxygen vacancies situated along the twin boundary [14, 15].]. Electronic and microscopic researches showed [15] that in the initial stage of tetra-ortho transition there emerge domain nuclei in which two families of coherent separation surfaces (110) and (110) are formed. This can cause formation of a structure such as “tweed” under overlapping of close micro twins. The period of such structure depends on the oxygen content and can be stimulated by doping with a three-valence metal and, specifically, with aluminium [15,16]. In the initial stage of microdomain formation the formation of separation interface takes place by means of diffusion of structural vacancies in CuO layers. The propagation of interface separation occurs by means of voltage controlled movement of twin dislocations.

Linear defects (dislocations) are rather characteristic

for epitaxially grown films and texture samples. Defects of this type can be caused by imperfect dislocations produced by the support film interface in film samples, and imperfect dislocations produced at the interface of $YBa_2Cu_3O_{7-\delta}$ and $YBa_2Cu_3O_5$ phases in textured melted samples. The dislocation density in films can reach about $1.4\ 10^8$ /cm^2 [17].

High dislocation density in single crystals $YBa_2Cu_3O_{7-\delta}$ can be obtained in a crystal growth during the peritectic reaction [18], which is probably due to small inclusions of $YBa_2Cu_3O_5$ phase. But the dislocation density equals to about $5\ 10^3$/ cm^2 [19] in the crystals grown with the solution-melt method. It should be noted that the dislocation density can be increased under the thermomechanical treatment of materials [20].

Point defects (oxygen vacancies) are present at all $YBa_2Cu_3O_{7-\delta}$ samples, which is due to the nonstoichiometric oxygen content. Besides, the filling factor is close to one for all oxygen positions, except CuO (1). Depending on oxygen content the superstructure formation is possible under the periodic distribution of oxygen vacancies. The density of oxygen vacancies is relatively large and at $\delta = 0.03$ it equals to about 10^{26} /m^3.

In the literature there is also some evidence about copper deficit in CuO planes that can reach the value of 0.09 in compounds [21]. Point defects can also be obtained under doping. As a rule, doping elements (except rare-earth elements and Sr) embed in Cu positions (1) [6]. But the ions of rare-earth metals and K replace ytrrium atoms, and Sr embed in the positions of Ba atoms.

Additional defects can be created under bombardment [22,23]. Depending on the type of particles and their energy there can be obtained both point and linear defects (tracks of high energy heavy particles) [24].

1.1.3. Influence of defects on transport properties of $YBa_2Cu_3O_{7-\delta}$ superconductor in the normal state. Transport properties of HTS materials depend very heavily on the structure imperfection and, specifically, on the oxygen content [25] and impurities [26, 27]. The specific electrical resistivity at room temperature of $YBa_2Cu_3O_{7-\delta}$ single crystals with the oxygen content close to stoichiometric equals to ρ_{ab} = 200 mΩ cm in ab – plane, and ρ_c = 10 mΩ cm along ***c*** axis [2]. In perfect single crystals the electrical conduction is quasi-metal in all crystallographic directions [1-3, 28]. However, even a small stoichiometric deviation $\delta \le 0.1$ leads to quasi-semiconductor dependence $\rho_c(T)$ under preservation of the quasi-metal type of the dependence $\rho_{ab}(T)$. Further reduction of the oxygen content leads to the density reduction of current, heat and conductivity carriers of $YBa_2Cu_3O_{7-\delta}$ superconductor, and under oxygen deficiency $\delta \ge 0.6$ the metal-insulator transition is observed [28]. Doping of $YBa_2Cu_3O_{7-\delta}$ with metal elements, with the exception of cases described above, leads to the replacement of copper atoms in CuO planes. In this case the data regarding the level of influence of such replacement are substantially contradictory. For example, in the work [29] it is reported that according to the data from different authors the growth of ρ_{ab} value in $YBa_2Cu_{3-z}Al_zO_7$ crystals at $z = 0.1$ can be less than 10%, or it will increase twofold at the same Al concentration. The reason for such divergence is likely to be the inhomogeneous Al distribution throughout the volume of crystals because under single-crystal growth in corundum crucibles the Al implantation occurs in an uncontrolled way. In particular, wide transitions in superconductive state $T_c \approx$ 2 K are representative of inhomogeneous Al distribution. There is also a significant spread in superconductive state parameters. Doping of $YBa_2Cu_3O_{7-\delta}$ under replacement of yttrium by rare-earth metal ions practically does not change transport characteristics of the normal and superconductive state [3, 24]. The replacement of yttrium atoms by praseodymium atoms is an exception. In the area of $y \le$ 0.05 concentrations the current carrier concentration and ρ_{ab} in $Y_{1-y}Pr_yBa_2Cu_3O_{7-\delta}$ superconductor weakly depend on Pr concentration [30]. At $y \approx 0.5$ we observe a sharp fall of the current carrier concentration and at $y > 0.5$ we observe $\rho(T)$ dependence typical for superconductors [30,31].

As mentioned above, there are flat defects, twin boundaries, in $YBa_2Cu_3O_{7-\delta}$ single crystals. The work [32] deals with the influence of these defects on transport properties in the normal state. It shows that the twins are effective scattering centres of current carriers. According to [32] the free path of electrons in single crystals is measured equal to 0.1 μm, which is one order less than the intertwine distance. Therefore, the maximum increase of electrical resistance due to scattering can make up 10%. It was observed approximately the same resistance increase under current flow across twins in comparison with the resistance under current flow along twins [33].

1.1.4. Fluctuation conductivity and 2D-3D crossover in HTS. As it is generally known, small coherence length value and quasi-laminated structure of HTS leads to emergence of a wide fluctuation area on temperature dependences of conductivity near the superconducting transition temperature [3, 8, 9, 33, 34, 36-39]. Besides, the change of oxygen content and impurities has a significant impact on the formation processes of fluctuation Cooper pairs and, respectively, on the realization of different modes for existence of fluctuation conductivity (FC) at temperatures higher than the critical temperature (T_c) [3,5,8,9,33,34]. It is widely agreed now that the FC existence domain can be conditionally divided into three characteristic temperature intervals defined by the correlation between the coherence length perpendicularly to ab-plane $\xi_c(T)$ and the interlayer distance *d:*

1) $\xi_c(T) << d$ – 2D-area (the most distant from T_c);

2) $\xi_c(T) \approx$ d – 3D-area (the closest to T_c);

3) narrow section in the immediate vicinity to T_c – so called «beyond - 3D» mode [5,34].

The last mode mechanism emergence is still not clear enough. It is assumed that the mode fits so called "first level pairing" [5, 34]. The 3D-area fits the mode where Josephson interaction between pairs is realized throughout the body of superconductor. It is thought that in this area the capital contribution to FC is due to Cooper pairs emerging spontaneously at $T > T_c$ as a result of the classical mechanism that was first described in the well-known paper of Aslamazov-Larkin [35]. According to [35] this contribution to HTS can be written as:

$$\Delta\sigma_{AL}(T) = [e^2 / 32\hbar\xi_c(0)]\varepsilon^{1/2}, \quad (2)$$

where $\varepsilon = (T-T_c)/T_c$ – reduced temperature (T_c – critical temperature in mean field approximation). Here $\Delta\sigma_{AL}$ practically does not depend on the sample structure imperfection.

In 2D-area the two-particle tunneling between layers is ruled out. As a result superconductive and normal carriers are situated directly in the planes of conductive layers. In this case taking into account the irregularity level of the sample structure is of prime importance. The influence of the structure imperfection on FC mode in film samples of $YBa_2Cu_3O_{7-\delta}$ compound was researched in the works [8, 9]. Here it was shown that for pure samples the dominating contribution in FC in 2D-area is due to the additional contribution substantiated by Maki-Thompson [36] and defined as a result of interaction for fluctuation pairs with normal charge carriers. Such contribution depends on the lifetime of fluctuation pairs and it is defined by unpairing processes in a specific sample. According to [36]:

$$\Delta\sigma_{MT}(T,H) = \frac{e^2}{8\hbar d(1-\alpha/\delta)\varepsilon} \times$$

$$\times \ln\left\{\frac{\delta}{\alpha}\cdot\frac{1+\alpha+\sqrt{1+2\alpha}}{1+\delta+\sqrt{1+2\delta}}\right\} \quad (3)$$

If there are structural irregularities in the sample, $\Delta\sigma(T)$ dependence is defined with Lawrence-Doniah [37]:

$$\Delta\sigma_{LD} = [e^2 / (16\hbar d)](1+2\alpha)^{1/2}\varepsilon^{-1} \quad (4)$$

Here $\alpha = 2\xi_c^2(T)/d^2 = 2[\xi_c(0)/d]^2\varepsilon^{-1}$ – coupling parameter, and $\delta = 1.203(1/\xi_{ab}(0))(16/\pi\hbar)[\xi_c(0)/d^2]k_BT\tau_\phi$ – unpairing parameter. Here l – free path length, ξ_{ab} – coherence length in ab-plane and τ_ϕ – lifetime of fluctuation pairs. It should be noted that we have a crucial issue regarding the temperature range where the $\Delta\sigma(T)$ dependence can be described within the fluctuation theory because, according to current concepts, the excess conductivity at temperatures rather distant from the critical $T >> T_c$ is an effect of the so-called "pseudogap anomaly". It was experimentally discovered earlier [3] that at a rather large temperature increase above T_c the fluctuation conductivity decreases more quickly than the theory predicts. It was supposed that the reason for this process is in underestimation of short-wave order-parameter fluctuations while it increases with the temperature growth. In the works of Varlamov with co-authors [38, 39] the microscopic estimation of $\Delta\sigma(T)$ was made taking into account all order parameter components. The comparison of experimental data with the theory [38, 39] was made, in particular, in [40]. In this case there was an agreement with the theory for the temperatures up to near $T \approx 1.35\ T_c$. Under further temperature increase the $\Delta\sigma(T)$ decreases more quickly than the theory predicts [38, 39]. Apparently, it is this temperature area where the transition to the pseudogap mode occurs [40]. The pseudogap mode will be considered more thoroughly in the next chapter.

1.2. Pseudogap state in HTS- compounds

In high-temperature superconductors, as it follows from the phase diagram (see fig. 2.2), under change of the oxygen index the dielectric antiferromagnetic phase will be replaced by metal one and then by superconducting phase which does not have an ordered magnetic structure [41].]. There was discovered the emergence of the pseudogap phase (considerable density decrease of electronic states) above the superconducting transition point under the oxygen content less than optimal. The pseudogap phase is observed in numerous magnetic [42, 43], neutron diffraction [44], optical [45,46] and nuclear magnetic resonance researches [47], and in experiments of the angle-resolved photoelectron spectroscopy (ARPES) as well. In resistive measurements the pseudogap anomaly is displayed in the departure $\xi_{ab}(T)$ from linearity under the temperature decrease below some representative value T^* [2,8,9,40,50], which is an evidence of the emergence of some excess conductivity. There are two dividing lines: "upper" pseudogap (there begin resistance deviations from the linear law) and "lower" pseudogap (pseudogap proper) in many phase diagrams.

At present the literature intensively discusses two main scenarios of the pseudogap anomaly emergence in HTS-systems. According to the first one the pseudogap emergence is linked to "dielectric" short-range order fluctuations, for example antiferromagnetic fluctuations, spin and charge density waves et cetera (see, for example, review [41]). The second scenario supposes the formation of Cooper pairs even at temperatures considerably higher than the critical $T^* >> T_c$ with the subsequent establishment of their phase coherence at $T < T_c$ [40,51].

In recent years the model of fluctuating antiferromagnetic clusters has been intensively researched in theoretical works of Sadovsky with co-authors [41,

52]. Thus, for example, in [52] the authors generalized dynamic medium field theory by including the terms that depend on the correlation length of pseudogap fluctuations in the corresponding equations. These summands are expressed by means of some additional self-energy which in its turn depends on the impulse and describes nonlocal dynamic correlations induced by short-range collective fluctuations such as antiferromagnetic spin-density or antiferromagnetic charge-density waves. It should be noted that the conclusions of the above-mentioned paper are based on the results of ARPES researches which are often used for explanation of other different pseudogap models as well. [48, 49].

There was applied an approach based on the approximation within the framework of the effective field theory in the recent large theoretical paper [53]. It should be noted that the phase diagram substantiated in the paper [53] does not have a transition curve into the "weak" pseudogap phase. Besides, it is assumed that the spin-spin fluctuations leading to pseudogap effects are formed not in localized moments but in the conduction band.

As mentioned previously, the concept of uncorrelated electron pairs or so called paired clusters [54] in the explanation of the pseudogap anomaly in HTS is also a subject of a rather wide discussion in scientific works. Among the works upholding this point of view the crossover theory from Bardeen–Cooper–Schrieffer mechanism to the mechanism of Bose-Einstein condensation should be noted. Within this crossover theory there were obtained pseudogap temperature dependences for weak and strong pairing cases [55, 56]:

$$\Delta(T) = \Delta(0) - \frac{\Delta(0)}{2} \times \\ \times \frac{T}{\sqrt{\mu^2 + \Delta^2(0)}} \exp\left(- \frac{\sqrt{\mu^2 + \Delta(0)^2}}{T} \right) \quad (5)$$

where Δ – pseudogap value, and μ – chemical potential.

The authors of this work specify their point of view on the nature of the cuprate pseudogap based on the concept of uncorrelated pairs. However, in the article they write that their research does not include the influence of antiferromagnetic spin fluctuations.

The attempt to unite concepts was made in the work [57]. It is the upper border of "weak" pseudogap that was given special attention in this work. The analytical treatment made in [57] is based on the concept of the resonant valence band which was first proposed in the well-known Anderson RVB model [58, 59]. Here, however, the authors suppose that there are areas of both Bose (b-RVB) and Fermi (f-RVB) types. Whereas Bose area is responsible for the "strong" pseudogap, Fermi area - for the "weak" area respectively. According to these

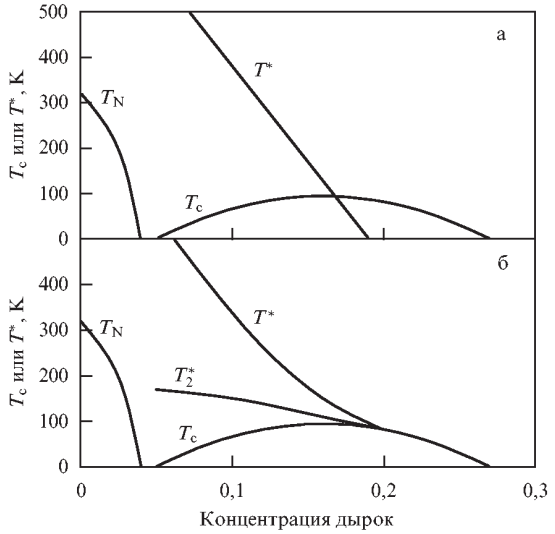

Fig. 2 Phase diagram variants for HTS-cuprates according to [41].

views in the area of the "strong" pseudogap, which is situated just behind the superconducting transition curve, the reduced density of states is caused by the existence of uncorrelated Cooper pairs. But in the "weak" pseudogap area situated above in the phase diagram (fig. 2 (b)), there is an orbital magnetic-ordered state which is destroyed at higher temperatures. However, as it was shown in the works of Boyarsky (see [60] and references to it), the whole set of considerations and facts contains multiple internal contradictions. Besides, up to now there are no substantial experimental proofs of its validity.

In recent years one of dominating concepts for pseudogap anomaly emergence in HTC has been so called cluster model [61-63]. Thus, for example, in the recent theoretical work [61] it was found that the critical temperature T_c and the temperature of pseudogap opening T* in the compound $Y_1Ba_2Cu_3O_{7-\delta}$ are uniquely related to the dimensions of superconducting clusters. The superconducting clusters are generated by oxygen ions forming the negative U centres (NUC) responsible for the carrier generation in the compound. Besides, it is affirmed that the pseudogap observed in different experiments is nothing less than the same superconductive gap but emerging at $T>T_c$ as a result of large fluctuations of the particle number between the NUC pair level and the oxygen area [61]. Here it is supposed that under reduction of the doping level by oxygen the average dimension of clusters decreases, and the relative fluctuations of NUC occupation density increase, which, in its turn, must create rise of T* and drop of T_c [61]. In the work [62] within the framework of the impurity mechanism for the high-temperature superconductivity, on the hypothesis that finite superconducting clusters exist in the area adjoining to the superconductive phase from the doping less than optimal (pseudogap area) and the boundary of the superconductive

phase corresponds to the threshold of existence for an infinite superconductive cluster, there was obtained an upper boundary of the pseudogap state. There was made an attempt to explain the pseudogap state on the basis of the percolation theory on the hypothesis that the coherence length is proportional to $T^* - T$ in the work of Abrikosov [63]. Among experimental works dealing with this matter one should note the experiments where the clusters in HTS were observed by means of the scanning tunnelling spectroscopy [64, 65] and the works [66-69] dealing with the optical studies of oxygen ordering processes as well. However, despite the considerable stored scientific material it is not completely clear both the nature of structural cluster anomalies and the mechanisms of their formation in HTS.

1.3. Redistribution of labile oxygen and evolution of resistive characteristics of $YBa_2Cu_3O_{7-\delta}$ single crystals under heat treatment at low temperatures.

The researches of superconductive [25,61-67] and optical [68, 69] properties of the single crystals $YBa_2Cu_3O_{7-\delta}$ hardened from high temperatures with the oxygen deficiency $\delta \approx 0.5$-0.6 showed that these properties depend not only on the oxygen index value but also on the anneal time at room temperature. Thus, for example, the anneal at room temperature leads to increase of the critical temperature T_c, which can reach $\Delta T_c \approx 15$ K depending on the oxygen index value [25, 66, 67]. The optical researches show [68, 69] that under anneal at room temperature one can observe the increase of the single crystal reflectivity which is explained by the authors as a result of an increase of the current carrier concentration.

Neutron diffraction researches [13] of $YBa_2Cu_3O_{7-\delta}$ ceramic samples hardened from 500°C temperature are evidence of the lattice parameter change under anneal of sample at room temperature: all lattice parameters decrease (Fig. 3), and the degree (a-b) increases (Fig. 4). However, we do not observe a considerable change in the filling factor of oxygen positions in Cu-O plane along a and b axes. The main changes of the critical temperature, (Fig. 4), the lattice parameters (Fig. 3) and the reflectivity under anneal are observed in the early stage of anneal: approximately 85% of general variation value of these characteristics is realized during the first 24 hours.

The influence of anneal at room temperatures on the critical temperature, current carrier concentration and on the lattice parameters change of $YBa_2Cu_3O_{7-\delta}$ oxygen-deficit samples is explained as a result of oxygen atoms ordering in Cu-O plane without change of the oxygen content in the sample. The three issues that arise then are: (1) what is the cause of the critical temperature increase (oxygen ordering or lattice parameters change)?, (2) what range of δ values does the ordering occur in? and (3) What nature and typical scale does this ordering have?

It is known that it is anomalously large increase of the critical temperature of LaBaCuO superconductor under the hydrostatic pressure P, $dT_c/dP=0.64$ K/kbar [70] that stimulated search of new superconductors which have Cu-O layers drawn together due to "internal pressure" caused by the small ionic radius separating these layers. But in $YBa_2Cu_3O_{7-\delta}$ superconductor the baric derivative of the critical temperature is not constant and depends on δ index.

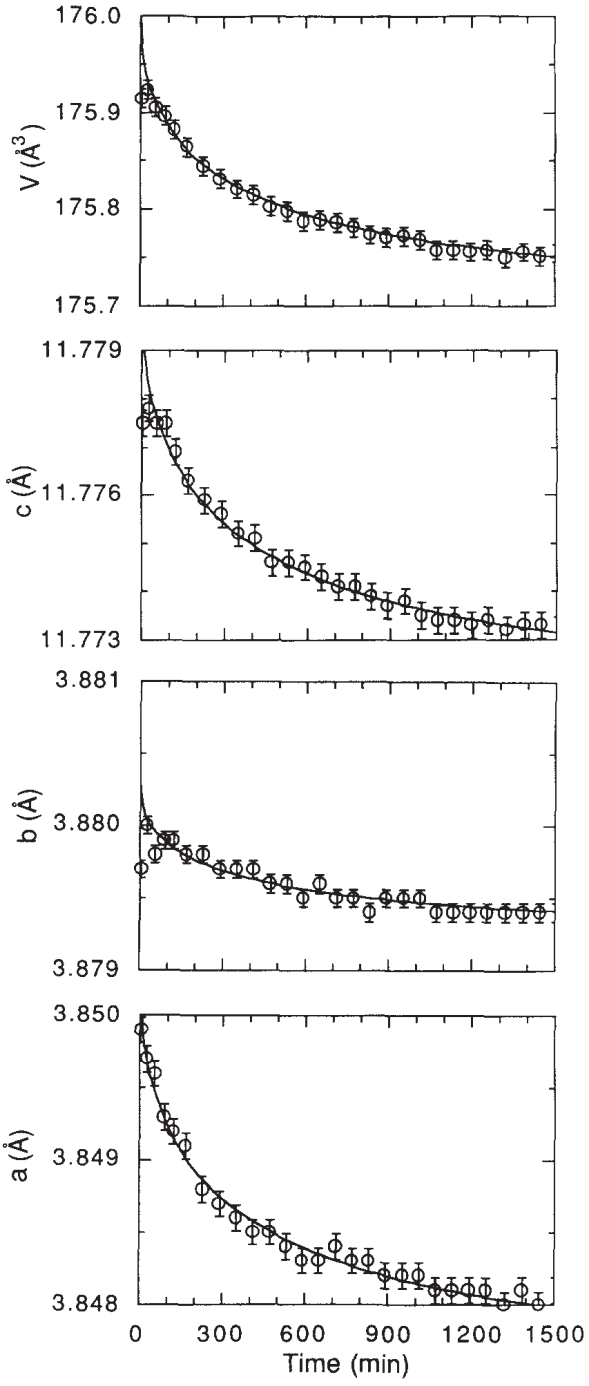

Fig. 3. Dependence of volume and unit cell parameters on anneal time at room temperature for hardened sample $YBa_2Cu_3O_{6.41}$ [13].

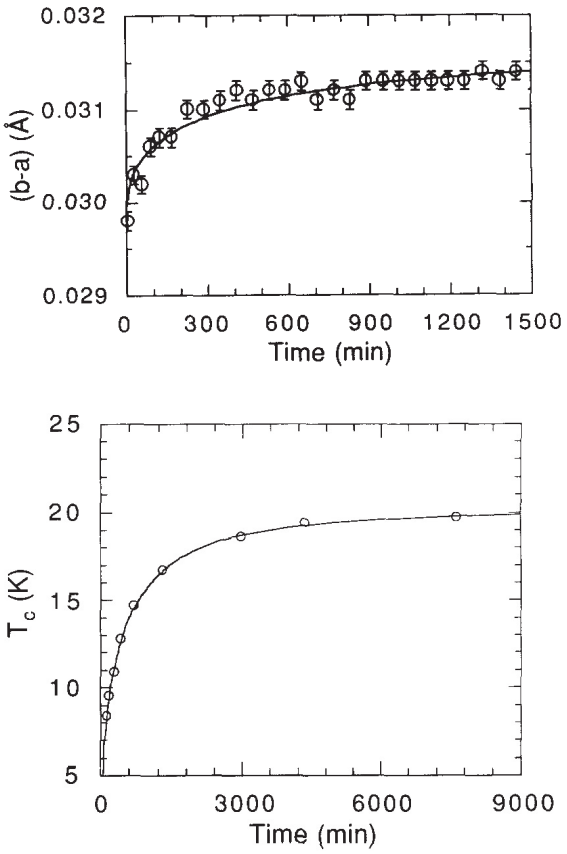

Fig. 4. Dependence of (b-a) difference and critical temperature T_c on anneal time at room temperature for hardened sample $YBa_2Cu_3O_{6.41}$ [13]. Critical temperature was defined from the beginning of diamagnetic response appearance.

Besides, the derivative value has its maximum at $\delta \approx 0.4$-0.5 and equals to (0.1÷1) K/kbar [71-74]. Therefore, the slight decrease of lattice parameters under low-temperature anneal can lead to the considerable critical temperature increase. On the other hand, the authors of the work [66] believe that the T_c increase is due primarily to the change of the local environment of copper atoms in Cu-O planes that leads to the charge distribution in these planes.

The research of oxygen index influence on the critical temperature increase under low-temperature anneal [67] showed that ΔT_c value decreases at δ reduction, an at $\delta \approx 0.2$ there were not observed any changes of T_c value under anneal. However, it should be noted that T_c value is not sensitive to the oxygen index change at $\delta \leq 0.2$ [66], and, therefore, the issue regarding possibilities of the oxygen redistribution in the specified range of δ variation should be investigated further.

The structure of $YBa_2Cu_3O_{7-\delta}$ at $\delta \approx 0$ is defined by Cu-O chains presence, that is, the oxygen positions of O(1) are fully occupied and the positions of O(5) are vacant. Under oxygen deficit $\delta \approx 0.5$ the structure is defined by interchange of chains where the oxygen positions of O(1) are fully occupied, and of chains where the positions of

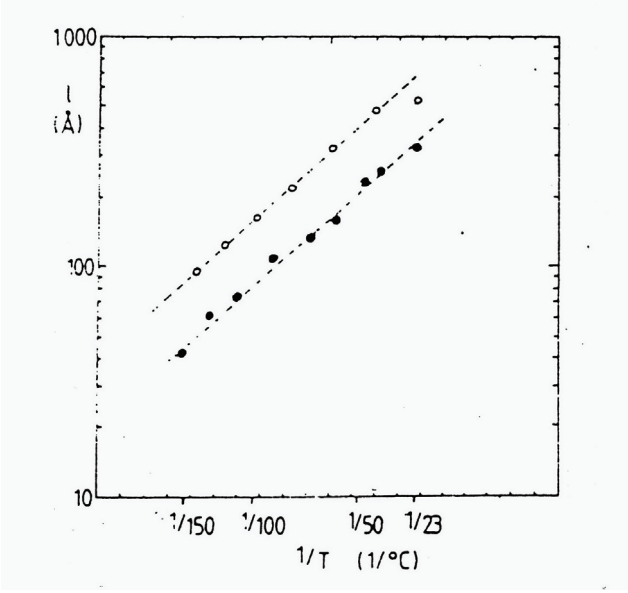

Fig. 5. The average length of chains in $YBa_2Cu_3O_{6.5}$ (shaded circles) and $YBa_2Cu_3O_{6.6}$ (hollow circles) as reciprocal temperature function [69].

O(1) are vacant. The realization of such ordered structures is possible at a stoichiometric ratio between the oxygen concentration and the vacancies, which is equal to 1:0 и 1:1 in these examples. The experimental research of different physical properties of $YBa_2Cu_3O_{7-\delta}$ sample with the oxygen deficit $\delta \approx 0.4$ made it possible for the authors of the work [77] to substantiate the concept of superconductive cluster with the structure close to ordered one under the concentration ratio between oxygen concentrations and vacancies equal to 5:1, 4:1, 3:1 и 2:1. For instance, it is thought that under 5:1 ratio in every sixth chain the oxygen positions of O(1) are vacant and in other chains they are occupied. Under stoichiometric ratio between oxygen concentrations and vacancies it is possible either disordering in the oxygen-vacancies system or the formation of ordered phase-clusters mixture. The issue remains open. The results of the works [13, 68] point to the existence of the ordered state at room temperature. However, the ordering scale obtained from the neutron diffraction [13] researches (≈ 30 Å) is less by an order of magnitude than the value 300 Å obtained from the optical [69] researches (see fig. 5). It should also be noted a possibility of change for the oxygen subsystem state under low-temperature hardening starting from the temperatures T_a = 100÷300 K. The research of hardening influence on the electrical resistance and the critical temperature of the sample from c $T_c \approx 91$ K [78] show that there is increase of T_c and decrease of the specific electrical resistance ρ in the plane (a,b). The variation value of T_c and ρ depended both on the value T_a and on the holding time at T_a. The authors interpreted the obtained results by means of microdiffusion mechanism for the formation of the lattice state with the increased value of T_c. The behaviour of ρ depending on value T_a showed that there was disordering of the initial

state of the oxygen vacancies and their further ordering.

It should also be noted that under resistive measurements the transition to the pseudogap mode is displayed in faster than linear fall of the electrical resistance value in the basis plane $\rho_{ab}(T)$ (emergence of the so called excess conductivity) when the temperature decreases less than some representative value T* which is observed in HTS samples [2, 8, 9, 40]. Since the electrical resistance of such compounds is rather sensitive to the state of the oxygen subsystem, the redistribution of the labile component must have an effect on the temperature dependences $\rho_{ab}(T)$. As far as we know there have not been published any experimental researches regarding the influence of labile oxygen redistribution in the nonequilibrium state (at fixed oxygen concentration in the sample) on the pseudogap anomaly in 1-2-3 system.

Conclusions

In conclusion it should be mentioned that there was considered only a rather small part of scientific publications dealing with different aspects of normal electron transport in HTS in this very brief scientific literature review. The more detailed consideration of the above-mentioned phenomena can be found in the reviews [4, 41]. Nevertheless, following on from the results of the analysis performed we can set up some problems that do no have the ultimate experimental and theoretical solution up to now, such as: (i) what is the nature of the high pressure influence on formation of the pseudogap anomaly in low praseodium-doped $YBa_2Cu_3O_{7-\delta}$ single crystals and what is the role of singularities in the electronic spectrum of these compounds under compressional change of the critical temperature and the lateral coherence length? (ii) What is the role of the structural relaxation induced by the temperature step change in realization of different modes of the longitudinal electron transport? And, in this aspect, what is the influence of isovalent and nonisovalent substitution on the processes of labile component redistribution in the oxygen subsystem? (iii) What is the role of structural defects of different morphology on the realization of specific dynamic transitions in the magnetic subsystem of single-domain single-crystal samples $YBa_2Cu_3O_{7-\delta}$ with a small deviation from the oxygen stoichiometry? What way does the layer structure have an influence on order-disorder transitions?

The performed analysis of the scientific literature dealing with different aspects of unusual properties display of the normal electron transport in HTS in this review made it possible to define some problems that have not been fully-investigated up to now. Despite a considerable body of existing experimental and theoretical works dealing with research of the effects observed in the normal (nonsuperconducting) state we do not have comprehensive understanding of the mechanisms causing these effects. In particular, the examples may include the anomalously wide temperature area of fluctuation paraconductivity phenomenon, so called “pseudogap anomaly”, incoherent electron transport, metal - insulator transitions and a number of other issues.

From this perspective it is very important today to conduct researches concerning determination of the influence level of different morphology defects on single crystal samples with a given defect structure topology. It should also be noted that despite the absence of the microscopic theory there is a special demand for experimental procedures using the extreme exposure of different types (low temperatures, high magnetic fields and high pressures). These procedures makes it possible not only to test the validity of multiple theoretical models but also outline the empiricism for critical parameters increase of HTS compounds.

Consequently, the above-mentioned issues are the base for the solution of the problem involving determination of the influence physics of point and flat defects on magnetoresistive properties of $ReBa_2Cu_3O_{7-\delta}$ compounds (Re = Y and other rare-earth elements), and establishment of laws concerning the conduction state formation such as insulator-metal transition, superconductor - Fermi - liquid metal - nonsuperconductor under carrier concentration variation, under change of the labile component concentration in a wide range and replacement of constituent elements of these compounds as well.

References

1. Bednorz J.G. Possible high T_c superconductivity in the Ba−La−Cu−O system [Text] / J.G Bednorz and K.A. Muller // Zeitschrift für Physik B.-1986. - V.64. - P.189-193.
2. Obolenskii M.A. Localization effects and pseudogap state in $Y_1Ba_2Cu_3O_{7-\delta}$ single crystals with different oxygen content [Text] / M.A. Obolenskii, R.V. Vovk, A.V. Bondarenko, N.N. Chebotaev // Low Temperature Physics. - 2006. - V.32, №6. - P.571-575.
3. 3.Alekseevsky N. E. Fluctuation superconductivity and impurity phases in the perovskitopodobnykh systems and the prospects of increase in the T_c [Text] / N. E. Alekseevsky, A. V. Mitin, V. I. Nizhankovsky, E. P. Hlybov, V. V. Evdokimova, G. M. Kuzmichev // SFHT. - 1989. - V.2, №10. - P.40-55.
4. Luo H.G. Scaling analysis of normal-state properties of high-temperature superconductors [Text] / H.G. Luo, H.P. Su, T. Xiang // Phys. Rev. B. -2008. - V.77. - P.014529 (1-17).
5. Pureur P. Critical and Gaussian conductivity in $Y_1Ba_2Cu_3O_{7-\delta}$ [Text] / P. Pureur, Costa R. Menegotto, R. Rodrigues, J. Schaf Jr., J.V. Kunzler // Phys. Rev. B. - 1993. - V.47. - P.11420-11425.
6. Chryssikos G.D. X-ray diffraction and infrared investigation of $RBa_2Cu_3O_{7-\delta}$ and $R_{0.5}Pr_{0.5}Ba_2Cu_3O_7$ compaunds (R=Y and lanthanides) system [Text] / G.D. Chryssikos, E.I. Kamitsos,

J.A. Kapoutsis, A.P. Patsis, V. Psycharis, A. Kafoudakis, C. Mitros, G. Kallias, E. Gamari-Seale, D. Niarchos // Physica C. - 1995. - V.254 (1-2). - P.44-62.

7. Borges H.A. Pressure study of the paraconductivity of high T_c superconductors system [Text] / H.A. Borges, M.A. Continentino // Solid State Commun. - 1991. - V.80. - P.197-199.
8. Solovyov A. L. Fluctuation conductivity in $YBa_2Cu_3O_{7-\delta}$ films with various content of oxygen. II. Optimum dopirovanny and slabodopirovanny films of YBCO / A.L. Solovyov, H. - U. Habermeier, T. Haage // FNT. - 2002. -V.28, №1. - P.24-35.
9. Solovyov A. L. Fluctuation conductivity in $YBa_2Cu_3O_{7-\delta}$ films with various content of oxygen. II. Optimum dopirovanny and slabodopirovanny films of YBCO [Text] / A.L. Solovyov, H. - U. Habermeier, T. Haage // FNT. - 2002. - V.28, №2. - P.144-156.
10. Kanoda K. Dimensionality and Superconductivity in $Y_1Ba_2Cu_3O_{7-\delta}$ / K. Kanoda, T. Kawagoe, M. Hasumi, T. Takahashi, S. Kagoshima, T. Mizoguchi system [Text] // Journal of the Physical Society of Japan. - 1988. -V.57, №5. - P.1554-1557.
11. Belyaeva A.I. Twin boundaries role in superconducting properties formation of single crystals $Y_1Ba_2Cu_3O_{7-\delta}$ system [Text] / A.I. Belyaeva, S.V. Vojtsenya, V.P. Yuriyev, M.A. Obolenskii, A.V. Bondarenko // Solid State Commun. - 1993. - V.85, № 5. - P.427-430.
12. Eturno Zh. Structure of high-temperature superconducting oxides [Text] / Zh. Eturno // Moscow "World": Physics abroad. - 1989. - P.25-27.
13. Giapintzakis J. Han A method for obtaining single domain superconducting YBa2Cu3O7-x single crystals [Text] / J Giapintzakis, D.M. Ginzberg, P.D // J. Low Temp. Phys. -1989. - V.77, №1/2. - P.155-161.
14. Kemin T. A superstructure in single crystals $Y_1Ba_2Cu_3O_{7-x}$ [Text] / T. Kemin, H. Meisheng, W. Yening // J. Phys. Condens. Matter. -1989. -V.1, №6. - P.1049-1054.
15. Lacayc G. Twin to tweed transition in YBaCuO by substitution of Cu [Text] / G. Lacayc, R. Hermann, G. Kaestener // Physica C. - 1992. - V.192. - P.207-214.
16. Pan V.M. YBaCuO single crystals microstructure related to critical current density [Text] / V.M. Pan, V.L. Svechnikov, V.F. Solovjov, V.F. Taborov, H.W. Zandbergen // Supercond. Sci. Technol. - 1992. - V.5, № 12. - P.707-711.
17. Kes P.H. Vortex pinning and creep experiments [Text] / P.H. Kes // Proceedings of the Los Alamos Symposium "Phenomenology and Application of HTSC". - Los Alamos, NM. - 1991. - P.390-434.
18. Gawalek W. High critical currents in peritectically grown $YBa_2Cu_3O_{7-\delta}$ single crystals [Text] / W. Gawalek, W. Schueppel, R. Hergt // Supercond. Sci. Technol. -1992. -V.5. - P.407-410.
19. Kvardakov V. V. Research of defects of monocrystals of kuprat by methods of neutron topography and selective etching [Text] / V.V. Kvardakov, V. A. Somenkov, S. Sh. Shilstein // SFHT.-1992. - V.5, № 4. - P. 624-630.
20. Selvamanickam V. Flux pinning by dislocation in deformed melt-textured $YBa_2Cu_3O_x$ superconductors [Text] / V. Selvamanickam, M. Mironova, S. Son, K.Salama // Physica C: Superconductivity and its applications. -1993. -V.208, №3, - P.238-244.
21. Roth G. Copper deficiency in $Y_1Ba_2Cu_3O_{7-x}$ [Text] / G. Roth, G. Heger, P. Schweiss et al. // Physica C. - 1988. - V.152, №4. - P.329-334.
22. Bondarenko A.V. Effect of electron irradiation on anisotropy of vortex creep in YBCO single crystal [Text] / A.V. Bondarenko, A.A. Prodan, Yu.T. Petrusenko, V.N. Borisenko, F. Dworschak, U. Dedek // Magnetic and superconducting materials.-1999. - P.499-506.
23. Bondarenko A.V. Effect of electron irradiation on vortex dynamics in $YBa_2Cu_3O_{7-\delta}$ single crystals [Text] / A.V. Bondarenko, A.A. Prodan, Yu.T. Petrusenko, V.N. Borisenko, F. Dworschak, U. Dedek // Phys. Rev. B.-2001. - V.64, №9. - P.2513(4).
24. Ginzberg D. M. Physical properties of high-temperature superconductors. [Text] / D. M. Ginzberg. // M.: World. - 1991. - P.543.
25. Obolensky M. A. Processes of a relaxation of resistance in the kisloroddefitsitnykh monocrystals of $Y_1Ba_2Cu_3O_{7-\delta}$ [Text] / M. A. Obolensky, A. V. Bondarenko, R. V. Vovk, A. A. Prodan // FNT. - 1997. - V.23, №11. - P.1178-1183.
26. Obolensky M. A. Magnetic measurements of critical current and potential of a pinning in monocrystals of $Y_{1-x}Pr_xBa_2Cu_3O_7$ [Text] / M. A. Obolensky, A. V. Bondarenko, V. I. Beletsky, A. V. Samoylov, D. Niarkhos, M. Pissas, G. Kallias, A. G. Sivakov // Functional Materials. - 1995. - V.2, №4. - P. 409-414.
27. Vovk R.V. Excess conductivity and pseudo-gap state in YBCO single crystals slightly doped with Al and Pr [Text] / R.V. Vovk, M.A. Obolenskii, A.A. Zavgorodniy, A.V. Bondarenko, I.L. Goulatis, A.I. Chroneos // J Mater Sci: Mater Electron.-2007. - V.18. - P.811-815.
28. Alexandrov I. V. New data on dependence of critical temperature on the content of oxygen in the superconducting $YBa_2Cu_3O_x$ [Text] / I.V connection. Alexandrov, etc. (12 coauthors) // Letters in JETP.-1988. - V.48, №8. - P.449-452.
29. Van Dover R.B. Extraordinary effect of aluminum substitution on the upper critical field of $YBa_2Cu_3O_7$ [Text] / R.B. Van Dover, L.F. Schneemeyer, J.V. Waszczak et al. // Phys. Rev. B. - 1989. - V.39, №4.-P.2932-2935.
30. Kebede A. Magnetic ordering and superconductivity in $Y_{1-y}Pr_yBa_2Cu_3O_7$ [Text] / A. Kebede // Phys. Rev. B. - 1989. - V.40, №7. - P. 4453-4462.
31. Radousky H.B. A review of the superconducting and normal state properties of $Y_{1-x}Pr_xBa_2Cu_3O_{7-\delta}$ [Text] / H.B. Radousky // J.Mater. Res. -1992. -V.7, №7. - P.1917-1955.
32. Moshchalkov V. V. Superconductivity and localization in the $YBa_2Cu_3O_{7-\delta}$ system [Text] / V. V. Moshchalkov, etc. (6

coauthors) // FNT. - 1988. - V.14, №9. - P.988-992.
33. Obolenskii M.A. Effect of twin boundaries on scattering processes of normal and fluctuating carriers in $Y_1Ba_2Cu_3O_{7-\delta}$ single crystals [Text] / M.A. Obolenskii, R.V. Vovk, A.V. Bondarenko // Functional Materials.-2006. - V.13, №1. - P.35-38.
34. Mendonca Ferreira L. Pressure effect of pressure on the fluctuation conductivity of $YBa_2Cu_3O_7$ [Text] / L. Mendonca Ferreira, P. Pureur, H.A. Borges, P. Lejay // Physica B. - 2004. - V.69. - P.212505.
35. Aslamazov L. G. Influence of fluctuations on properties of superconductors at temperatures is higher than critical [Text] / L.G. Aslamazov, A. I. Larkin // FNT. - 1968. - V.10, №4. - P.1104-1111.
36. Bieri J.B. Nonlocal effect in magnetoconductivity of high-Tc superconductors [Text] / J.B. Bieri, K. Maki, R.S. Thompson // Phys. Rev. B. - 1991. - V.44, №9. - P.4709-4711.
37. Lawrence W.E. Theory of layer structure superconductors [Text] / W.E. Lawrence, S. Doniach // Proc. 12th Inter. Conf. on Low Temperature Physics, Akademic Press of Japan, Kyoto. -1971. - P.361-362.
38. Varlamov A. A. To a question of influence of superconducting fluctuations on thermo - the EMF and heat conductivity of a superconductor near the critical temperature of [Text] / A.A. Varlamov, D. V. Livanov // JETP.-1990. - V.98, №2 (8). - P.584-592.
39. Reggani L. Fluctuation conductivity of layered high-Tc superconductors: A theoretical analysis of recent experiments [Text] / L. Reggani, R. Vaglio, A.A. Varlamov // Phys. Rev. B. -1991. - V.44. - P.9541-9546.
40. Prokofiev D. D. The size and temperature dependence of a pseudo-crack in YBaCuO received from resistive measurements [Text] / D. D. Prokofiev, M. P. Volkov, Yu. A. Boykov // FNT.-2003. - V.45, №7. - P.1168-1176.
41. Sadovsky M. V. Psevdoshchel in high-temperature superconductors [Text] / M. V. Sadovsky // UFN. - 2001. - V.171, №5. - P.539-564.
42. Krasnov V.M. Evidence for Coexistence of the Superconducting Gap and the Pseudogap in Bi-2212 from Intrinsic Tunneling Spectroscopy [Text] / V.M. Krasnov, A. Yurgens, D. Winkler, P. Delsing, T. Claeson // Phys. Rev. Lett. - 2000. - V.84, №25. - P.5860-5863.
43. Krasnov V.M. Magnetic Field Dependence of the Superconducting Gap and the Pseudogap in Bi2212 and $HgBr_2$-Bi2212, Studied by Intrinsic Tunneling Spectroscopy [Text] / V.M. Krasnov, A.E. Kovalev, A. Yurgens, D. Winkler // Phys. Rev. Lett. -2001. -V.86, №12. - P.2657-2660.
44. Fauqué B. Magnetic order in the pseudogap phase of high - T_c superconductors [Text] / B. Fauqué, Y. Sidis, V. Hinkov, S. Pailhès, C.T. Lin, X. Chaud, P. Bourges // Phys. Rev. Lett. -2006. - V.96, №19. -P.197001.
45. Puchkov A.V. Evolution of the Pseudogap State of High - T_c Superconductors with Doping [Text] / A.V. Puchkov, P.Fournier, D.N.Basov, T.Timusk, A.Kapitulnik, N.N. Kolesnikov // Phys. Rev. Lett. -1996. - V.77, №15. - P.3212-3215.
46. Startseva T. Temperature evolution of the pseudogap state in the infrared response of underdoped $La_{2-x}Sr_xCuO_4$ [Text] / T. Startseva , T.Timusk, A.V. Puchkov, D.N. Basov, H.A. Mook, M. Okuya, T. Kimura, K. Kishio // Phys. Rev. B. - 1999. - V.59, №10. - P.7184-7190.
47. Gorny K. Magnetic Field Independence of the Spin Gap in $YBa_2Cu_3O_{7-\delta}$ / K. Gorny, O.M. Vyaselev, J.A. Martindale et al. (11 auth.) [Text] // Phys. Rev. Lett. -1999. - V.82, №1, - P.177-180.
48. Tohyama T. Role of next-nearest-neighbor hopping in the t-t'-J model / T. Tohyama, S. Maekawa [Text] // Phys. Rev. B. - 1994. - V.49, №5. - P.3596-3599.
49. Dessau D.S. Key features in the measured band structure of $Bi_2Sr_2CaCu_2O_{8+\delta}$: Flat bands at EF and Fermi surface nesting [Text] / D.S. Dessau, Z.-X. Shen, D.M. King et al. (11 auth.) // Phys. Rev. -1993. - V.71, №17. - P.2781-2784.
50. Vovk R. V. Influence of redistribution of labile oxygen on a pseudo-slot-hole state in the bezdvoynikovykh monocrystals of the $YBa_2Cu_3O_{7-x}$ [Text] / R. V. Vovk, M. A. Obolensky, A. A. Zavgorodny, A. V. Bondarenko, I. L. Gulatis, N. N. Chebotayev // FNT. - 2007. - V.33, №8. - P.931-934.
51. Pieri P. Magnetic Field Effect on the Pseudogap Temperature within Precursor Superconductivity [Text] / P. Pieri, G.C. Strinati, D. Moroni // Phys. Rev. Lett. -2002. - V.89, №12. - P.127003(1-4).
52. Kuchinskii E.Z. Destruction of the Fermi surface due to pseudogap fluctuation in strongly correlated systems [Text] / E.Z. Kuchinskii, I.A. Nekrasov, M.V. Sadovskii // ZhETF Letters. - 2005. - V.82, №4. - P.198-203.
53. Varma C.M. A theory of the pseudogap state of the cuprates [Text] / C.M. Varma // Cond. mat. - 2005. - P.0507214.
54. Srivastava J.K. Paired Cluster Model of High-Tc Superconductivity: Explanation for Pseudogap Critical Concentration, Vortex Core Pseudogap and Possible Stripe Phase in High-Tc Superconductors [Text] / J.K. Srivastava // Cond. mat. - 2005. - P.0504245.
55. Babaev E. Crossover from Weak- to Strong-Coupling Superconductivity and to Normal State with Pseudogap [Text] / E. Babaev, H. Kleinert // Cond. mat. - 1998. - P.9804206.
56. Babaev E. Nonperturbative XY-model approach to strong coupling superconductivity in two and three dimensions [Text] / E. Babaev, H. Kleinert // Phys. Rev. B. -1999. - V.59, №18. - P.12083-12089.
57. Zheng-Cheng Gu. Magnetic characterization of the upper pseudogap phase in cuprates [Text] / Cheng Gu Zheng, Yu Weng Zheng // Phys. Rev. B.-2005. - V.72. - P.104520 (10 pages).
58. Anderson P.W. The Theory of Superconductivity in the High Cuprates [Text] / P.W. Anderson // Princeton Univ. Press, Princeton NJ. -1997.

59. Anderson P.W. "Normal" Tunneling and "Normal" Transport: Diagnostics for the Resonating-Valence-Bond State [Text] / P.W. Anderson, Z. Zou // Phys. Rev. Lett. -1988. -V.60, №2. - P.132-135.
60. Boyarsky L. A. Fluctuation and heterogeneity in strongly correlated electronic systems [Text] / L.A. Boyarsky, S. P. Gabuda, S. G. Kozlova // FNT. - 2005. - V.31, №3-4. - P.405-411.
61. Stojkovic B.P. Theory of the longitudinal and Hall conductivities of the cuprate superconductors [Text] / B.P. Stojkovic, D. Pines // Phys. Rev. B. - 1997. - V.55, №13. - P.8567-8595.
62. Zverev V. N. Anisotropy of normal resistance of monocrystals of the $YBa_2Cu_3O_{7-x}$ with deficiency of oxygen [Text] / V. N. Zverev, D. V. Shovkun // Letters in JETP. - 2000. - V.72, №2. - P.103-108.
63. Zverev V.N. Pseudogap behavior of the normal state out-of-plane resistance in underdoped single crystals [Text] / V.N. Zverev, D.V. Shovkun // Physica C: Superconductivity and its applications.-2003. -V.391, №4. - P.315-318.
64. Alexandrov A.S. Coherent ab and c Transport Theory of High-Tc Cuprates [Text] / A.S. Alexandrov, V.V. Kabanov, N.F. Mott // Phys. Rev. Lett. -1996. - V.77, №23. - P.4796-4799.
65. Abrikosov A.A. Resonant tunneling in high-temperature superconductors of [Text] / A.A. Abrikosov // UFN. - 1998. - V.168, №6. - P.683-695.
66. Claus H. Atomic short-range order in oxygen-deficient $YBa_2Cu_3O_{7-\delta}$ [Text] / H. Claus, S. Yang, A.P. Paulicas et al. (5 auth.) // Physica C. - 1990. -V.171, №3,4. - P.205-210.
67. Veal B.W. Time-dependent superconducting behavior of oxygen-deficient $YBa_2Cu_3O_x$: Possible annealing of oxygen vacancies at 300 K [Text] / B.W. Veal, H. You, A.P. Paulicas et al. (6 auth.) // Phys. Rev. B. - 1990. -V.42, №7. - P.4770-4773.
68. Jorgencen D., Shiyou P., Lightfoot P., Shi H., Paulikas A.P., Veal B.M.W. Time-dependent structural phenomena at room temperature in quenched $YBa_2Cu_3O_{6.41}$ [Text] / D. Jorgencen, P. Shiyou, P. Lightfoot, H. Shi, A.P. Paulikas, B.M. Veal. // Physica C. -1990. - V.167, №3. - P.571-578.
69. Kircher J. Optical investigations of room-temperature chain ordering in $YBa_2Cu_3O_{7-\delta}$ [Text] / J. Kircher, M. Cardona, A. Zibold et al. (5 auth.) // Phys. Rev. B. - 1993. -V.48, №13. - P.9684-9688.
70. Chu C.W. Evidence for Superconductivity above 40 K in the La-Ba-Cu-O Compound [Text] / C.W. Chu, P.H. Hor, R.L. Meng, et al. (6 auth.) // Phys. Rev. Lett. - 1987. - V.58, №4. - P.405-407.
71. Svistunov V. M. Influence of pressure upon fluctuation effects in ceramic-metal superconductors [Text] / V. M. Svistunov, V. Yu. Tarenkov, A. I. Dyachenko, etc. (6 coauthors) // FNT. - 1988. - V.30, №11. - P.3498-3501.
72. Metzler J. Separation of the intrinsic pressure effect on T_c of $Y_1Ba_2Cu_3O_{6.7}$ from a T_c enhancement by pressure-induced oxygen ordering [Text] / J. Metzler, T. Weber, W.H. Fietz et al. (7 auth.) // Physica C. - 1993. - V.214, №3-4. - P.371-376.
73. Fietz W.H. Oxygen ordering effect and the superconducting transition temperature T_c of $Y_1Ba_2Cu_3O_x$ under pressure [Text] / W.H. Fietz, R. Quenzel, K. Grube et al. (6 auth.) // Physica C. - 1994. - V.235-240. -P.1785-1786.
74. Sadewasser S. Pressure dependence of T_c to 17 GPa with and without relaxation effects in superconducting $Y_1Ba_2Cu_3O_x$ [Text] / S. Sadewasser, J.S. Schilling, A.P. Paulicas, B.M. Veal // Phys. Rev. B. - 2000. - V.61, №1. - P.741-749.
75. Molchanov V. M. An atomic structure of monocrystals of Y1Ba2Cu3Ox with the intermediate content of oxygen [Text] / V. M. Molchanov, L. A. Muradyan, V. I. Simonov // Letters in JETP. - 1989. - V.49. - P.222-226.
76. Beyers R. Oxygen ordering, phase separation and the 60 K and 90 K plateaus in $Y_1Ba_2Cu_3O_x$ [Text] / R. Beyers, B.T. Ahn, G. Gorman, et al. (10 auth.) // Nature Publishing Group. -1989. - V.340. - P.619-621.
77. Sukharevsky V. Ya. Manifestation of atomic streamlining in characteristics of a normal and superconducting state of VTSP-oxides $Y_1Ba_2Cu_3O_x$ [Text] / Sukharevsky V. Ya., Zhikharev I. V., Khokhlova S. I., etc. // FNT. - 1990. - V.7, №8. - P.971-986.
78. Mamalui A. A. Low-temperature training of monocrystals of $Y_1Ba_2Cu_3O_{7-\delta}$ [Text] / A.A. Mamalui, L. S. Palatnik, K. V. Bednov, M. A. Obolensky, A. V. Bondarenko // FNT. - 1993. - V.19, №11. - P.1180-1186.

Вісник ХНУ, серія «Фізика», вип. 24, 2016. с. 17-19

PACS: 75.30.–m (Intrinsic properties of magnetically ordered materials);
75.47.Gk (Colossal magnetoresistance);
75.47.–m (Magnetotransport phenomena; materials for magnetotransport)
72.15.Eb.Electrical and thermal conduction in crystalline metals and alloys
UDC: 538.93

Comparison between magnetoresistivity and magnetothermopower in $Bi_{93.99}Mn_6Fe_{0.01}$

V.N. Svetlov[1], V.B. Stepanov [1,2], A.V. Terekhov[1,2] , E.V. Khristenko[1], A.D. Shevchenko[3], O.M. Ivasishin [3], Z.D. Kovalyuk[4], and A.L. Solovjov[1].

[1]B. I.Verkin Institute for Low Temperature Physics and Engineering of National Academy of Science of Ukraine, 47 Lenin ave., 61103 Kharkov, Ukraine
[2]International Laboratory of High Magnetic Fields and Low Temperatures, 95 Gajowicka Str., 53-421, Wroclaw, Poland
[3]G.V. Kurdumov Institute of the Metallophisics of National Academy of Science of Ukraine, 36 Nernadskogo ave., ,03142Kiev,Ukraine
[4]I. M. Frantsevich Institute for Problems of Materials of Science. Chernovtsy Department of National Academy of Science of Ukraine, Str. J. Wilde, 5, Chernivtsi, 58001, Ukraine
E-mail: svetlov@ilt.kharkov.ua.
Submitted 15 December 2015

For the first time magnetoresistivity $\Delta\rho/\rho$ and magnetothermopower $\Delta S/S$ in textured polycrystalline samples of $Bi_{93.99}Mn_6Fe_{0.01}$ were studied in a wide temperature range (300 ÷ 4.2) K and in magnetic field B=3 T. The peculiarities on the temperature dependencies of resistivity ρ, magnetoresistivity $\Delta\rho/\rho$, thermopower S and magnetothermopower $\Delta S/S$ were found. These peculiarities are likely due to modification of the band structure of the charge carrier energy spectrum and/or spin-dependent scattering of charge carriers under magnetic field. It is shown that the peculiarities on the temperature dependence of $\Delta\rho/\rho$ and $\Delta S/S$ correlate each other very well.
Keywords: magnetic field, resistivity, magnetoresistivity, thermopower, magnetothermopower

Впервые исследованы магнетосопротивление и магнетотермоЭДС в поликристаллическом образце $Bi_{93,99}Mn_6Fe_{0,01}$ в интервале температур 4,2-300К без магнитного поля и в поле 3Т. Обнаружены особенности на температурных зависимостях электросопротивления, магнетосопротивления, термоЭДС и магнетотермоЭДС при измерениях в магнитном поле 3Т, предположительно обусловленные изменением зонной структуры энергетического спектра носителей заряда и/или спин-зависимого рассеяния носителей заряда, происходящими под действием магнитного поля. Показано, что особенности на температурных зависимостях магнетосопротивления и магнетотермоЭДС хорошо коррелируют друг с другом.
Ключевые слова: магнитное поле, удельное электросопротивление, магнетосопротивление, термоЭДС, магнетотермоЭДС

Вперше досліджено магнетоопір і магнетотермоЕРС в полікристалічному зразку $Bi_{93,99}Mn_6Fe_{0,01}$ в інтервалі температур 4,2÷300К без магнітного поля і в полі 3Т. Виявлені особливості на температурних залежностях електроопору, магнетоопору, термоЕРС і магнетотермоЕРС при вимірах в магнітному полі 3Т, імовірно обумовлені зміною зонної структури енергетичного спектру носіїв заряду та / або спін-залежного розсіювання носіїв заряду, що відбуваються під дією магнітного поля. Показано, що особливості на температурних залежностях магнетоопору і магнетотермоЕРС добре корелюють один з одним.
Ключові слова:.магнітне поле, питомий електроопір, магнетоопір, термоЕРС, магнетотермоЕРС.

Introduction

Magnetic properties study of the materials based on Bi and Mn has shown that at room temperature some of such compounds possess the rather high value of the coercive force which increases with temperature. The fact makes these materials to hold much promise for creating of the permanent magnets for high-temperature applications [1,2]. However, there is a lack of the electrical transport study of these materials in magnetic fields. In our recent paper [3] we have partially filled up the gap and studied the temperature dependence of resistivity $\rho(T)$ of the textured polycrystalline $Bi_{93.99}Mn_6Fe_{0.01}$ in the temperature

range (300 ÷ 4.2) K in magnetic field B=6T. However, no experiments as for thermopower in such compounds have been performed so far. In the paper we report on results of the simultaneous measurements of the temperature dependencies of the resistivity ρ(T) and thermopower S(T) from room temperature down to 4.2 K in magnetic field B=3 T. The measurement results were used to calculate for the first time the temperature dependencies of magnetoresistivity Δρ/ρ and magnetothermopower ΔS/S.

Matherials and methods

The polycrystalline samples, whose properties have been measured, were prepared using analytical purity grade reagents of Bi, Mn and Fe. The quartz tubes of 16-18 mm long evacuated to the pressure P ~ 10^{-2} Pa were used as containers for the synthesis and growth of the $Bi_{93,99}Mn_6Fe_{0,01}$ polycrystals. The synthesis has been performed in a horizontal tube furnace of the SUOL type. The crystals were grown using Bridgeman's method at temperature 630ºC with the sinking velocity of about 1.5 mm/h.

The process has resulted in textured polycrystalline $Bi_{93,99}Mn_6Fe_{0,01}$ of the cylindrical shape. Rectangular samples of about 7x2x2 mm were cut out along of the element of cylinder. A fully computerized setup on the bases of a Physical Properties Measurement System (Quantum Design PPMS-9T) utilizing the four-point probe technique was used to measure the longitudinal resistivity ρ(T) and magnetoresistivity Δρ/ρ. Silver epoxy contacts were glued to the extremities of the sample in order to produce a uniform current distribution in the central region where voltage probes in the form of parallel stripes were placed. Contact resistances below 1Ω were obtained. Resistivity was measured using alternative current (I = 30 mA, f =17 Hz) running along the largest sample dimension. The thermopower S was measured using the standard approach as described elsewhere [4]. Measurements were performed in a wide temperature range (300 ÷ 4.2) K both without magnetic field and in magnetic field applied perpendicularly to the measuring current. Magnetic field was produced by the superconducting solenoid.

Results and discussion

Figure 1 shows temperature dependences of resistivity ρ (curves 1,4) and thermopower S (curves 2,3) measured both without field (curves 1,2) and in magnetic field B=3 T (curves 3,4). It should be noted, that ρ(T) measured at B=0 demonstrates linear dependence in the whole temperature range from room temperature down to 4.2 K (curve 1). In magnetic field B=3T the positive magnetoresistive effect followed by appearance of noticeable maximum on the ρ(T) curve was observed. The magnitude and location of this maximum increases quickly with increase of the magnetic field.

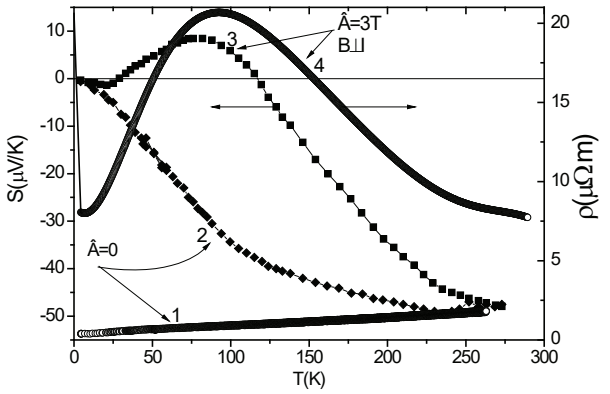

Fig.1. Temperature dependences of resistivity ρ(T) (curves 1,4) and absolute thermopower S(T) (curves 2,3) at B=0 (curves 1,2) and at B = 3 T (curves 3,4).

The specific behavior of ρ(T) in magnetic field, can be caused by different reasons. One of them is the possibility of the transformation of the Mn magnetic subsystem. It is well known that the transition from antiferro- or paramagnetic ordering to ferromagnetic one may be attended by strong changes in conductivity. Most likely it is due to the so-called spin-dependent scattering of the conduction electrons [5,6]. The spin-dependent scattering depends on the direction in which magnetic field is applied to the sample. There are preferred magnetic field directions along which the changes in magnetic subsystem occur more quickly and in more weak fields than it occurs in other directions. Evidently, particularities observed in magnetic field on the ρ(T) are also expected to appear on the temperature dependences of magnetization, thermopower and some other physical characteristics.

Figure 1 shows temperature dependences of the absolute thermopower S (curves 2) measured both without field (curves 2) and in magnetic field B=3 T (curves 3). It is seen that at B=0 measured thermopower has negative sign in the whole temperature range from room temperature down to 4,2 K. Accordingly, under applied field the thermopower S(T) increases much faster with decrease of temperature demonstrating transition from negative values of S to the positive ones at $T_1 \approx 117$ K followed by a distinct maximum at $T_{mS} \approx 80$ K. Below T_{mS} S(T) starts to decrease smoothly along with ρ(T) demonstrating transition from positive values to the negative ones at $T_2 \approx 30$ K. At $T_2 \approx 30$ K weak minimum is observed below which S(T) draws to zero. On the whole, the S(T) curve reminds the ρ(T) dependence in magnetic field (curve 4).

Observed change of the thermopower sign in studied $Bi_{93.99}Mn_6Fe_{0.01}$ can be caused by different reasons. First of all the change of the sign of the charge carriers is possible. This effect is often observed in semimetals which include Bi too. The next reason is the likely change of the charge

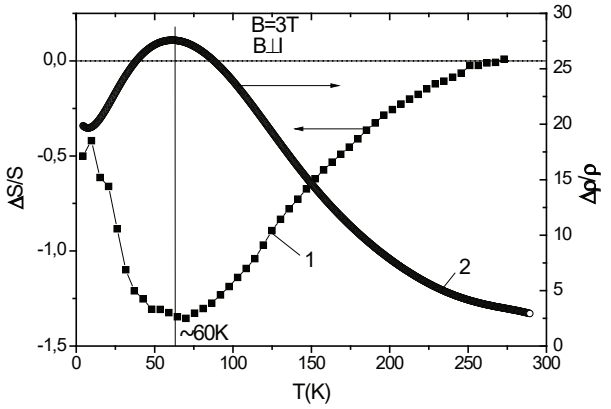

Fig. 2. Magnetoresistivity Δρ/ρ (curve 2) and magnetothermopower ΔS/S (curve 2) as a function of temperature in magnetic field B=3 T.

carrier concentration and their distribution between different isoenergetic surfaces under applied magnetic field [7]. The same physical mechanism can also account for the peculiarities of the ρ(T) behavior observed in magnetic field.

Very interesting result comes from the comparison between temperature dependences of magnetoresistivity Δρ/ρ = [ρ(B, T)-ρ(0, T)]/ρ(0, T) (Fig. 2, curve 2) and magnetothermopower ΔS/S = [S(B, T)-S(0, T)]/S(0, T) (Fig. 2, curve 1). The distinct correlation between both temperature dependences is observed. However, Δρ/ρ increases with temperature demonstrating maximum at $T_{max} \approx 60$ K, whereas ΔS/S noticeably decreases with T demonstrating minimum but again at the same temperature $T_{min} \approx 60$ K. Thus, both maxima observed in Fig. 1 shift towards the lower temperatures. However, if the shape of the Δρ/ρ (T) curve is in keeping with the curve of ρ(T) (Fig. 1), the temperature dependence of the ΔS/S (Fig. 2, curve 1) is completely different. Nevertheless, the minimum of the thermopower is in precise correspondence with the maximum of the thermoresistivity (Fig. 2). The result allows us to conclude that such unusual shape of the ΔS/S (T) dependence is most likely specified by the same physical mechanism (by the rearrangement of the magnetic structure and/or by the modification of the energy band structure). It should be emphasized that such temperature dependence of ΔS/S is observed for the first time. Evidently, the physical processes in $Bi_{93.99}Mn_6Fe_{0.01}$ which result in revealed correlation between the temperature dependencies of magnetoresistivity Δρ/ρ and magnetothermopower ΔS/S require further investigation.

Conclusion

1. It is shown, that textured polycrystalline $Bi_{93,99}Mn_6Fe_{0,01}$ demonstrates noticeable maximum on ρ(T) when magnetic field is applied in B⊥I configuration. The maximum can be connected with the change of the spin-dependent scattering and/or with modification of the changes of the band structure of the energy spectrum of the charge carriers in magnetic field.

2. For the first time maximum on the temperature dependence of the thermopower S(T) is revealed. In addition, below $T_1 \approx 117$ K S(T) demonstrates transition from negative values of S to the positive ones which can be attributed to the transformation of the energy bands structure under magnetic field.

3. For the first time temperature dependence of the magnetothermopower ΔS/S was studied. It is found, that ΔS/S demonstrates minimum at $T_{min} \approx 60$ K. Moreover, the minimum on ΔS/S exactly coincides with the maximum of the magnetoresistivity Δρ/ρ. The finding allows us to conclude that the reasons which result in appearance of peculiarities on both magnetothermopower and magnetoresistivity are caused by the similar physical mechanisms.

References

1. Liu Yong-Sheng, Zhang Jin-Cang, Ren Zhong-Ming, Gu Min-An, Yang Jing-Jing, Cao Shi-Xum and Yang Zheng-Long, Chin. Phys. Lett., 27 (2010) 097502-1-097502-4.
2. N.V. Rama Rao, A.M. Gabay and G.C. Hadjipanayis, J. Phys. D: Appl. Phys, 46 (2013) 062001-062004.
3. V.N. Svetlov, A.V. Terekhov, V.B. Stepanov, A.L. Solovjov, E.V. Khristenko, O.M. Ivasishin, A.D. Shevchenko and Z.D. Kovalyuk, Low Temp. Phys. 41, 314 (2015).
4. V.N. Svetlov, Low Temp. Phys. 38, 181 (2012).
5. E.L. Nagaev, Soviet Physics Uspekhi 39, 781 (1996).
6. M.N. Baibich, J.M. Broto, A. Fert, F. Nguyen Van Dau, F. Petroff, P. Eitenne, G. Creuzet, A. Friederich, and J. Chazelas, *Phys. Rev. Lett.,* 61, 2472 (1988).
7. N.B. Brandt, E.A. Svistova, Soviet Physics Uspekhi 13, 370 (1970).

Вісник ХНУ, серія «Фізика», вип. 24, 2016. с. 20-23

PACS: 78.55.Hx; 82.30.Fi
УДК [548.5:546.655´21-022.532]:544.773.42

Luminescence of F^0 centers in CeO_2 nanocrystals

V. V. Seminko[1]*, P.O. Maksimchuk[1], N. V. Kononets[1], E.N. Okrushko[1], I.I. Bespalova[1], A. A. Masalov[1], Yu. V. Malyukin[1] and Yu.I.Boyko[2]

[1]*Institute for Scintillation Materials of National Academy of Sciences, 60 Lenina Ave, 61001, Kharkiv, Ukraine*
[2]*V. N. Karazin Kharkiv National University, 4 Svobody sq., 61077, Kharkiv, Ukraine*
** Correspondent author: Tel.: +38 057 341 04 87; fax: +38 057 340 32 07.*
seminko@isma.kharkov.ua

In the paper luminescent properties of CeO_{2-x} (ceria) nanocrystals are discussed. Ceria nanocrystals with different oxygen non-stoichiometry were obtained using sol-gel method and subsequent annealing in oxidizing or reducing atmosphere. Luminescence spectra of ceria nanocrystals reveal three types of luminescent centers. Beyond previously observed 4f-5d luminescence of Ce^{3+} ions and charge transfer (CT) luminescence determined by radiative relaxation in Ce^{4+}-O^{2-} complexes, wide luminescence band formed by F^0 centers was revealed. Ratio between luminescent centers of different types can be varied by variation of treatment atmosphere. Luminescence of Ce^{3+} ions is the most intensive in reducing atmosphere due to highest content of oxygen vacancies, and, correspondingly, of Ce^{3+} ions. As CT luminescence of Ce^{4+}-O^{2-} complexes, so luminescence of F^0 centers demonstrate strong quenching with temperature increase; however CT luminescence quenching is more pronounced than quenching of luminescence for F^0 centers.
Keywords: ceria; F-centers; luminescence; nanocrystals.

В статье обсуждаются люминесцентные свойства нанокристаллов CeO_{2-x} (диоксида церия). Нанокристаллы диоксида церия с различной кислородной нестехиометрией были получены при помощи золь-гель метода с последующим отжигом в окислительной или восстановительной атмосфере. Спектры люминесценции нанокристаллов диоксида церия демонстрируют наличие центров люминесценции трех типов. Помимо ранее наблюдаемой 4f - 5d люминесценции ионов Ce^{3+} и полосы с переносом заряда (CT), обусловленной излучательной релаксацией Ce^{4+} - O^{2-} комплексов, выявлена широкая полоса, формируемая F^0 центрами. Соотношение между содержанием центров люминесценции разных типов можно изменять путем варьирования атмосферы отжига. Люминесценция ионов Ce^{3+} наиболее интенсивна при обработке в восстановительной атмосфере благодаря высокой концентрации кислородных вакансий и, соответственно, ионов Ce^{3+}. Как CT люминесценция Ce^{4+} - O^{2-} комплексов, так и люминесценция F^0 центров демонстрирует сильное тушение с возрастанием температуры, однако температурное тушение CT люминесценции выражено сильнее, чем тушение люминесценции F^0 центров.
Ключевые слова: диоксид церия; F-центры; люминесценция; нанокристаллы.

В даній статті обговорюються люмінесцентні властивості нанокристалів CeO_{2-x} (діоксиду церію). Нанокристали діоксиду церію з різною кисневою нестехіометрією були отримані за допомогою золь-гель методу з подальшим відпалом в окислювальній або відновлюючій атмосфері. Спектри люмінесценції нанокристалів діоксиду церія демонструють наявність центрів люмінесценції трьох типів. Окрім 4f - 5d люмінесценції іонів Ce^{3+} та смуги з переносом заряду (CT), обумовленої випромінювальною релаксацією Ce^{4+} - O^{2-} комплексів, що спостерігалися раніше, виявлена широка смуга, сформована F^0 центрами. Співвідношення між вмістом центрів люмінесценції різних типів можна змінювати шляхом варіювання атмосфери відпалу. Люмінесценція іонів Ce^{3+} найбільш інтенсивна при обробці в відновлювальної атмосфері завдяки високій концентрації кисневих вакансій і, відповідно, іонів Ce^{3+}. Як CT люминесценція Ce^{4+} - O^{2-} комплексів, так і люмінесценція F^0 центрів демонструє сильне гасіння зі зростанням температури, однак температурне гасіння CT люмінесценції виражено сильніше, ніж гасіння люмінесценції F^0 центрів.
Ключові слова: діоксид церію; F-центри; люмінесценція; нанокристали.

Introduction

High oxygen storage capacity and ability to switch between Ce^{4+} and Ce^{3+} oxidation states recently has turned the attention of leading material scientists to ceria (CeO_{2-x}) powders and nanocrystals [1-3]. Low $Ce^{4+}\rightarrow Ce^{3+}$ reduction energy and high concentration of oxygen vacancies in ceria lattice seem to be the main prerequisites for the specific properties of nanoceria, so variation of co-dopants and treatment conditions allow obtaining ceria nanocrystals with different oxygen storage and antioxidant properties[4,5].

As was shown in the number of papers [6,7], formation of oxygen vacancies in ceria is accompanied by capture of two electrons by Ce^{4+} ions, which turn in this way to Ce^{3+} ones. However, some recent publications suggested that

electrons can be captured not only by Ce^{3+} ions, but by oxygen vacancies as well, leading to formation of so-called F-centers [8]. Presence of different kinds of F-centers in nanoceria was confirmed in [9] both by EPR and optical spectroscopy methods. Moreover, recently in [10] a new phenomenon of room temperature ferromagnetism for undoped ceria films and nanocrystals was shown and exchange interactions between F-centers were proposed to be the cause of this effect [11]. F-centers can be formed as a result of capture of one (F^+), two (F^0) or no (F^{++}) electrons by oxygen vacancies. While each of these centers has its distinct magnetic and spectroscopic features, clear distinction between F-centers can be made.

Spectroscopic properties of ceria nanocrystals depend on the presence of both Ce^{3+} ions and defect centers. Undoped ceria is a dielectric material with band gap of about 6 eV with valence band formed by 2p states of oxygen, and conduction band formed by mixed 6s+5d states of cerium [12, 13]. Inside the band gap of ceria a narrow band formed by empty $4f^0$ states of Ce^{4+} ions is observed. The distance between the top of the valence band and the bottom of $4f^0$ band is about 3.15 eV.

Steady state and time-resolved luminescence studies shown in our previous papers [14] enable us to distinguish clearly two types of optical centers in undoped ceria nanocrystals formed by Ce^{3+} ions which charge is compensated by oxygen vacancies in NN positions, and Ce^{4+}-O^{2-} charge transfer (CT) complexes, respectively. Also it was determined that ratio between intensities of Ce^{3+} 5d→4f luminescence and CT luminescence in Ce^{4+}-O^{2-} complex depended strongly both on the atmosphere of treatment and size of nanocrystal [15]. Increase of the content of oxygen vacancies either due to treatment in reduction atmosphere or decrease of nanocrystal size led to corresponding increase of Ce^{3+} luminescence intensity as compared to CT band. However, presence of alternative paths of electron behavior after oxygen vacancy formation besides localization on cerium ions, such as formation of F-centers, can complicate sufficiently this rather simple picture. In this paper we show that F-centers (namely, F^0 centers) are inevitably formed in ceria lattice even at treatment in oxidative atmosphere leading to formation of alternative luminescence centers.

Experimental

CeO_2 nanocrystals were obtained by Pechini method [16]. Cerium oxide CeO_2 (99,999%, Sigma-Aldrich) was dissolved in the mixture of nitric acid HNO_3 and hydrogen peroxide H_2O_2 (in 1:1 volume ratio). The solution of 0.75 g of citric acid and 1 ml of ethylene glycol was added to 20 ml of cerium nitrate $Ce(NO_3)_3$ (c = 1 mol/l) solution. The resulting mixture was treated at 80 °C during 10 h and then hydrolyzed by means of 10 mass.% NH_3 water solution (corresponding pH change was from 3 to 7). The precipitate was dried at 120 °C during 5 h and then dehydrated at 250 °C during 4 h. CeO_2 nanocrystals were annealed in oxidative (air) and reducing (hydrogen) atmospheres at 1000°C during 2 h. The corresponding samples are marked in the paper as CeO_2 (Air), and $CeO_2(H_2)$. Average size of nanocrystals was estimated from TEM images and was about 50 nm for all nanocrystals. The structure of the samples corresponds with JCPDS card No.34-0394, so the nanocrystals are characterized by FCC fluorite-type lattice and formation of any additional phases at these conditions can be excluded.

Luminescence spectra were obtained using spectrofluorimeter based on the grating monochromator, luminescence was excited by He-Cd laser (λ_{exc}= 325 nm), diode-pumped solid state laser (λ_{exc}= 457 nm), Ar^+ laser (488 nm) and YAG:Nd laser (532 nm) Investigations were carried out at 293 K and 77 K.

Results and discussion

CeO_2 nanocrystals obtained by the method described in previous section were treated at 1000°C in different atmospheres in order to obtain nanoceria with different concentration of oxygen vacancies, and so, with different content of structural defects. In fig. 1 the luminescence spectra of CeO_2 (Air), and $CeO_2(H_2)$ at 77 K under excitation in the charge-transfer (CT) band (λ_{exc} = 325 nm) are shown. The band with maximum of about 400 nm was observed only for $CeO_2(H_2)$ and as was shown in our previous paper [14] this band is determined by 5d→4f luminescence of Ce^{3+} ions stabilized by oxygen vacancies. Both excitation

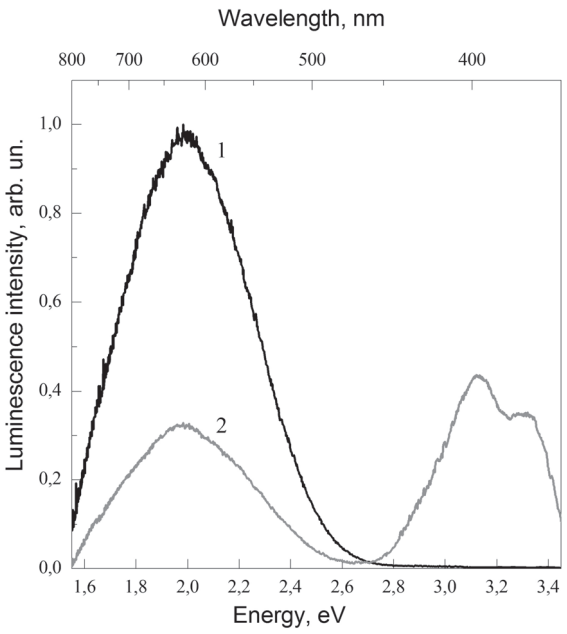

Fig. 1. Luminescence spectra of CeO_2 nanocrystals treated in oxidizing (1) and reducing (2) atmospheres (λ_{exc} = 325 nm), T=300 K.

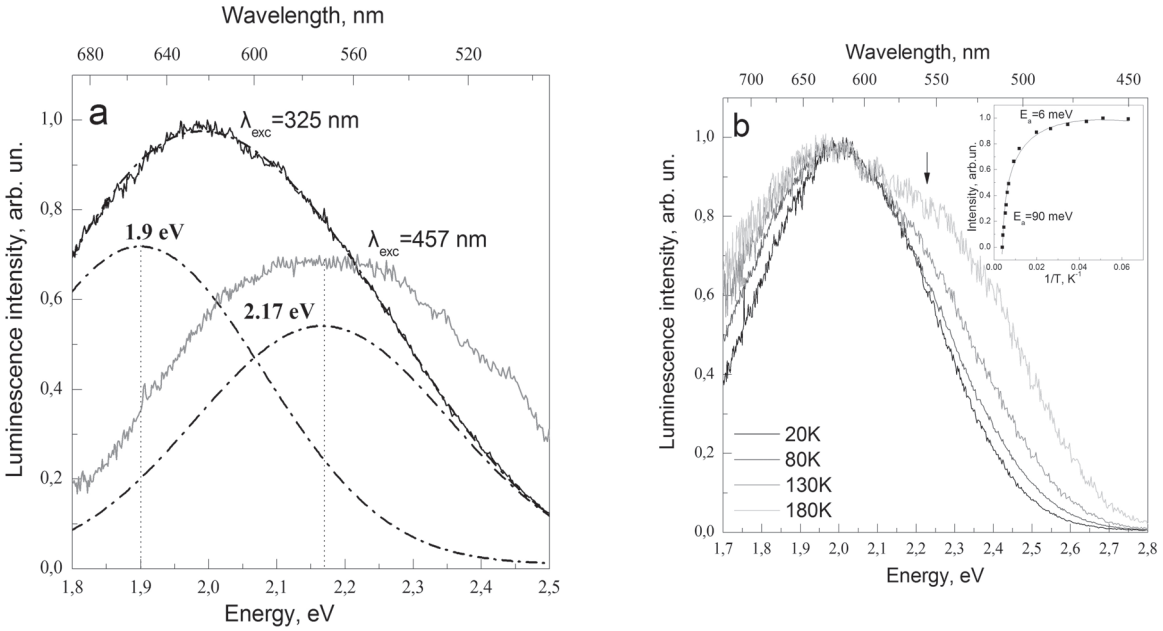

Fig. 2. a) Luminescence spectra of CeO_2 nanocrystals treated in oxidizing atmosphere at λ_{exc} = 325 nm and 457 nm; fitting of luminescence spectrum at λ_{exc} = 325 nm by two Gaussian profiles is also shown. b) Luminescence spectra at λ_{exc} = 325 nm at variation of temperature in the range from 20 K to 180 K normalized by the intensity of 650 nm band. In the inset – temperature dependence of intensity of 570 nm band at 457 nm excitation.

spectrum and typical for Ce^{3+} 5d→4f luminescence decay times in nanosecond range clearly confirm this attribution [14]. At the same time as for stoichiometric, so for non-stoichiometric ceria, wide band with maximum at 620 nm was observed. In [14] it was shown that this band can be attributed to CT-luminescence of Ce^{4+}-O^{2-} charge transfer complex.

More detailed analysis of this band reveals its complex nature (fig. 2a). Fitting of luminescence spectrum obtained at 325 nm excitation at 77 K by two Gaussian profiles reveals two peaks at 1.9 eV (650 nm) and 2.17 eV (570 nm). At 457 nm excitation (with energy lower than the difference between the top of the valence band and bottom of $4f^0$ band) the 650 nm sub-band disappears and spectrum consists of the band with maximum at 570 nm. The same luminescence spectra as for 457 nm excitation were observed at different excitations with energies below optical gap (488 nm and 532 nm). The fact that 650 nm sub-band can be excited only at $2p^6$→$4f^0$ excitation allows to attribute it to CT-luminescence of Ce^{4+}-O^{2-} charge transfer complex, while 570 nm band must have some different origin. These sub-bands exhibit sufficiently different temperature dependences (fig. 2b) – intensity of 650 nm band is comparable with intensity of 570 nm one only at low temperatures (less than ~100 K), while at room temperature its contribution to total intensity of complex 620 nm band is negligible. The 570 nm sub-band also exhibit temperature quenching but this quenching is sufficiently weaker than for 650 nm one. So, it must be concluded that 620 nm band consists of two sub-bands with different origin – while luminescence band at 570 nm can be excited as via CT excitation band, so directly by 457

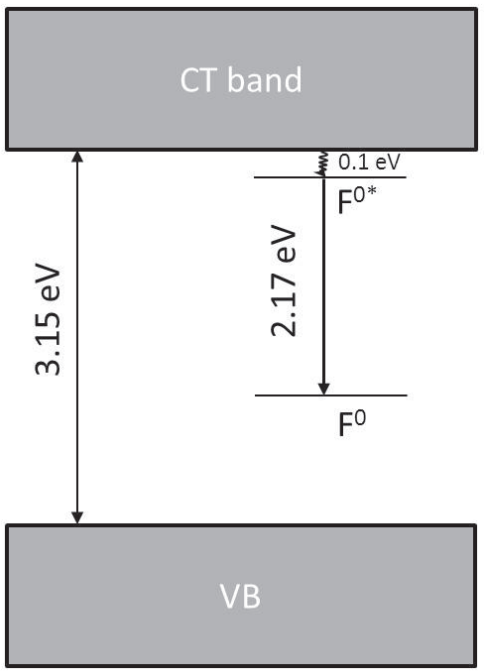

Fig. 3. Energy scheme for CeO_2 showing the positions of F^0 and F^{0*} levels in the band gap of ceria (VB – valence band, CT – charge transfer ($4f^0$) band).

nm excitation and probably has the defect-related nature, luminescence band at 650 nm can be excited only via CT band and so can be ascribed to luminescence in Ce^{4+}-O^{2-} charge transfer complex.

Fitting the temperature dependence of 570 nm (defect-related) band intensity by $I = I_0(1 + B_1 e^{-\frac{E_1}{kT}} + B_2 e^{-\frac{E_2}{kT}})^{-1}$ (fig.2b, inset) allows determining the activation energy in the low and high-temperature ranges: 6 meV and 90 meV, respectively. These values are in good agreement with the correspondent values of activation energy for F^0 centers in ceria nanocrystals obtained by precipitation method in [9]. Also the maximum of luminescence band for F^0 centers determined in [9] (2.1 eV) is close to the maximum of defect band for our nanocrystals (2.17 eV). So, the 570 nm band is most probably related to transitions in F^0 centers ($F^{0*} \rightarrow F^0$).

The most probable pathway of $F^{0*} \rightarrow F^0$ luminescence quenching is the one with participation of the bottom of $4f^0$ (CT) band. So the activation energy of 570 nm band luminescence quenching at room temperature (90 meV) can be associated with energy difference between F^{0*} level and the bottom of $4f^0$ band. This supposition allows us placing F^0 and F^{0*} levels in the band gap of ceria (fig.3).

Conclusions

1. Luminescence spectra of ceria nanocrystals at 325 nm excitation consist of two luminescence bands: the first one is determined by 4f-5d luminescence of Ce^{3+} ions and second one is complex consisting of two sub-bands: charge transfer (CT) luminescence band and luminescence band formed by F^0 centers.

2. Both CT luminescence band and F^0 luminescence band are temperature-dependent, however temperature quenching of F^0 luminescence band is less pronounced, than temperature quenching of CT luminescence which at room temperature almost disappear.

3. Temperature quenching of F^0 luminescence is realized with participation of the bottom of $4f^0$ band. Energy difference between excited F^{0*} level and bottom of $4f^0$ band is about 0.1 eV.

References

1. A. Trovarelli. Catalysis by Ceria and Related Materials, World Scientific Publishing Company, New York (2002), 908 p.
2. S. Bedrane, C. Descorme, D. Duprez. Catalysis Today, 75(1), 401 (2002).
3. M. Das, S. Patil, N.Bhargava, J.F. Kang, L.M. Riedel, S. Seal, J.J. Hickman. Biomaterials, 28(10), 1918 (2007).
4. E. Aneggi, M. Boaro, C. de Leitenburg, G. Dolcetti, A. Trovarelli. Journal of Alloys and Compounds, 408, 1096 (2006).
5. C. Korsvik, S. Patil, S. Seal, W. T. Self. Chemical Communications, 10, 1056 (2007).
6. N.V. Skorodumova, S.I. Simak, B.I. Lundqvist, I.A. Abrikosov, B. Johansson. Physical Review Letters, 89(16), 166601 (2002).
7. H. Olle, N.V. Skorodumova and S.I. Simak. Physical Review Letters, 108(13), 135504 (2012).
8. B. Vodungbo, F. Vidal, Y. Zheng. Journal of Physics: Condensed Matter, 20(12), 125222 (2008).
9. S. Aškrabić, Z. D. Dohčević-Mitrović, V. D. Araújo, G. Ionita. Journal of Physics D: Applied Physics, 46(49), 495306 (2013).
10. X. Han, L. Jaichan, and Y. Han-Ill. Physical Review B, 79(10), 100403 (2009).
11. V. Ferrari, A.M. Llois, and V. Vildosola. Journal of Physics: Condensed Matter. 22(27), 276002 (2010).
12. C.W.M. Castleton, J. Kullgren, K. Hermansson. Journal of Chemical Physics, 127(24), 244704 (2007).
13. F. Goubin, X. Rocquefelte, M.H. Whangbo, Y. Montardi, R. Brec. Chemistry of Materials, 16(4), 662 (2004).
14. A. Masalov , O. Viagin, P. Maksimchuk, V. Seminko, I. Bespalova, A. Aslanov, Yu Malyukin, and Yu Zorenko. Journal of Luminescence, 145, 61 (2014).
15. P.O. Maksimchuk , V.V. Seminko, I.I. Bespalova, A.A. Masalov. Functional Materials, 3, 255 (2014).
16. A. Serra, V. Severino, P. Calefi, S. Cicillini. J. Alloys Compd, 323, 667 (2001).

Вісник ХНУ, серія «Фізика», вип. 24, 2016. с. 24-29

UDK 539.374+669.715
PACS numbers: 62.20.Fe, 62.20.Hg

Superplastic deformation of high strength aluminum alloy 1933 after hot working

A.V. Poyda[2], A.V. Zavdoveev[3,4], V.Yu. Dmitrenko[4], V.P. Poyda[1], V.V. Bryukhovetskiy[2], D.E. Milaya[2], R.V. Sukhov[1], O. O. Minyenkov[1]

[1)] V.N. Karazin Kharkov National University
Svoboda square, 4, Kharkov, Ukraine, 61077
[2)] Institute of Electrophysics & Radiation Technologies NAS of Ukraine
Chernyshevskaya St. 28, P.O. Box 8812, Kharkov, Ukraine, 61002
[3)] Paton Electric Welding Institute of NAS of Ukraine
Bozhenko St., 11, Kiev, Ukraine, 03680
[4)] Donetsk Institute for Physics and Engineering named after A.A. Galkin NAS of Ukraine
Nauky Prosp., 46, Kiev, Ukraine, 03028

The structural state of the specimens of industrial alloy 1933, passed previous hot working processing, is investigated. It is found, that the microstructure has considerable anisotropy. The grains, elongated in the rolling direction, dominate in it. The specific proportion of low-angle grain boundaries and high-angle grain boundaries in specimens after hot working is determined. The optimal conditions of superplastic deformation in specimens past previous hot working are determined.
Keywords: superplasticity, hot working, grain boundaries, structural anisotropy.

Исследовано структурное состояние образцов промышленного сплава 1933, прошедшего предварительную термомеханическую обработку. Установлено, что микроструктура обладает значительной анизотропией. Зерна, удлиненные в направлении прокатки, преобладают в ней. Определена удельная доля малоугловых и большеугловых границ зерен в образцах после термомеханической обработки. Определены оптимальные условия проявления сверхпластической деформации в образцах прошедших предварительную термомеханическую обработку.
Ключевые слова: сверхпластичность, термомеханическая обработка, границы зерен, структурная анизотропия.

Досліджено структурний стан зразків промислового сплаву 1933 що пройшов попередню термомеханічну обробку. Встановлено, що мікроструктура має значну анізотропією. Зерна, видовжені в напрямку прокатки, переважають в ній. Визначено питому частка малокутових і багатокутових меж зерен в зразках після термомеханічної обробки. Визначено оптимальні умови прояву надпластичної деформації в зразках, що пройшли попередню термомеханічну обробку.
Ключові слова: надпластичність, термомеханічна обробка, межі зерен, структурна анізотропія.

Introduction

In [1-5], it was found that the forging high strength alloy 1933 of the system Al-Zn-Mg-Cu-Zr with the original bimodal grain structure showed the effect of high-temperature structural superplasticity (HTSP) in a solid-liquid state. The initial structure of industrial semi-finished alloy 1933 consisted of large poligonized unequiaxed grains that surrounded areas, consisting of ultrafine equiaxed grains. In [5] the specific proportion of grain boundaries in the initial misorientation of various 1933 alloy specimens, prepared for mechanical testing was determined. It was found that the specific proportion of low-angle boundary (LAB) grains for the tested area was 65.5% and the specific proportion of high-angle boundary (HAB) grains was 35.5%. It was shown [1-5] that the grain boundary sliding (GBS) occurs in the specimens during superplastic deformation (SPD). It occurs not only on the boundaries of ultra-fine grains, but also on the boundaries of coarse poligonized grains, oriented parallel to the stretch axis. On the basis of generalization of the results obtained in the work, and taking into account the data available in the literature, the analysis of development of the deformation and accommodative mechanisms of SPD of this alloy is conducted [5].

Since 1933 alloy is increasingly used in aircraft construction, in particular for the manufacture of load-bearing aircraft fuselage [6], it was necessary to continue research aimed at improving of its superplastic

characteristics. These improvements, in particular, could be achieved if it were possible to create a uniform ultrafine structure in the original alloy specimens. As it has been shown in [7], the implementation of static recrystallization does not provide the formation of homogeneous nonpoligonized grain structure and does not eliminate bimodality in the alloy 1933 of Al-Zn-Mg-Cu-Zr system, it was necessary to conduct studies aimed at using of other methods of forming of ultrafine homogeneous structure in the specimens of high-strength aluminum alloy, by selecting them from the set of those techniques that are traditionally used for its creation in multicomponent aluminum alloys [8-11]. The aim of research, the results of which are described in this article was to determine the effect of pre-thermomechanical processing, carried out as a result of cold rolling of pre-annealed industrial semi-finished alloy 1933 specimens on their structural condition, as well as improving of performance of superplasticity of the alloy specimens by creating in them firstly fibrous structure, and then uniform ultra-fine microstructure instead of bimodal structure.

Materials and methods of the experiment

Investigated in the paper alloy 1933 has such a chemical composition (1,6 – 2,2% Mg; 0,8 – 1,2% Cu; 0,1% Mn; 0,66 – 0,15% Fe; 0,1% Si; 6,35 – 7,2% Zn; 0,03 – 0,06% Ti; 0,05% Cr; 0,10 – 0,18% Zr; 0,0001 – 0,02% Be; base Al, % wt.) [5]. The main alloying elements in the alloy are magnesium, zinc and copper. They play a fundamental role in the partial melting of superplastic aluminum alloys and as a result, creating small amounts of viscous liquid phase at the grain boundaries during deformation [12-13].

Cold rolling of the pre-annealed for 2 hours at a temperature of 500°C specimens was carried out on the mill BMC-64-2BУ2C so that the accumulated amount of deformation was e = 1.3.

In the initial state the hardness of semi-finished alloy 1933 was HV – 126 HV, after annealing it was equal to 56, and after the cold rolling HV - 126.

Mechanical tests of the alloy specimens, prepared from industrial intermediates, held in air by stretching them in creep mode at constant flow stress according to the procedure described in details in [14].

Grain structure, cavity morphology and morphology of fibrous in specimens were studied using light microscopy (MIM-6 with the digital camera Pro-MicroScan) and scanning electron microscopy (JEOL JSM-840), and standard techniques of quantitative metallography [15].

To determine the proportions of ultrafine and coarse grains, the grain boundary misorientation angles and to make quantitative assessment of their content in the alloy 1933 the electron backscatter diffraction analysis (EBSD) was used [16]. Investigations were performed using a scanning electron microscope JEOL JSM-6490LV, equipped with energy dispersive spectrometry INCA Penta FETx3 and by detector of backscattered electrons Nordlys S. Analysis of the obtained structures was performed according to the procedure described in [16], using software HKL Channel 5, which is included in the set of technical documents to the microscope.

The surface of the working part of the specimens was subjected to grinding and to mechanical polishing. Surface finishing of sections for metallographic investigations was carried out using a diamond paste grit 1/0.

Specimens which were used for EBSD analysis were subjected to electropolishing. It was performed in a solution of such composition: 40 wt. % H_2SO_4, 45 wt. % H_3PO_4, 3 wt. % CrO_3, 11 wt. % H_2O [16]. Mode of operation: operating temperature 60-80°C, the anode current density, the voltage of 15-18 V, exposure – a few minutes.

To reveal the grain boundaries during the metallographic studies was used universal chemical etchant of such a composition: 17 ml HNO_3, 5 ml HF, 78 mL H_2O.

In addition to the chemical etching for revealing of grain boundaries of the working part surface of the test specimens of alloy as the initial one, and superplastically deformed to a certain degree of deformation, strain relief method was used.

To determine the contribution of grain boundary sliding (GBS) in the overall deformation and for studying of the kinetics of its development at different stages of SPD used a method of marker scratches. On the polished specimens using a diamond paste of dispersion 3 microns, the marker risks parallel to the axis of their subsequent direction of stretching were applied. Mechanical testing was carried out using specimens in a HTSP in the creep mode, which led to the formation on the surface of polished specimens of a deformation relief as a result of a small (3-5%) deformation. The views of it were studied.

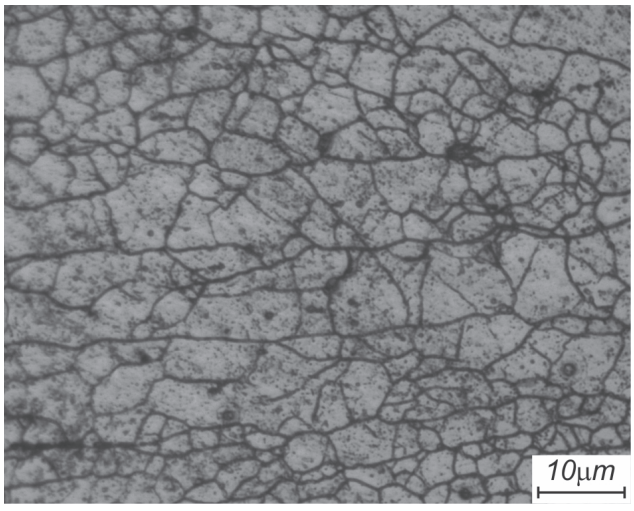

Fig.1. Typical view of the initial microstructure of the specimen of alloy 1933 in the initial state. Light microscopy.

The average grain size ⟨*d*⟩ was determined by light microscopy photomicrographs with use of random secant method [15].

Results and discussion

Figure 1 shows a micrograph of a typical view of the initial microstructure of the specimen of alloy 1933, obtained using optical microscopy techniques. The microstructure of the alloy is bimodal. It consists of areas containing a large number of recrystallized ultrafine grains with ⟨d⟩ = 7 ± 1 *μm*, divided by high-angle grain boundaries and contain some coarse elongated poligonized grains with ⟨d⟩ = 50 ± 1 *μm*, divided by low-angle grain boundaries [5].

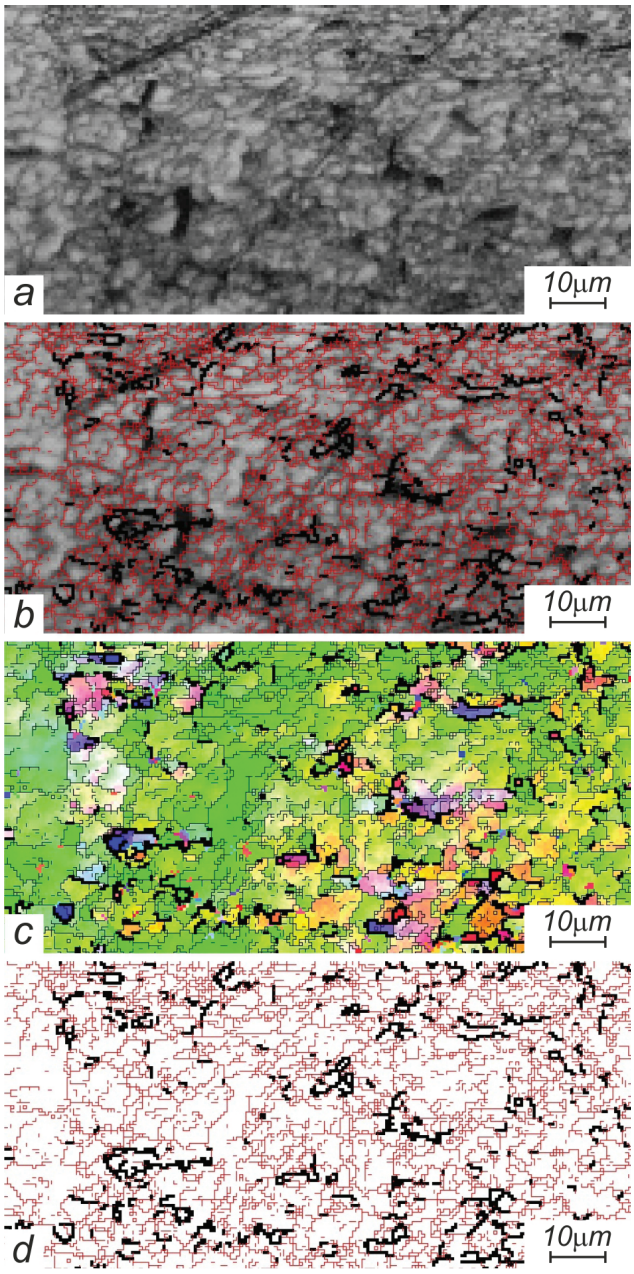

Fig.2. Cards of EBSD analysis: a – chosen fragment, b – card obtained as a result of combination of card of contrasts and of card of grain boundary misorientation; c, d – cards of grain boundary angles orientation.

As indicated in [7] a small amount of nonequilibrium eutectic constituents (Quasi-binary, ternary and quaternary eutectics), consisting of a mixture of crystals of a solid solution based on aluminum (α_{Al}) and intermetallic particles of T-phase, η-phase and S-phase are present in almost all industrial semifinished alloy 1933 which passed thermomechanical processing. It is characteristic for alloys of Al-Zn-Mg-Cu-Zr [6].

It is found that the stitch inclusions of intermetallic phases are mainly localized at the grain boundaries, which are parallel to the rolling direction. In grains the inclusions, which are scopes of mentioned above particles and the particles of ultrafine β'-phase (Al_3Zr) are present in grains. β'-phase (Al_3Zr) effectively inhibits the growth of the grains in multi superplastic aluminum alloys at high homologous temperatures [8-10]. After hot working of the alloy 1933, performed in this study, the analysis of microstructure was conducted using EBSD techniques. Figure 2, a shows a fragment of the working part of specimen that has been used for EBSD analysis of the structural state of the alloy in the investigated part of the surface of cold-rolled alloy specimen of 1933. It is seen that the structure of the alloy is homogeneous submicrocrystalline. On fig.2, b there is EBSD card, obtained as a result of combination of chosen for investigations fragment and of card of grain boundary misorientation. On fig.2, c, d cards of grain boundary angles orientation are shown. These cards were used for determination of the specific proportion of low-angle grain boundaries (LAB) and high-angle grain boundaries (HAB) for the investigated fragment of surface of specimen of alloy 1933.

Figure 3 shows the dependence of the relative amounts of different grain boundaries from misorientation

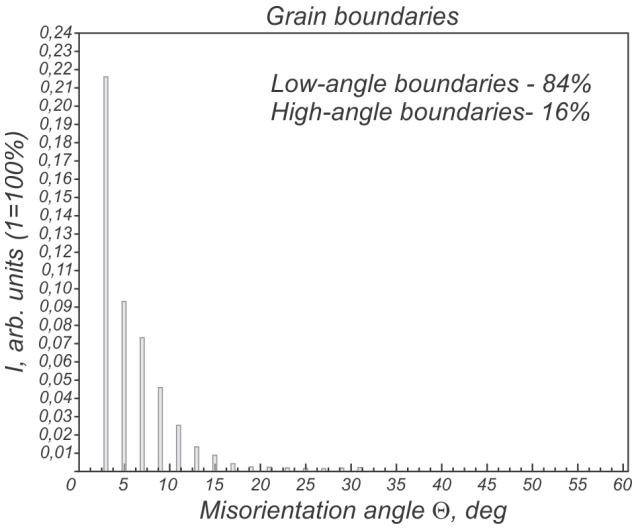

Fig.3. Relative amounts of the grain boundaries of the different misorientation from misorientation angle for the tested area of the specimen' surface after hot working.

angle for the tested area of the specimens' surface of alloy 1933 after hot working. This quantitative distribution of the disorientation angles of the grain boundaries was constructed as a result of accounting of all certified grain boundaries present in the tested specimen of alloy 1933.

When building this relationship was usually to attribute to the LAB grains those grain boundaries, which have misorientation angle below 10°, and to attribute to the to HAB - those grain boundaries, which are misoriented above 10° [16]. It is found that the specific proportion of LAB grains for the tested area is 84.0% and the specific proportion of HABs grains is 16.0%.

As a result of the mechanical tests performed in the creep mode at a constant strain stress it is found that specimens of the alloy 1933, subjected to preliminary hot working exhibit the effect of high-temperature structural superplasticity (HTSP). The optimal conditions of its performance is such: temperature T = 500°C, flow stress σ = 4.5 MPa. The maximum relative elongation of specimens to failure δ = 410%. Strain rate is $2{,}2 \cdot 10^{-3}$ s^{-1}.

Elongation to failure and the true strain rate in the specimens with a homogeneous fine-grained structure, previously passed thermomechanical treatment, is higher than that for the initial 1933 alloy specimens with bimodal structure [1-5].

Fig.4. General view of the specimen of alloy 1933, previously passed hot working, deformed to failure in mode of superplasticity in optimal conditions to 410% in comparison with the initial.

Fig.4 shows the general view of the specimen of alloy 1933, previously passed hot working, deformed to failure in mode of superplasticity in optimal conditions to 410% in comparison with the initial one. It's seen that the superplastic deformation of the specimen performed homogeneously and steadily on the macroscopic level. This is proved by the fact that the specimen's failure was quasibrittle without forming a distinct neck.

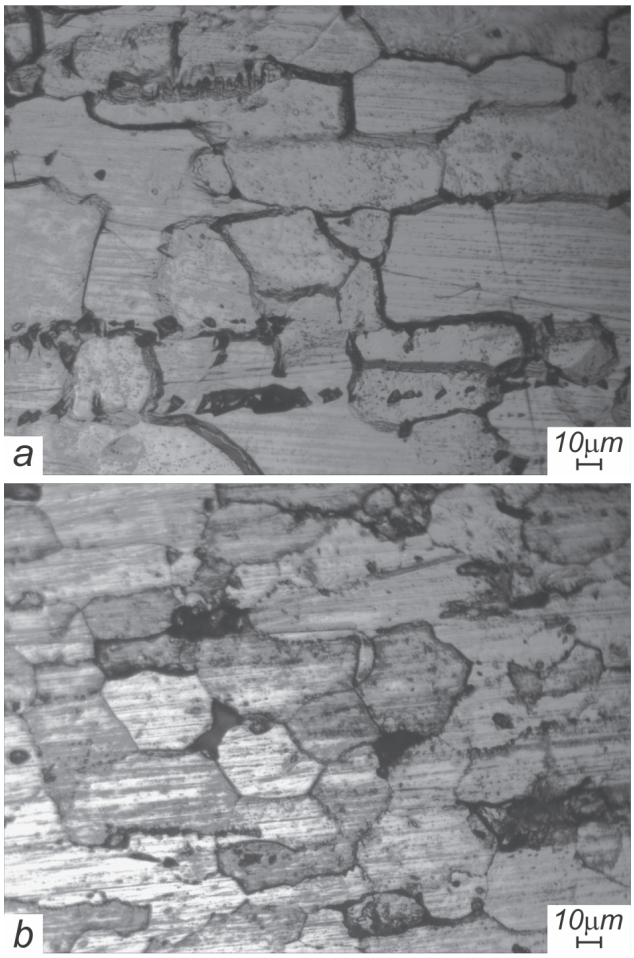

Fig.5. The typical view of the microstructure of the working part of specimen: a - heated to a test temperature T = 500°C, b - superplastically deformed to failure under the optimal conditions. Light microscopy.

Fig.5 shows the typical view of the microstructure of the working part of specimen heated to a test temperature T = 500°C and superplastically deformed to failure under the optimal conditions. Their analysis showed that as a result of a preliminary thermomechanical processing of semifinished alloy 1933 bimodality was eliminated and a uniform ultrafine grain structure having an average size d = 15 μm formed. It made possible to increase the phenomenological parameters characterizing the superplastic properties of the alloy.

It can be assumed that a certain amount of intermetallic phases localized at the grain boundaries, is dissolved in the aluminum-based solid solution during heating of the specimen to a test temperature and directly during the superplastic deformation. Not had time to dissolve intermetallic and non-equilibrium components to which they belong, as well as the border edge grains in which, as shown in [4] in a solid solution based on aluminum contains increased compared to the nominal alloy composition concentration of zinc atoms and magnesium act as centers of partial melting of the alloy. As a result, plots occupied

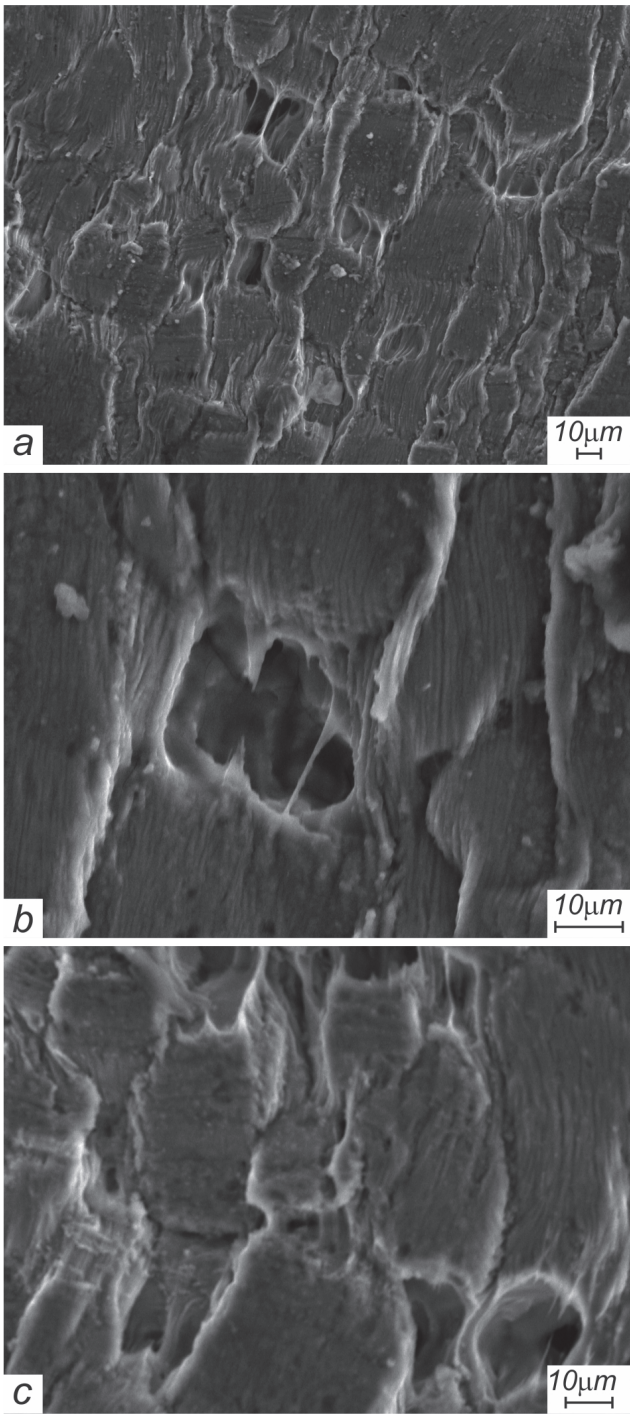

Fig.6. Typical views of deformation relief formed on the surface of the working part of specimens of the alloy 1933 superplastically deformed to fracture under the optimal conditions. Scanning electron microscopy.

by a metastable liquid phase, necessary for active and facilitated the development of HTSP accommodative processes [17-23] are formed on the grain boundaries.

As a result of detailed studies of specific views of strain relief formed on the surface of the working part of the alloy 1933 specimens superplastically deformed to failure performed using scanning electron microscopy, fibrous structures were found (see. fig.6). They formed and developed during the superplastic deformation in near-surface grain boundary pores and microcracks of grain.

It is considered [17-22] that the formation and development of such structures is an indirect confirmation of the fact that the 1933 alloy during superplastic deformation is in the solid-liquid state due to its partial melting. The study of specific types of strain relief found that the ends of long fibers (see. Fig.6, a, b) connect the surface of grain boundary cavities and cracks formed in the course of GBS in the separation of grains from each other along the boundaries, approximately perpendicular to the strain direction, and short fibers form a fringe on the edges of the grains (see. Fig.6, c).

The number of fibers found in the near-surface grain boundary cavities is different. Apparently, it depends on the amount of metastable liquid phase localized at the grain boundaries perpendicular to the strain direction of the specimen.

On the surface of the fibers and grains to which they are connected, friable oxide film are detected. This suggests that during SPD in specimens of alloy 1933 at a test temperature T = 500°C, in its working part the dynamic oxidation of the surface of the specimen and the inclusions of a metastable liquid phase, which in a small amount are present at the grain boundaries and in the boundary edges of slipping grains intensively occured. The dynamic oxidation led to the formation of oxides of Al_2O_3, MgO and magnesia spinel $MgAl_2O_4$, consisting of the oxides, which are the most common for multicomponent aluminum alloys doped with Mg [23]. Saturation of metastable liquid phase by particles of magnesium and aluminum oxides is apparently led to the formation of liquid-solid material with higher viscosity [24], viscous flow of which occured due to the disclosure of grain boundary cavities during the development of GBS in the SPD of specimens of alloy 1933. It, in its turn, led to the formation and development of the fibrous structures according to the mechanism described in [3].

This work is done with partial support by the target complex program "Fundamental Problems of Creation of New Nanomaterials and Nanotechnologies", project №62/16-N.

Conclusions

1. The structural state of the specimens of industrial alloy 1933, passed previous hot working, is investigated. It is found, that the microstructure has considerable anisotropy. The grains, elongated in the rolling direction dominate in it.

2. The specific proportion of grain boundaries of different misorientation in specimens of alloy 1933 passed hot working is determined. It is found that the specific proportion of the low-angle grain boundaries is 84% and the specific proportion of high-angle grain boundaries is 16%.

3. It is shown that a uniform equiaxed grain structure with an average grain size of d = 15 microns in specimens of alloy 1933 previously past thermomechanical processing, forms in the early stages of superplastic deformation.

4. It is found that the specimens of alloy 1933 previously past thermomechanical processing exhibit the effect of high temperature structural superplasticity. Optimal conditions for its manifestation are: temperature T = 500°C, flow stress σ = 4,5 MPa. The maximum relative elongation of the specimens to failure δ, superplastically deformed under T = 500°C, σ = 4,5 MPa under the true strain rate $2{,}2\cdot10^{-3}$ s^{-1} reached 410%.

5. In the process of superplastic deformation of the specimens of alloy 1933 with an ultrafine grain boundary structure the fibrous structures form and develop in the surface cavities and intergranular cracks as a result of their disclosure during the development of grain boundary sliding.

References

1. D.E. Pedun, V.P. Poyda, T.F. Sukhova, A.P. Samsonik, V.V. Litvinenko, E.L. Spiridonov. Visnyk KhNU, seriia «Fizyka». V.16, №1019, 63 (2012).
2. D.E. Pedun, V.P. Poyda, V.V. Bryukhovetskiy, A.V. Poyda, A.P. Kryshtal', T.F. Sukhova, A.L. Samsonik, V.V. Litvinenko, E.K. Spiridonov. Metallofizika i noveyshie tekhnologii, V.34, №10, 1397 (2012).
3. V.P. Poyda, D.E. Pedun, V.V. Bryukhovetskiy, A.V. Poyda, R.V. Sukhov, A.L. Samsonik, V.V. Litvinenko. FMM, V.114, №9, 779 (2013).
4. D.E. Pedun, V.P. Poyda, V.V. Bryukhovetskiy, A.V. Poyda, R.V. Sukhov, A.P. Kryshtal'. Visnyk KhNU, seriia «Fizyka», V.18, №1075, 55 (2013).
5. A.V. Poyda, A.V. Zavdoveev, V.P. Poyda, V.V. Bryukhovetskiy, D.E. Milaya, R.V. Sukhov. Visnyk KhNU, seriia «Fizyka», V.22, №1158, 23 (2015).
6. V.M Beleckii, G.A. Krivov. Alyuminievye splavy (sostav, svoistva, tehnologiya, primenenie) spravochnik / Pod obshei redakciei akademika RAN I.N. Fridlyandera. K.: Kominteh. 2005, 315p.
7. V.I. Elagin. V.V. Zakharov, M.M. Drits. Struktura i svoystva splavov sistemy Al-Zn-Mg. M.: Metallurgiya (1982), 224s.
8. I.I. Novikov, V.K. Portnoy. Sverkhplastichnost metallov i splavov s ultramelkim zernom. M.: Metallurgiya, (1981), 168s.
9. O.A. Kaybyshev. Sverkhplastichnost promyshlennykh splavov. M.: Metallurgiya, (1984), 264s.
10. Superplastic Forming of Structural Alloys, Ed. by N.E. Paton and C.H. Hamilton. The Metallurgical Society of AIME, San Diego, California, (1982), 312p.
11. V.N. Shcherba. Pressovanie alyuminievykh splavov. M.: Intermetinzhiniring, (2001), 768s.
12. M. Mabuchi, H.G. Jeong, K. Hiraga, K. Higashi. Interface Sci. V.4, №3 – 4, 357 (1996).
13. I.I. Novikov, V.K. Portnoy, V.S. Levchenko, A.O. Nikiforov. Mater. Sci. Forum. Vol.243 – 245, 463 (1997).
14. V.P. Poyda, R.I. Kuznetsova, T.F. Sukhova, N.K. Tsenev and others. Metallofizika, V.12, №1, 44 (1990).
15. S.A. Saltykov. Stereometricheskaya metallografiya. M.: Metallurgiya, (1976), 272 s.
16. V.N. Varyukhin, E.G. Pashinskaya, A.V. Zavdoveev, V.V. Burkhovetskiy. Vozmozhnosti metoda difraktsii obratnorasseyannykh elektronov dlya analiza struktury deformirovannykh materialov. K.: Naukova dumka, (2014) 101s.
17. C.L. Chen, M.J. Tan. Mater. Sci. and Eng. A., 298, 235 (2001).
18. W.D. Cao, X.P. Lu, H. Conrad. Acta. Mater., 44, №2, 697 (1996).
19. Higashi K., Nieh T.G., Mabuchi M., Wadsworth J. Scripta Met. et Mater., V.32, N7. 1079 (1995).
20. W.J.D. Shaw., Materials Letters, 4, 1 (1985).
21. V.P. Poyda, V.V. Bryukhovetskiy, R.I. Kuznetsova, A.V. Poyda // Visnyk SumDU, V76, №4, 5 (2005).
22. V.P. Poyda, V.V. Bryukhovetskiy, A.V. Poyda, R.I. Kuznetsova, V.F. Klepikov, D.L. Voronov // FMM, V.103, №4, 433 (2017)
23. Chang Jung-Kuei. Effects of atmosphere in filament formation on a superplastically deformed aluminum–magnesium alloy / Jung-Kuei Chang, Eric M. Taleff, Paul E. Krajewskib and James R. Ciulika // Scripta Materialia 60. –2009. P.459–462.
24. A.M. Korolkov Liteynyie svoystva metallov i splavov. M.: Nauka, (1967). 199s.

Вісник ХНУ, серія «Фізика», вип. 24, 2016. с. 30-35

81.05.Je; 82.45.Qr; 81.15.Pq; 82.45.Yz
УДК 542.943:620.18

Synthesis by method of electro consolidation of SiC and WC, ZrO_2 nanocomposite materials with the high mechanical properties

E.S. Gevorkyan[1], G.D. Semchenko [3], M.V.Kislitsa[1],
V.A.Chishkala[2], S.R. Vovk[2], R.V.Vovk[2]

[1] *Ukrainian State University of Railway Transport, Feuerbach Square, 7, Kharkov, Ukraine, 61002*
[2]*National Technical University "Kharkov Polytechnic Institute", Frunze Street 21, Kharkov, Ukraine, 61002*
[3]*V.N. Karazin Kharkov National University, Svobody sq. 4, Kharkov, Ukraine, 61022*
[1] *edsgev@gmail.com,*[2]*r.vovk@mail.ru,* [3] *sgd@kpi.kharkov.ua,*

Application of modern ways of ceramic mater ials' consolidation and association of synthesis methods of organic and inorganic chemistry, sol-gel method and mechanochemistry, allowing to control processes of synthesis of the defined phases at molecular level, gives the chance to create highly effective composite materials.

Keywords: mechanochemistry, nanoparticles, synthesis of β-SiC, nanopowder, ZrO_2–3 wt. % Y_2O_3, WC, properties, K1C, consolidated composite materials

Застосування сучасних способів консолідації керамічних матеріалів і об›єднання методів синтезу органічної і неорганічної хімії, золь-гель методу і механохімії, що дозволяють контролювати процеси синтезу заданих фаз на молекулярному рівні, дає можливість створювати високоефективні композиційні матеріали.

Ключові слова: механохімія, наночастинки, синтез β-SiC, нанопорошки, ZrO_2–3 wt. % Y_2O_3.

Применение современных способов консолидации керамических материалов и объединение методов синтеза органической и неорганической химии, золь-гель метода и механохимии, позволяющих контролировать процессы синтеза заданных фаз на молекулярном уровне, дает возможность создавать высокоэффективные композиционные материалы.

Ключевые слова: механохимия,наночастицы,синтез β-SiC,нанопорошки, ZrO_2–3 wt. % Y_2O_3.

Introduction

The modern stage of development of science and technology is characterized by considerable achievements in the field of creation of the composite materials (CM). In modern development of high technologies the mixing of components at molecular level and creation of CM with disperse, nanosized and fibrous inclusions are the main tendencies in ceramic materials science. Therefore the mechanochemistry and sol-gel process which allow to project, create and control the properties of materials and products from them, are the most perspective directions for developing of new technological decisions and new materials with the defined properties. Results of use of the specified tendencies for creation of perspective composite materials have been presented in the report [1, 2, 3, 4].

One of the characteristics of creation method of the CM nanostrengthened by nanoparticles and nanofibres of β-SiC and Si_3N_4 is self-organization of gel structures and the purposeful organization of nanoreactors for synthesis of nanoparticles and nanofibres of the specified compounds. In nanoreactors by means of physical impacts (temperature and pressure) it is possible to operate processes of chemical transformations of tetraethoxysilane and the subsequent self-organization of radicals ($–CH_3$) in gel clusters of β-cristobalite structures into organo-inorganic complex ($–CH_3$)–$(SiO_2)_n$. This complex is a precursor of components for synthesis of nonoxygen compounds, first of all, β-SiC at low temperatures. Low-temperature synthesis of SiC, according to thermodynamic calculations [5–8], is possible only from such components as carbon and silicon monoxide.

At $P_{SiO} = 10^{-19} – 10^{-12}$ atm. and P_{CO}/P_{CO2} = 9:1 – 8:2 synthesis of SiC can be carried out at a temperature below 700 K that is confirmed experimentally [6, 7] in the course of thermodestruction of gels and modification of powders of refractory compounds for CM at their milling with silicon alkoxide. Mechanisms of low-temperature synthesis of β-SiC in the course of mechanochemical activation of powders at milling with silicon alkoxide and at heat treatment of gels on its basis are identical.

During modification of powder of any refractory filler at milling with an additive of silicon alkoxide the nucleation

and synthesis of β-SiC nanoparticles have been observed, as well as systematic and nonsystematic violations of crystal lattices of fined powders that intensify sintering of refractory powders for producing of CM.

Use of the modified by silicon alkoxide powders of α-SiC, B_4C, Si_3N_4 and Al_2O_3 as fillers of ceramic matrixes led to creation of hot-pressed crack-resistance ceramics, the corundum coatings for protection of graphite from oxidation with the intermediate layer nanostrengthened by β-SiC, nanostrengthened carbon-graphite and silicon carbide CM [9].

Use of nanoparticles of WC and partially stabilized by yttrium oxide nanoparticles of ZrO_2 allows to get by method of hot pressing at a direct transmission of current through graphite form a thin microstructure of composites with high physicomechanical properties. This process has been carried out on specially developed apparatus for hot pressing [10].

Apparatus and Procedures

Consolidation of composite materials on the basis of powders of nonoxygen compounds has been carried out by well-known method of hot pressing at temperatures of 1873–2573 K (30 min.). Hot pressing of ZrO_2 has been carried out by means of the developed apparatus of hot pressing with application of the high-ampere current at a transmission it through a graphite compression mold [10] at a temperature of 1473–1673 K and rate of temperature raise 400 degrees/min.

The phase composition of the modified powders and the developed materials on their basis, the size of grains of the synthesized phases, properties of samples have been determined by known methods. Structure of SiC materials has been studied using a polarizing microscope MIN–8 and an electronic microscope Jeol. The X-ray phase analysis has been carried out on the diffractometer DRON–3M at Cu_{Ka} radiation.

Phase structure of the received samples of ZrO_2–Y_2O_3–WC has been investigated by method of the X-ray phase analysis (the Rigaku Ultima IV diffractometer ($Cu_{K\alpha}$ – radiation, Ni – filter). For definition of exact element composition of material the X-ray spectral analysis with use of a raster ion-electronic microscope of Quanta 200 3D has been made. Definition of a form and the sizes of powders' particles has been carried out with usage of a transmission electron microscope JEM–2100.

Structure research of the sintered specimens on the basis of partially stabilized zirconium dioxide has been carried out by methods of power probe (atomic power Ntegra Aura microscope) and raster microscopy (a raster ion-electronic microscope of Nova NanoSEM). Microhardness of ceramics' samples has been determined by the automatic AFFRI DM8 microhardness tester by Vickers's method with application of 1 kg loading within 15 seconds.

Monoaxial compression tests of materials' samples have been carried out at the room temperature on the air by means of the test machine Instron 300LX.

Results and discussion

For creation of crack-resistant constructional ceramics on the basis of nonoxygen compounds have been used modified powders of these compounds during milling with an additive of silicon alkoxide (tetraethoxysilane). Nucliation and mechanochemical synthesis of β-SiC during milling of powders with this additive can be most brightly presented at obtaining of the modified electrocorundum (Fig. 1). After 1 hour of a grinding in a spherical mill mechanochemical synthesis of β-SiC in the course of milling of the organo-inorganic complex $(–CH_3)–(SiO_2)_n$ has been observed [7].

Use of the powders of refractory compounds modified by silicon alkoxide allows to obtain materials with theoretical density at much lower temperatures of their consolidation (Fig. 2).

Thanks to existence of the organo-inorganic complexes $(–CH_3)–(SiO_2)_n$ created at mechanochemical activation, mechanochemical synthesis of β-SiC nanoparticles from them and creation of β-SiC globules 80–30 nanometers in size reinforcing ceramic matrixes from modified powders of refractory compounds such as Al_2O_3, α-SiC, and B_4C, lead to increase of durability and crack resistance of these materials.

During consolidation of the modified by silicon alkoxide powders self-reinforcing of matrixes of materials by β-SiC nanoparticles, creation –intra and –inter nanostructures have been observed.

The peculiarity of structures of the materials consolidated at hot pressing from the modified powders is not only self-reinforcing of ceramic matrixes by nanoparticles that leads to their dispersion hardening, but also loss of silicate layers between grains of the modified filler (Fig. 3).

Properties of hot-pressed ceramics from the modified powders of nonoxygen compounds have been presented in Table 1.

Apparently from Table 1, figures of properties of hot-pressed materials from the powder of SiC modified by silicon alkoxide surpass values of figures of density, porosity, durability, and it provides higher rates of crack resistance and hardness at identical value of friction coefficient at comparing of properties of the consolidated materials with the usual powder of SiC.

Research of processes of hot pressing with a direct transmission of the high-ampere current of nanopowder mixes of partially stabilized zirconium dioxide ZrO_2 – 3 %Y_2O_3 and tungsten monocarbide WC have showed that the optimum modes, providing the maximum density and mechanical properties of the

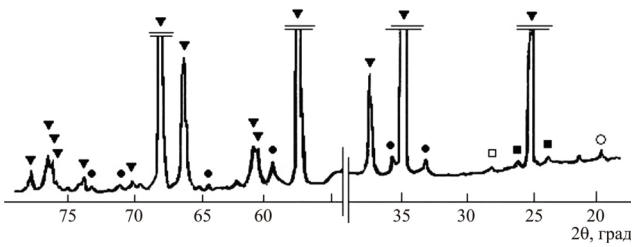

Fig. 1. Phase composition of modified fused corundum after one hour of milling: ▼ – α-Al_2O_3, ● – β-SiC, ○ – Si_2ON_2, ■ – mullite, □ – Si.

material, are: $T_{sintering}$ = 1300 – 1400 °C, $P_{pressing}$ = 30 MPa, $t_{sintering}$ = 2 min. Researches of a microstructure of the received composites ZrO_2–Y_2O_3–WC with the content in initial mixes of 10 wt. % and 20 wt. % WC that have been carried out by means of raster electronic microscopy, have showed a difference of initial mixes as well as the received materials.

As it has been shown at Fig. 3, agglomerates of tungsten monocarbide with an average size of grains are distributed in "cloud" of the white phase ZrO_2–3 wt.

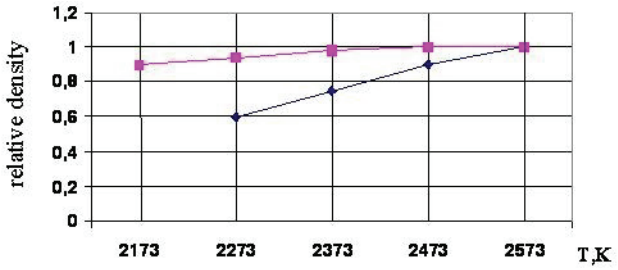

Fig. 2. Dependence of density of hot-pressed samples from usual (•) and modified powder (■) of silicon carbide.

% Y_2O_3. At this it is noticeable that in the agglomerated parts of WC there is the certain hitch similar to links in a chain which in turn chaotically coil. The microstructure of the material received as a result of hot pressing with a direct transmission of the high-ampere current at a temperature of 1350 °C has been shown in

Fig. 3. Destruction surface of hot-pressed (1850 °C, 30 min.) SiC material from the α-SiC powder modified by silicon alkoxide 1 – globules of β-SiC nanoparticles, 2 – grains of α-SiC.

Fig. 4.

From Fig. 4 it is possible to notice that grains of tungsten carbide are in the bulk located in the form of the smallest colonies of nanograins, however there are large agglomerates of tungsten monocarbide in which there are also grains of zirconium dioxide. It is demonstrably visible on the X-ray spectral analysis in point 1.

Results of properties' research of the known consolidated $(Zr_{0.94}Y_{0.06})O_{1.88}$ and developed hot-pressed ZrO_2 – Y_2O_3 – 10 wt. % WC ceramics are reported in Table 2.

From comparison of characteristics of materials from partially stabilized zirconium dioxide and the developed composite on the basis of zirconium dioxide with an additive of 10 wt. % WC it is visible that indicators of physicomechanical properties considerably increase with introduction of nanodimensional tungsten monocarbide.

Research of the influence of tungsten monocarbide nanopowders on properties of zirconium dioxide partially stabilized by yttrium oxide is currently important because tungsten monocarbide has high hardness and abrasive firmness therefore in principle introduction of these additives allows to increase wear resistance and crack

Table 1

Properties of CM from powder of silicon carbide

Properties of material	Self-bonded SiC	Hot-pressed from the modified SiC powder	Hot-pressed from the usual SiC powder
Density [g/cm^3]	3,0	3,3	2,92–3,03
Porosity [%]	2,5	0	2–5
Bending strength [MPa]	220	Not less than 650	Not more than 440
K_{1C} [MPa.m^{0,5}]	2,9–4,1	6,2–6,5	Not more than 4,4
Hardness [GPa]	9,1–9,6	14,7	10–11
Friction coefficient	0,15–0,25	0,16	0,16

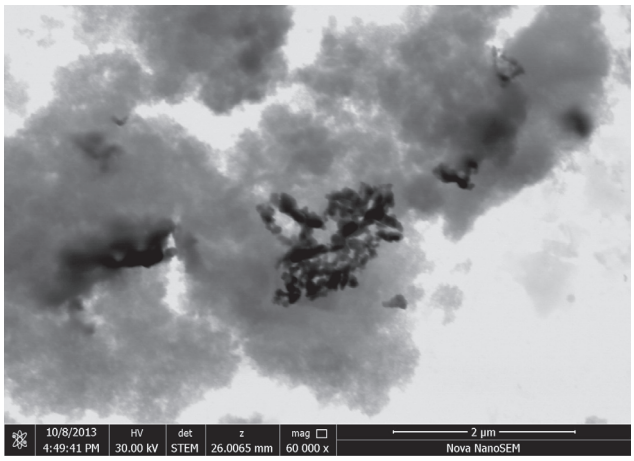

Fig. 4. Initial nanopowder mix of ZrO_2– 3 wt. % Y_2O_3 – 10 wt. % WC.

resistance of a composite as a whole.

It should be noted that tungsten monocarbide carries electric current and consequently the nanopowder mixes can put in positive dynamics into agglomeration mechanisms at hot pressing with a direct transmission of the high-ampere current. At a certain content of tungsten monocarbide in mix there will be the percolation processes, allowing to pass electric current at even rather low temperatures that in turn influences composite structurization, first of all kinetics of growth of grains. On this basis we have investigated processes of hot pressing of mixes with various content of tungsten monocarbide at various temperatures, heating speeds and exposure time, in this case pressure sustaining by graphite compression mould has been maximum.

The realized researches of hardness, durability and crack resistance of composites with various content of tungsten monocarbide give the grounds to assume that the amount of tungsten monocarbide strongly influences the hardness and crack resistance that the greatest hardness turns out at the 30 % content of WC whereas crack resistance turns out maximum at the contents 20 wt. %. Decrease in crack resistance with increase of the content of tungsten monocarbide most likely can be explained by increase in the content of W_2C.

Carbon partially penetrates into a crystal lattice of ZrO_2 that allows to increase durability on phase boundary.

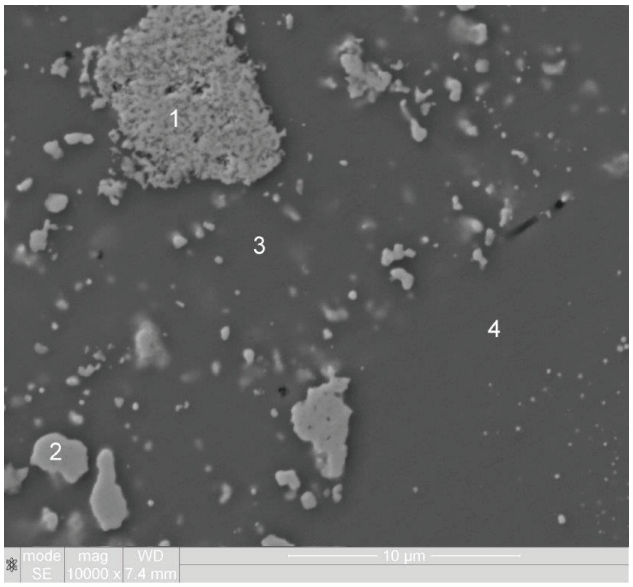

Fig. 5. Microstructure of composite of ZrO_2 – 3 wt. % Y_2O_3 – 10 wt. % WC (sintered at a temperature of T=1350 °C, P=30 MPa and hold time of 2 min.), x 10000. 1 – agglomerates of WC–ZrO_2 – 3 wt. % Y_2O_3; 2 – submicronic grain WC–ZrO_2 – 3 wt. % Y_2O_3; 3 – ZrO_2 – 3 wt. % Y_2O_3 – WC; 4 – ZrO_2 – 3 wt. % Y_2O_3.

Thus the content of W_2C decreases.

As it is shown at Fig. 6, crack extends practically bending around nanograins of tungsten monocarbide, thereby losing energy of destruction that leads to crack resistance increase.

Apparently from fig. 7 sample destruction is transgranular that points at durability on phase boundary. It is most likely explained by partial penetration of carbon from W_2C into a crystal lattice of ZrO_2 increasing durability of interphase borders that in turn increases crack resistance of a composite as well as bending strength.

As can be seen from Figure 9 with increasing hot pressing pressure shrinkage.

It adopts a smoother character.

As can be seen from the composite structure ZrO_2-3 wt.% Y_2O_3-20 wt.% WC. along with nanoparticles have submikronyye WC particles, indicating that the mechanism of nanoparticle growth heterogeneity in hot pressing by

Table 2

Properties of the hot-pressed modified zirconia ceramics

Material composition	Microhardness [HV]	Compressive strength [MPa]	Pycnometric specific gravity [g/cm^3]	Density in reference to theoretical [%]
$(Zr_{0.94}Y_{0.06})O_{1.8}$	1408	2586	6,08	98
$ZrO_2 – Y_2O_3$ – 10 wt. % WC	1650	3200	6,2	99

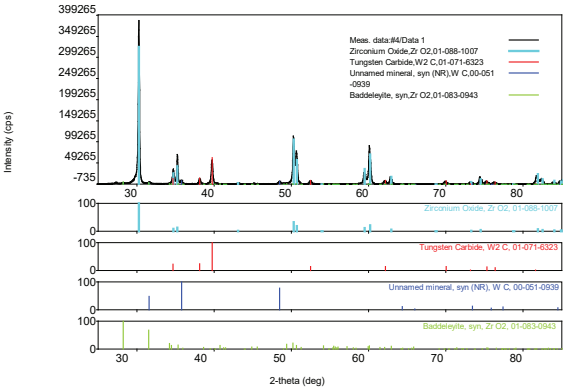

Fig. 6. X-ray spectroscopic analysis of a sample of ZrO2 – 10 wt. % WC received by hot pressing at T = 1400 °C.

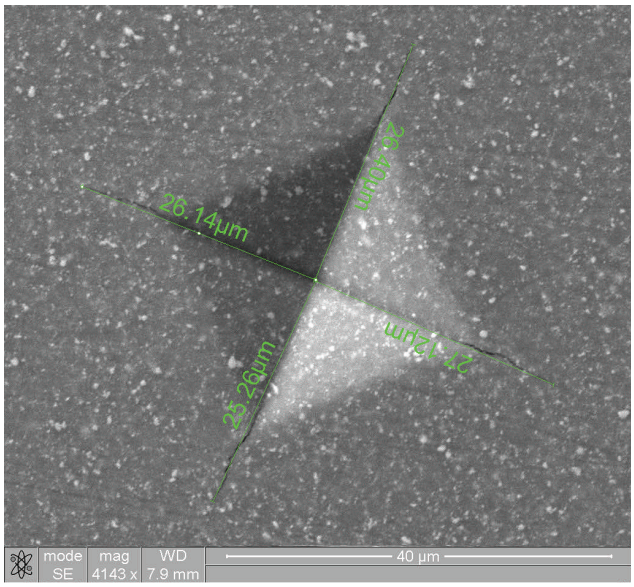

Fig. 7. Formation of cracks in a sample ZrO_2 – 10 wt. % WC received by hot pressing at a temperature T=1200 °C.

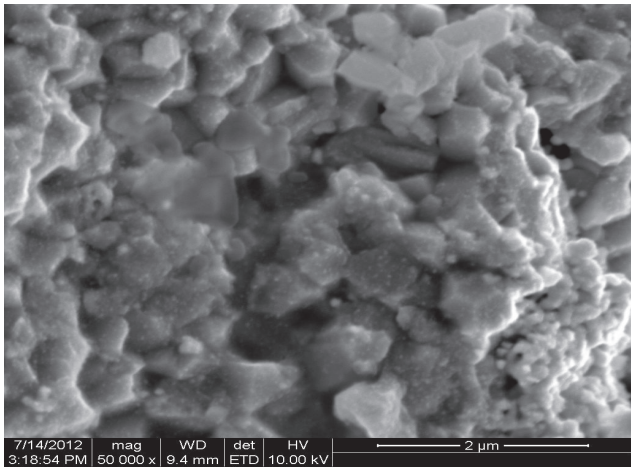

Fig. 8. Fracture of a sample of ZrO_2 – 10 wt. % WC received by hot pressing at temperature T=1200 °C and pressure P=30 MPa.

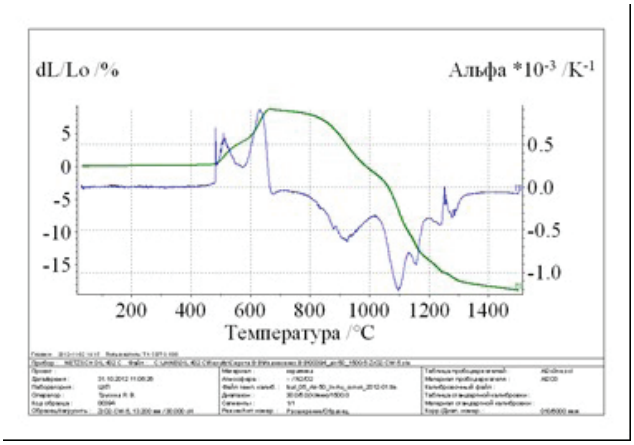

Fig. 9. Curves of composite shrinkage ZrO_2-3 wt.% Y_2O_3-20 wt.% WC shrinkage of the green line at P = 30 MPa, blue at P = 10 MPa.

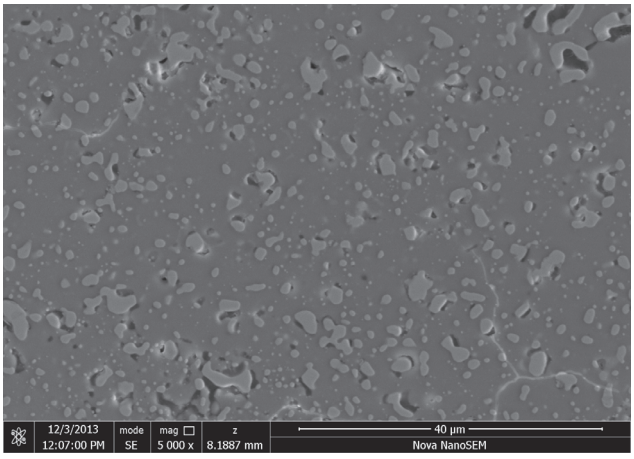

Fig. 10. Composite structure ZrO_2-3 wt.% Y_2O_3-20 wt.% WC, obtained at P = 30 MPa, the temperature T = 1400^0 C, holding time 2 minutes.

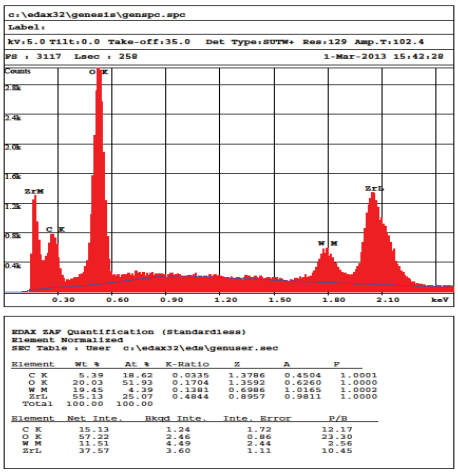

Fig.11. Chemical analysis of the elements of the composite ZrO_2-3 wt.% Y_2O_3-20 wt.% WC, received at P = 30 MPa and temperature T = 1400^0 C, holding time 2 minutes.

passing a high current direct current through the graphite mold (electro consolidation), which is located in a special vacuum chamber. Note the phase boundary between ZrO_2-3 wt.% Y_2O_3-20 wt.% and WC, which shows that the WC grains have a sleek oval surface, which suggests the possible formation of the eutectic at the boundaries between the matrix phase and a reinforcing particles.

On Fig. 10 is represented the chemical analysis of the composite ZrO_2-3 wt. % Y_2O_3-10 wt. % WC, obtained at P = 30 MPa and temperature T = 1400^0 C, holding time of 2 minutes. As can be seen, along with particles of WC, there is a small amount of W_2C, which raises the hardness of the composite, and the fracture toughness lowers.

Conclusion

Thus, mechanochemical synthesis of β-SiC nanoparticles in nanoreactors from the created organo-inorganic complex $(–CH_3)–(SiO_2)_n$ at modifying powders of refractory fillers and carbonaceous binders by silicon alkoxide and gels on its basis has allowed to create CM on the basis of SiC, B_4C, Si_3N_4 with a bending strength not less than 650 MPa and crack resistance 6,5–7,9 MPa.$m^{0,5}$.

The method of hot pressing (1200–1400 °C, the speed of temperature raise 400 degrees/min.) also synthesized the nanomaterial ZrO_2–WC from mix of the nanopowders of WC and ZrO_2 received by thermodecomposition of zirconium salts. Samples from the developed material had bending strength 250–300 MPa, crack resistance 10–15 MPa $m^{0,5}$, hardness 22–24 GPa, heat conductivity 30–35 W/m K.

From the researches carried out follows that additives of nanopowders of tungsten monocarbide to partially stabilized zirconium dioxide lead to microhardness and durability increase that, apparently, is explained by durability increase on the interphase borders and fine-grained structure of the received samples.

References

1. D.Sherman, D.Brandon, Mechanical Properties of hard materials and their relation to microstructure, Advanced Engineering Materials 1 (1999) 161–181.
2. Z.X Yuan, J.Vleugels, Biest O. Van Der, Preparation of Y_2O_3–coated ZrO_2 powder by suspension drying, J. Mater. Scien. Let., 19 (2000) 359–361.
3. Shevchenko V.Y. Technical ceramics / V.Y. Shevchenko, S.M. Barinov. – M.: Nauka, 1993.– 192 p.
4. S.M Barinov, V.Y. Shevchenko, Durability of technical ceramics, Nauka, Moscow, 1996.
5. G.D. Semchenko, I.Y. Shuteyeva, M.A. Kuschenko [and others], Thermodynamic research of possibility of low-temperature synthesis of SiC in system Si–O_2–C, All-Russian conference, Novosibirsk (2009) 187.
6. G.D. Semchenko, Constructional ceramics and refractories, Shtrih, Kharkov, 2000.
7. G.D. Semchenko, I.Y. Shuteyeva, O.N. Borisenko, Corundum coatings for high-temperature protection of graphite against oxidation Raduga, Kharkov, 2011.
8. G.D. Semchenko, Sol-gel process in technology of ceramics BI, Kharkov, 1997.
9. G.D. Semchenko, Checked by fire and time Raduga, Kharkov, 2013.
10. M.O. Azerenkov, E.S. Gevorkyan, S.V. Lytovchenko, V.O. Chyshkala, L.A. Tymofeyeva, O.M. Melnyk, Yu.G. Gutsalenko, Ukraine Patent № 72841 (2012).

Вісник ХНУ, серія «Фізика», вип. 24, 2016. с. 36-40

УДК 539,25; 539,26
PACS: 61.46.-w;
68.75.Lp

The structural and morphological study of the powder sample of strontium hexaferrite

E.M. Savchenko, S.I. Petrushenko, K.A. Mozul

V.N. Karazin Kharkiv National University
61022. Kharkiv, Svobody sq., 4

In the paper the results of X-ray diffraction and electron microscopic examination of the ferrite sample are presented. It is found that the ferrite consists of particles with size of 20-50 nm, with a narrow size distribution. It has been shown that the individual ferrite particles tend to unite in large complexes, with an average size of 600 nm. A complex structure of hexaferrite particles was detected, which consists of a dense core and a light shell.
Keywords: ferrite, X-ray diffraction, powder particle size.

В работе представлены результаты рентгенографического и электронно-микроскопического исследования ферритового образца. Установлено, что феррит состоит из частиц размером 20–50 нм с достаточно узким распределением по размерам. Показано, что отдельные частицы феррита стремятся объединиться в крупные комплексы, средний размер которых составляет 600нм. Обнаружена сложная структура частиц гексаферрита, которые состоят из плотного ядра и более легкой оболочки.
Ключевые слова: феррит, рентгенограмма, размеры частиц порошка.

У роботі представлені результати рентгенографічного та електронно-мікроскопічного дослідження феритового зразка. Встановлено, що ферит складається з частинок розміром 20-50 нм з досить вузьким розподілом за розмірами. Показано, що окремі частинки фериту прагнуть об'єднатися у великі комплекси, середній розмір яких становить 600нм. Виявлена складна структура частинок гексафериту, які складаються з щільного ядра і легшої оболонки.
Ключові слова: ферит, рентгенограма, розміри частинок порошку.

It is well known that modern electronics development is moving towards increasing the density of the elements. This inevitably leads to the necessity of using in electronic devices of components that have increasingly smaller sizes. However, many of their physical properties depend on the size, and may vary with time. The reason for this can be both chemical interaction processes and diffusion processes which are substantially more active in nanoscale samples than in the bulk ones [1]. Thus, the study of the properties of fine materials, as well as using them as technological objects or model samples, is impossible without a thorough study of their morphology.

This work is devoted to the study of the structure of strontium hexaferrite $SrFe_{12}O_{19}$, which is a hard magnetic material and an important component for the manufacture of magnets, which is applied in many fields of technology: from the carriers in recording devices to medical and biological innovations. Due to the wide application, ferrites are investigated in considerable detail. However, to evaluate the influence of particle size on physical properties, particularly, magnetic properties, it is necessary to understand how the morphology of ferrite powders changes with an increase of dispersity and, consequently, with the rise of the contribution of the surface, and also to have samples with reliably defined structural parameters.

It is known that the surface energy of the phase (the phase boundary) is higher in comparison with the volume energy. The energy lowering is due to the surface restructuring because of the migration of atoms or the adsorption of additional components. For example, in the study of single crystal of barium hexaferrite $BaFe_{12}O_{19}$ [2] by X-ray photoelectron spectroscopy it was found the difference between the element composition of the surface and the stoichiometric composition. On the surface there was an excess of oxygen, and positions of iron appeared to be vacancies. Such deformation of the structure leads to the distortion of the magnetic subsystem of ferrite, the depth of which, according to the authors, is less than the crystallographic one. Because of the smallness of this layer it was not detected for a long time, and the near-surface region was considered as "magnetically-dead" (non-magnetic). are obtained [3] Direct evidence of the

existence of the surface region with "chamfered" magnetic structure of finite thickness (from 5-10nm in ferrite base compositions to ~ 200nm in aluminum substituted ferrites) was obtained from the studies [3] of the Mössbauer spectra of ferrite single crystals, that is a consequence of the existence of the surface as a structural defect. The Curie temperature of the open surface layer appears to be a few dozens of degrees (50-75K) lower than that of a bulk crystal.

During the transition from macrocrystals to nanocrystals of $BaFe_{12}O_{19}$ magnetic structure is transformed. The thickness of the plate-ferrite particles having a hexagonal shape becomes comparable with the size of magnetically perturbed area. It is accompanied by a significant decreasing of the magnetization [4.5]. In addition, by the temperature dependence of the specific magnetization, the transition from the magnetically-stable state to the superparamagnetic state in calcium-barium hexaferrite (10-60nm particle size) is detected [6].

Experimental technique

As the samples for the research, the industrial strontium hexaferrite $SrFe_{12}O_{19}$ was used. The study of the phase composition was carried out by X-ray diffraction measures using X-ray diffractometer DRON-2. This is a classical method which makes it possible to carry out a qualitative phase analysis, identification of chemical elements and compounds, studying of preferred orientation in crystals, and grain size evaluation. The morphology of ferrite samples was studied with a scanning electron microscope (SEM) JEOL JSM840 and transmission electron microscope (TEM) 100BR EME.

In additin, the possibility of transition of particles to the superparamagnetic (SPM) state was assessed by calculating the critical superparamagnetic volume of ferrite particles. Experimental research of the magnetic state in a wide temperature range was carried out by the method suggested in [8].

Samples for X-ray studies were prepared by pressing industrial strontium hexaferrite powder in a cylindrical tablet with the radius of about 5 mm and the height of about 3. For the samples examined by transmission electron microscopy (TEM), the structural basis was the carbon film that was condensed under vacuum (10^{-6} mm Hg) to a cleavage of single crystal KCl. Then the salt crystal dissolved in water and the carbon film was transferred to an electron-microscopic mesh. A drop of slurry from the ferrite powder with distilled water was applied to the prepared mesh, and then the sample was dried.

Results and its discussion

Fig. 1 shows the SEM micrograph of the investigated sample of hexaferrite. When X-ray studying the samples, it was found that they really are the single phase strontium

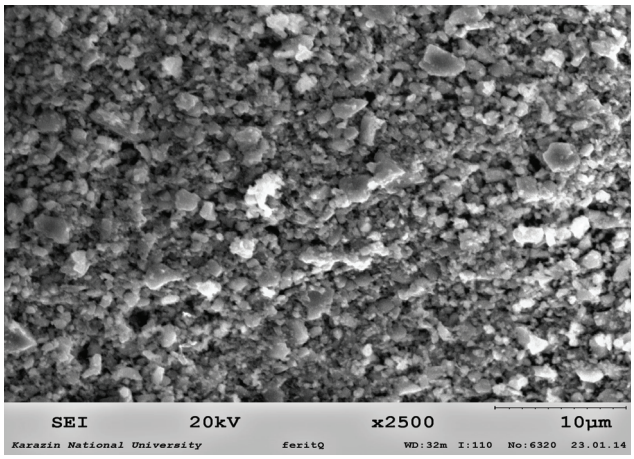

Fig.1. An electron micrograph of the pressed sample of strontium hexaferrite.

hexaferrite. The resulting Debye pattern was shown in Fig. 2. The unit cell has a hexagonal symmetry, characterized by the space group P63/mmc. The calculated lattice parameters for strontium hexaferrite $SrFe_{12}O_{19}$ are: a = 5,883 nm, c = 23,046 nm (reference: a = 5,886 nm, c = 23,037 nm). As a reference, we used data of «1996 JCPDS – International Centre for Diffraction Data. All rights reserved». It should be noted that when comparing the experimental data with the reference x-ray data, a relative change in intensity of lines (107) and (114) was found, which may be caused by the presence of a partial texture of the sample.

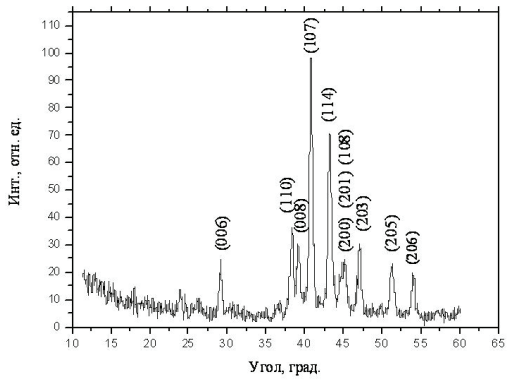

Fig.2. The XRD pattern obtained from the pressed sample of strontium hexaferrite.

The estimation of the mean characteristic size of coherent scattering regions has been made on the basis of the broadening of diffraction lines, using the Selyakov - Scherrer formula

$$D = nd = \frac{\lambda}{\beta \cos\theta} \qquad (1)$$

β is the half-width of the line; λ is the wavelength; θ is the diffraction angle; D is the crystallite size; n is the number of interplanar spacings d_{hkl}

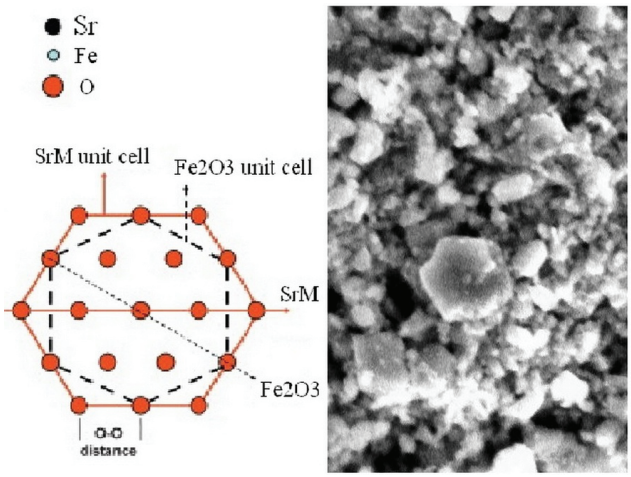

Fig.3. An electron micrograph of the strontium hexaferrite pressed sample (b) and the structure of the basal plane (a).

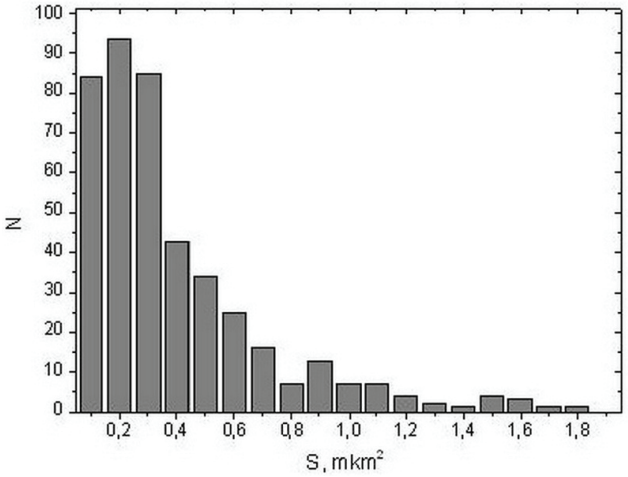

Fig.4. The histogram of size distribution of the ferrite particles.

The obtained value was equal to 20 nm. It can be assumed that the actual grain size significantly differed from this one, because the technology of obtaining powder did not provide the desired formation of nano-sized particles.

To estimate the actual grain size of the powder electron microscopy data were used. SEM image of the sample is shown in Figure 3. In the photo it is clearly visible the particle with hexagonal faceting that is typical for hexagonal symmetry P63/mmc.

Determination of the average typical size of particles observed in the pictures, and the construction of their size distribution were carried out using specially designed software. The resulting distribution is shown in Fig. 4 [9].

The average crystallite area according to research data was S = 0,370 mkm^2, which corresponds to the average typical size D = 600nm. This significant difference between the results of X-ray analysis and SEM suggested that the particles observed in Fig. 1, 3 have composite structure, and the process of pressing samples and relatively low resolution of SEM complicate their fine structure observation, for registration of which the methods of transmission electron microscopy were used.

In the picture (Fig. 5) obtained at low magnification, the general structure of the sample is shown. Ferrite particles come together in fairly large complexes, which are elongated structures having length many times greater than their transverse dimension. Such aggregation of the particles of the ferrite powder is, probably, due to the strong uniaxial magnetocrystalline anisotropy of hexaferrite, which determines the tendency of the particles to unite. The sizes of such composite particles are in the range from

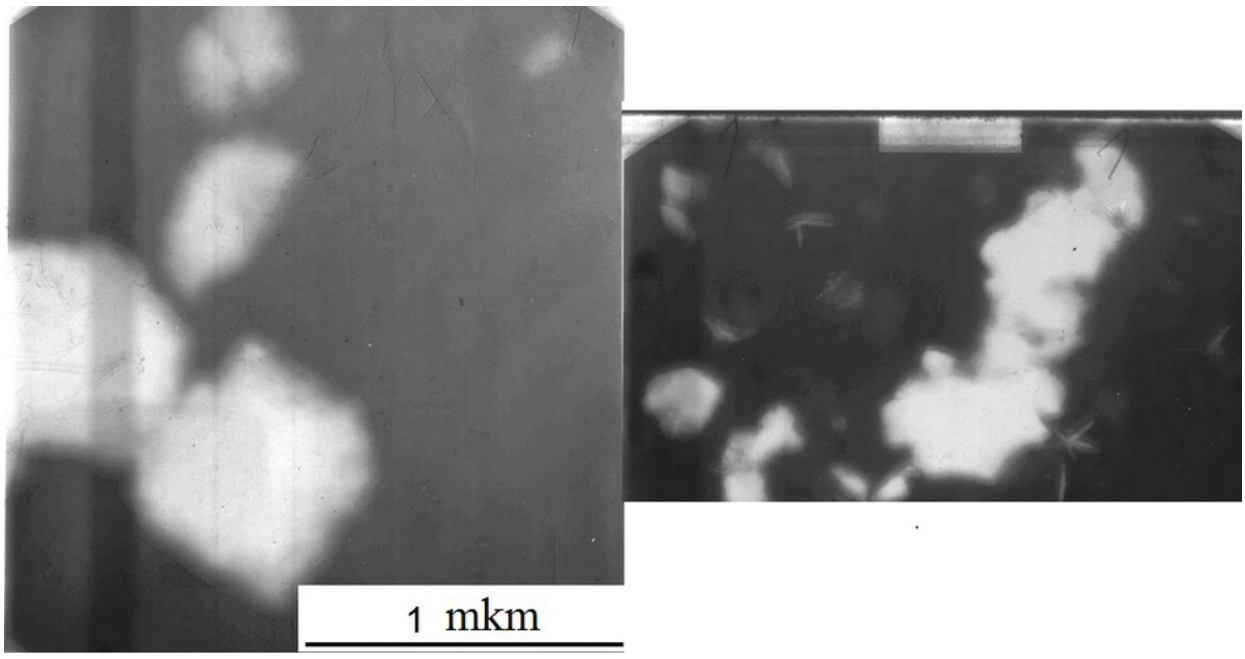

Fig.5. Illustration for composite structure of particles of studied sample.

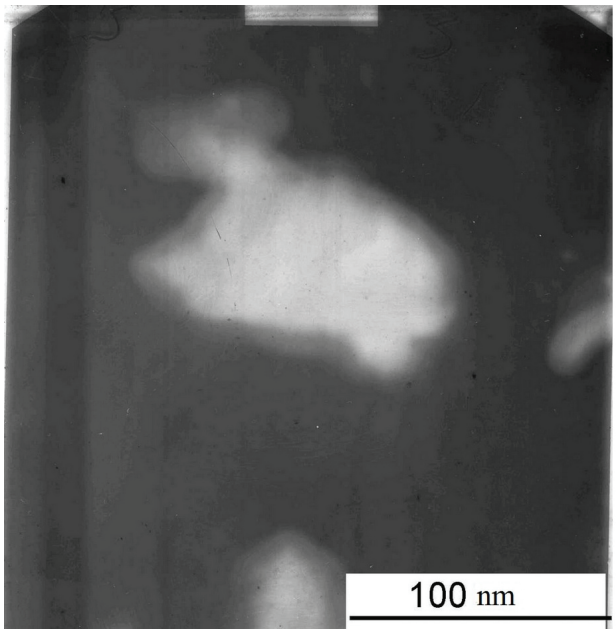

Fig.6. complicated structure of individual particle at high magnification.

about 200 nm to 8000 nm, and in some pictures even larger units are detected. Averaged value of the typical size of such composite particles is about 600 nm and coincides with the results obtained with the use of SEM.

In addition to the large composite particles, complicated structure of which is clearly visible in the fluorescent screen of electron microscope, there are a small number of particles having much smaller size. Besides small size, these particles are characterized by narrow size distribution. Particles of this class have a typical size in the range of 25-50 nm that is comparable to the value obtained during radiographic examinations.

A similar pattern was observed in [7] in the study of nanocomposite WC-Co alloy. Evaluation of grain size on the X-ray data (50nm) basis gave about 1000 times smaller result than the SEM (75mkm). However, these large friable particles were easily crumbled by grinding into smaller nanocrystalline grains, the size of which according the TEM data correlated with X-ray data.

Furthermore, the analysis of electron microscopic images showed that the nano-sized particles of ferrite have a complex structure as well, and consist of fairly dense core surrounded by lighter shell which is more transparent for the electrons (Figure 6). The depth of the shell is about 10

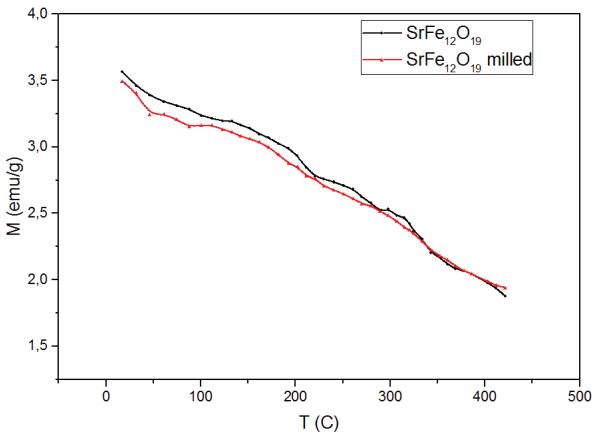

Fig.7. Temperature dependence of magnetization at constant external field H=1 kOe.

nm. This result agrees with the results of [2] which indicate the difference between the surface and the stoichiometric structures. According to the authors, on the surface there exist an excess (compared to stoichiometric) amount of lighter and hence more "transparent" oxygen ions and deficit of relatively heavy iron.

The possibility of transition of the particles of investigated hexaferrite system $SrFe_{12}O_{19}$ into the SPM state is found out by evaluating the critical superparamagnetic volume $V_{so}(H = 0)$ and comparing it with the actual minimum volume V_{min} obtained by microscopy.

The critical volume is determined by equating the magnetic anisotropy energy of the particles and thermal energy [8]:

$$KV_{so} = 25kT \qquad (2)$$

It is evident that with temperature increasing the magnitude of critical volume rise substantially, and thus the probability of the transition of particles in to the SPM state grows.

As can be seen in the curves of σ (T) (Fig. 7) taken at a fixed magnetic field H = 1 kOe, the anomaly predicted by Pfeiffer [4] is not observed. This indicates that actual particles volume is above the critical superparamagnetic one all over the temperature range up to the Curie temperature. It can be assumed that a slight part of the powder with small particle sizes, which was detected in micrographs, goes into SPM state. However, in view of the small pro rata contribution of this group of particles, the anomaly in

Table 1.

The dependence of the magnetocrystalline anisotropy constant and the critical volume of the particles on temperature

T	$K_1 *10^{-6}$, ergs / cm^3	$K_1(T)/K_1(300)$	$V_{S0} *10^{-21}$, cm^3	d_S, nm
300	3.3	1	279	11.2
400	2.7	0.818	455	13.2
500	2.04	0.618	752	15.7
600	1.23	0.373	1501	19.7
700	0.24	0.073	8944	35.7

the temperature dependence of the magnetization does not occur.

Conclusions

In this paper it is founded that the ferrite used for radiographic studies, has a hexagonal structure. Redistribution of intensities of the diffraction lines indicates the texturing of the sample, which is confirmed by TEM studies. By SEM research it is revealed that the morphology of the molded ferrite samples is represented by a number of large particles having a typical size of about 600 nm. It was found that the ensemble preserves magnetically stable condition over the entire temperature range, up to the Curie point, despite the presence of the fraction of particles whose dimensions match the SPM transition condition, which generally correlates with the results of microscopic research. At the same time, TEM studies have shown that these particles have a complicated structure and are composed of separate units, distributed in a narrow range of sizes, and their average size is about 45 nm and generally correlates with the diffraction analysis results. Furthermore, a complex structure of separate ferrite particles is determined. It was first found by TEM that the particles consist of a massive core surrounded by a lighter shell.

References

1. I.G. Churilov S.V. Dukarov, S.I. Petrushenko, V.N. Sukhov Effect of temperature on the pores growth in the polycrystalline films of fusible metals Probl. At. Sci. Tech V.10 N. 110 2014
2. Kamzin A.S., Rozenbaum V.L., Ol`khovik L.P., Kovtun E.D.Diagnostics of the surface and near-surface region of barium hexaferrite monocristals// J.Magn.Magn.Mater.- 1996.- V.161.- P.139-142.
3. Камзин А.С.,Ольховик Л.П., Розенбаум В.Л.Одновременная гамма-, рентгеновская и электронная мессбауэровская спектроскопия магнитной структуры поверхности и объема гексагональных ферритов типа М//ЖЭТФ.-1997.-Т.111,№4.-С.1426-1437.
4. Голубенко.З.В., Ольховик Л.П., Сизова З.И. Особенности поведения намагниченности системы нанокристаллов высокоанизотропного гексаферрита// Вісник ХДУ. Сер.«Фізика».-1988.-№417,вип.1.- С.54-57.
5. Ольховик Л.П., Пушкарская А.А., Ткаченко Н.В., Барабашко М.С. Физико-технологические принципы создания биосовместимых суперпарамагнитных частиц медико-биологического назначения// Вістник ХНУ. Сер.«Фізика».- 2009.- №865,вип.12.- С.58-61.
6. Мозуль К.А., Ольховик Л.П., Сизова З.И., Шуринова Е.В. О влиянии внешнего магнитного поля на формирование магнитного состояния наночастиц $Ca_{0.5}Ba_{0.5}Fe_{12}O_{19}$ // Вістник ХНУ. Сер.«Фізика».- 2010.- №915,вип.14.- С.96-98.
7. Seegopaul P., McCandlish L.E., Shinneman F.M.// Production capability and powder processing methods for nanostructured WC-Co powder.//Intern.J.Refr.Met.and Hard Mater. 1997.V.15.- №1-3.-P.133-138.
8. Pfeiffer H., Schüppel W. Temperature dependence of the magnetization in fine particle systems and the Hopkinson effect. Application to barium ferrite powders // J. Magn. Magn. Mater. – 1994. – Vol. 30. – p. 92 – 98.
9. Е.М. Савченко, Д.С. Урденко Сравнительный анализ методик определения размеров частиц порошкового образца для учебного эксперимента. //Проблеми сучасної освіти: збірник науково-методичних праць.- Вип.5. У 2ч.: Ч.1.- Х.: ХНУ імені В.Н.Каразіна, 2014, С. 99-102.

Вісник ХНУ, серія «Фізика», вип. 24, 2016. с. 41-44

UDC: 546.284-31-022.532+539.1.074.3
PACS: 81.07.Bc,78.55.-m

Nano-porous SiO_2-matrices for development of new optical materials

Ju. I. Boyko[1], Yu. V. Malyukin[2], I.I. Bespalova[2], L.I. Voloshina [2], O. G. Vyagin[2], V.V. Seminko [2], V. F. Korshak[1], I. V. Postavnychyi[1]

[1]V. N. Karazin Kharkiv National University,
4 Svobody Sq., 61077, Kharkov, Ukraine
[2]Institute for Scintillation Materials, National Academy of Sciences of Ukraine
61001 Nauki aven., Kharkiv, Ukraine
ganina@isma.kharkov.ua

Nano-porous transparent SiO_2-matrices obtained by sol-gel techniques and organic phosphors PPO, o-POPOP, p-Tp are produced, and their optical, luminescent, and scintillation characteristics are studied. It is shown that these simples generate an intense photoluminescence signal, possess a nanosecond decay time. The absolute light yield of the composites was determined to be 4400 photon/MeV for SiO_2:PPO, 5100 photon/MeV for SiO_2:o-POPOP, and 1800 photon/MeV for SiO_2:pTh.

Keywords: SiO_2-matrice, organic phosphors, scintillation characteristics.

Описан метод получения нанопористых прозрачных SiO_2-матриц, содержащих органические фосфоры PPO, o-POPOP, p-Tp, изучены их оптические, люминесцентные и сцинтилляционные характеристики. Показано, что такие материалы имеют интенсивный сигнал фотолюминесценции и обладают наносекундными временами затухания. Величина абсолютного световыхода при возбуждении альфа-излучением с энергией 5.46MeV составила 1800−5100 фотон/MeV, амплитудное разрешение лежит в диапазоне 27−67%.

Ключевые слова: SiO_2-матрица, органические фосфоры, сцинтилляционные характеристики.

Описано метод отримання нанопористих прозорих SiO_2-матриць, які містять органічні фосфори PPO, o-POPOP, p-Tp, досліджено їх оптичні, люмінесцентні і сцинтиляційні характеристики. Показано, що такі матеріали мають інтенсивний сигнал фотолюмінесценції і володіють наносекундним часом загасання. Величина абсолютного світловиходу при збудженні альфа-випромінюванням з енергією 5.46MeV складає 1800-5100 фотон/MeV, амплітудне розширення лежить у діапазоні 27-67%.

Ключові слова: SiO_2-матриця, органічні фосфори, сцинтиляційні характеристики.

Nowadays, highly porous materials obtained by different techniques have attracted a lot of attention as materials for the development of new nanoscale objects with unusual and unique properties [1, 2]. There are a number of properties such as the strict ordering of pores at large surface areas, the narrow dispersion of pore diameters and intervals between them, the controlled pore diameter allowing to create new materials based on the nanosized matrices.

Different polymers, silica-gels, xerogels, ormosils and composite glasses were used as matrices, and are of great potential for technical application in the fields of optics, electronics, mechanics and environment protection [2].

Nano-porous silica matrices are unique materials with high specific surface area, high porosity (order 50-75%) and low index of refraction [3, 4]. The sol-gel technique is the primary method used to prepare nano-porous SiO_2-matrices. For the synthesis of materials by a sol-gel technique organic metal compounds are usually used such as metal alkoxides $[M(OR)_n]$, where M represents a network forming element (Al, Si, Ti, Zr, etc.), and R is usually an alkyl group [2, 5]. The hydrolysis and polycondensation of the metal alkoxide precursor lead to the transition from a colloidal solution to a solid phase. The characteristics of the materials synthesized via the sol-gel technique are influenced by many parameters, such as the nature of the reagents, the molar ratios used, the type of solvents and catalysts, the reaction temperature and the rate of removal of solvents. In particular, the choice of catalyst influences the properties of the material. Hydrolysis is favored by acidic catalysis and, therefore, in such conditions the formation of linear Si-O-Si polymers is favored. This causes the formation of more compact material (with small pores) compared with that obtained using basic catalysis [2, 6].

Due of their unique properties, SiO_2-matrices have been extensively studied as inter-metal dielectric materials,

for optical and acoustic applications [1, 2]. The introduction of various organic phosphors into nano-porous SiO_2-matrices makes possible to produce composite luminescent materials with required properties. Such SiO_2-matrices can be used as fluorescent screens or scintillator materials [1, 7, 8].

In this work, we report our experimental results on the structural properties of pure nano-porous SiO_2-matrices and optical properties of SiO_2-matrices doped by organic phosphors. As organic phosphors 2,5-diphenyloxazole (PPO), 1,2-bis(5-phenyloxazolyl-2)benzene (o-POPOP) and 1,4-diphenyl benzene (p-Tp) were used.

Experimental techniques

Optical transmission spectra were measured using a SPECORD 200 spectrophotometer (Analytik Jena, Germany). Luminescence spectra were recorded using an automated spectrofluorimeter based on a grating monochromator. Luminescence was excited by the radiation of a He-Cd laser with a wavelength of 325 nm. Luminescence decay curves were measured using a FluoTime 200 picosecond spectrofluorimeter (PicoQuant, Germany) with a semiconductor laser with a wavelength of 330 nm as the excitation source and a setup instrument function of 0.5 ns.

Pulse amplitude spectra were measured using a spectrometric circuit consisted of a BUS2-94 preamplifier, a BUI-3K spectrometric amplifier, and an AMA-03-F multichannel amplitude analyzer (Tenzor Co., Russia). An R1307 photoelectric multiplier (Hamamatsu Co., Japan) was used as the photodetector; scintillations were excited by α particles with energy of 5.46 MeV emitted from a 238Pu radioactive source.

Synthesis and characterization

The method of obtaining of SiO_2-matrices is based on the widely known sol-gel method, which proceeds through the steps of hydrolysis and polycondensation of organic silicon compounds in an alcohol solution containing acid or base catalyst.

Briefly, tetramethoxysilane ($Si(OCH_3)_4$, 98,0% "Merck" (Germany), TMOS), anhydrous methanol and water with volume ratios of 1:0,84:1,2 were used as precursors for the silica and nitric acid (HNO_3, 65%) used as a catalyst. All components were mixed for about 5 min until the transparency appear. The mixture was poured in plastic Petri dishes (D=35 mm) and held for 24 h at room temperature until a gel was formed, which was then dried in the oven at 45°C for several days. The heat-treatment was executed at increasing temperature up to 500°C for 10 h and held for 2 h. The samples of SiO_2-matrices were transparent colorless disks with D = 20 mm and H = 1 mm (Fig.1.).

The organic phosphors were introduced by impregnating the SiO_2-matrices into the compositions of the solutions PPO, o-POPOP and p-Tp in toluene with optimal concentrations of 1,0 wt % [9]. SiO_2-matrices were held in these solutions for 5-48 h and then dried at 50°C until constant weight. It has been found experimentally that the samples of SiO_2-matrices with a concentrations of the dopant of 1-10 wt % possess the most intensive luminescence.

Fig. 1. Photographic of SiO_2-matrices.

According to X-ray phase analysis SiO_2-matrices have an amorphous structure. Studying the surface of the matrices by AFM revealed open pores with the diameters about 20 nm. TEM images of the samples reveal that matrices consist of silica nanoparticles with average sizes of about 30 nm. Pore distribution, and specific surface areas were calculated from the nitrogen adsorption isotherms, via the BET method. The specific surface area of the samples of SiO_2-matrices is 800 m^2/g with corresponding total pore volume of 0,55 cm^3/g. The density and porosity of the matrices determined using the hydrostatic weighing method [8] are 1.40 g/cm^3 and 54 vol %, respectively. The average microhardness of the matrices is 170 kg/mm^2, which is practically twice as high as the values reported by the other authors [1, 10].

Optical properties

Luminescence and scintillation properties of obtained materials were investigated. In Fig. 2 the absorption and luminescence spectra of SiO_2-matrice with incorporated PPO, o-POPOP and p-Tp organic phosphors are shown. Both the edge of fundamental absorption and maxima of luminescence of organic phosphors in the matrix are shifted (~40 nm) to long-wavelength region as compared with the spectra of corresponding solutions indicating a strong interaction of phosphor molecules with pores of SiO_2-matrices.

Incorporation of organic phosphors into SiO_2-matrices leads not only to strong interaction between phosphor molecules and pores of SiO_2-matrices, but also to increase of interaction between molecules themselves that can be

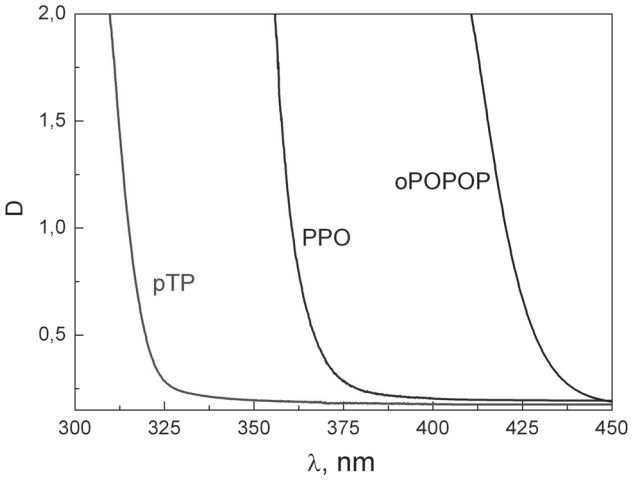

a

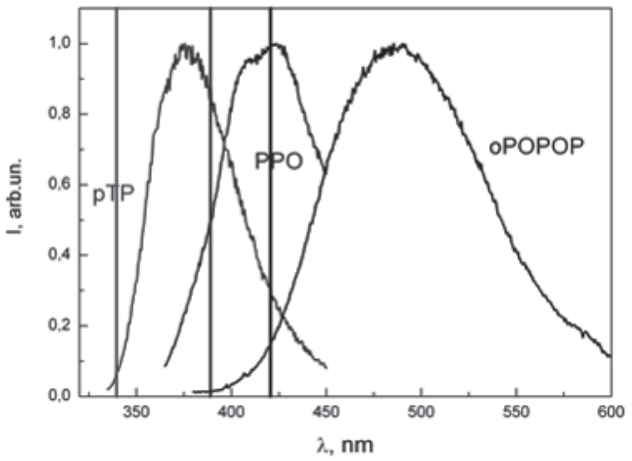

b

Fig.2. Absorption spectra of SiO_2-matrices with different phosphors (a). Luminescence spectra of SiO_2-matrices with different phosphors (b).

seen from the modification of kinetics of excitation energy relaxation. Decay curves of PPO in solution and in the SiO_2-matrice at different concentrations of phosphor molecules are shown in Fig. 3 (λ_{exc}= 377 nm). Decay curves of phosphors are sufficiently modified with their incorporation into SiO_2-matrices. At the initial stage of luminescence decay (0-15 ns) shortening of decay time is observed, most likely due to luminescence quenching due to decrease of the distance between PPO molecules. Meanwhile, in the range of 15-50 ns, the second component is observed, which may be determined by migration of excitation energy between the phosphor molecules.

In the Fig.4 the pulse height spectra of SiO_2-matrices with different phosphors under excitation by alpha-radiation are shown. It can be seen that spectra are symmetric and well fitted by Gaussian function that indicate the uniform distribution of the dopant molecules within the matrix volume. The pulse height resolution R is 27% for SiO_2:PPO, 32 % for SiO_2:o-POPOP and 67% for p-Tp. The absolute light yiel d of the composites was determined to be 4400 photon/MeV for SiO_2:PPO, 5100 photon/MeV for SiO_2:o-POPOP, and 1800 photon/MeV for SiO_2:p-Tp. These values of light yield are rather low, but comparable to the light yield of. the BC416 commercial plastic scintillator based on polyvinyl toluene (Saint Gobain Co.), equal to 6000–7000 photon/MeV.

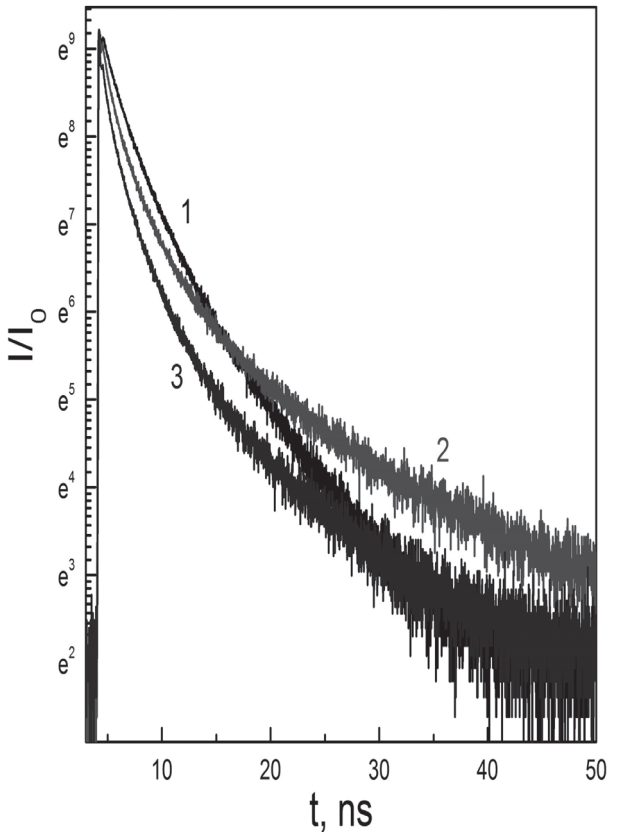

Fig. 3. Decay curves of PPO luminescence (λ_{exc}= 377 nm). 1 – in solution, 1 mass.%; 2 – in SiO_2-matrice, 1 mass.%;3 – in SiO_2-matrice, 10 mass.%.

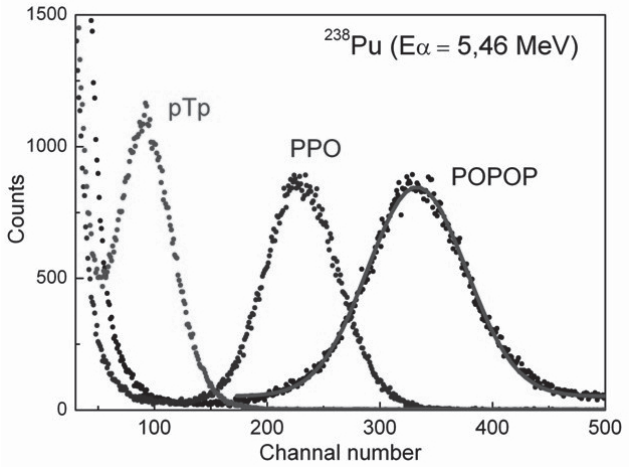

Fig. 4. Pulse height spectra of SiO_2-matrices with different phosphors under α-excitation (excitation source - ^{238}Pu).

Conclusions

Highly-porous transparent SiO_2-matrices obtained by sol-gel techniques are perspective materials for creation of

new luminescence and scintillation materials on their base. These matrices have high porosity (54 vol. %) with average pore diameter equal to 10 nm. Impregnation of SiO_2-matrices by phosphor molecules (such as PPO, o-POPOP, p-Tp) allows to obtaining luminescent and scintillation materials with properties quite different from those observed in corresponding phosphor solutions. Obtained materials have moderate scintillation properties; however their light yield is comparable with the one of commercial plastic scintillators.

References

1. Liu P.S., Chen G.F. Porous Materials: Processing and Applications, Butterworth-Heinemann, Elsever (2014), 576 p.
2. Optical and Electron Phenomena in Sol-Gel Glasses and Modern Application, Structure and Bonding/R. Reisfeld, C.K. Jorgensen (Eds.) – Springer, 1996. – 251 pp.
3. H. Zhang, Y. Qiao, X. Zhang, S. Fang. J. Non-Cryst. Solids, 356, 879–883 (2010).
4. E. A. Tikhonov, A. K. Lyamets, I. I. Bespalova, Yu.V. Malyukin, http://arxiv.org/abs/1504.04262 04/2015.
5. M. Catauro, R.A. Renella, F. Papale, S. V. Ciprioti. Mater. Sci. Eng. C, 61, 51-55 (2016).
6. M.D. Curran, A.E. Stiegman, J. Non-Cryst. Solids, 249, 62–68(1999).
7. M. Nikl, N. Solovieva, K. Apperson, D. Birch, and A. Voloshinovskii, Appl. Phys. Lett. 86, 101914 (2005).
8. S. Shionoya, W. H. Yen, and H. Yamamoto, Phosphor Handbook, 2nd ed. (CRC Press, Boca Raton, 2006), Pt. III, Chap. 7, p. 637.
9. O. G. Vyagin, I. I. Bespalova, A. A. Masalov, O. V. Zelenskaya, V. A. Tarasov, and Yu. V. Malyukin. Tech. Phys. Lett., 40, 2014.
10. K. S. Lam, X.-L. Zhu, and D. Lo, Appl. Phys. B, 68, 1151 (1999).

Вісник ХНУ, серія «Фізика», вип. 24, 2016. с. 45-49

PACS: 42.70.Gi, 78.20.-e, 42.65.Pc
УДК 535.44, 539.216.2

Optical bistability in the formation of spontaneous gratings in photosensitive AgCl–Ag waveguide films

V. I. Lymar, E. D. Makovetsky

V. N. Karazin Kharkiv National University,
Physical department, Physical optics chair,
ph. (057)707-51-25, e-mail: lymar@univer.kharkov.ua

An experiment was conducted to create periodic structures in light-sensitive waveguide AgCl–Ag films on glass surface under irradiation by He-Ne laser beam (λ = 632.8 nm). So-called spontaneous gratings were formed from Ag granules within AgCl film on the interference pattern created by the beam and scattered waveguide modes. These gratings developed due to positive feedback: diffraction efficiency of spontaneous grating and intensity of waveguide mode are mutually amplified for account of the beam energy. Doubling of the spontaneous grating diffraction reflex has been found, and optical bistability has been shown to occur based on spatial analogy to stimulated temporal oscillations of a harmonic oscillator.

Keywords: light-sensitive materials, waveguide film, AgCl, Ag, waveguide mode, periodic structure, optical bistability.

Проведений експеримент з формування періодичних структур у світлочутливих хвилеводних плівках AgCl–Ag на поверхні скла при опромінюванні пучком He-Ne лазера (λ = 632,8 нм). На інтерференційному полі пучка та розсіяних хвилеводних мод формувались т. зв. спонтанні гратки з гранул Ag у плівці AgCl, що розвивались за рахунок позитивного зворотного зв'язку: взаємного підсилення дифракційної ефективності спонтанної гратки та інтенсивності хвилеводної моди за рахунок енергії пучка. Виявлене подвоєння дифракційного рефлексу від спонтанних граток, та на підставі просторової аналогії з часовими коливаннями гармонічного осцилятора показано, що має місце оптична бістабільність.

Ключові слова: світлочутливі матеріали, хвилеводна плівка, AgCl, Ag, хвилеводна мода, періодична структура, оптична бістабільність.

Проведен эксперимент по формированию периодических структур в светочувствительных волноводных пленках AgCl–Ag на поверхности стекла при облучении пучком He-Ne лазера (λ = 632,8 нм). На интерференционном поле пучка и рассеянных волноводных мод формировались т. наз. спонтанные решетки из гранул Ag в пленке AgCl, развивавшиеся за счет положительной обратной связи: взаимного усиления дифракционной эффективности спонтанной решетки и интенсивности волноводной моды за счет энергии пучка. Обнаружено раздвоение дифракционного рефлекса от спонтанных решеток, и на основании пространственной аналогии с временными вынужденными колебаниями гармонического осциллятора показано, что имеет место оптическая бистабильность.

Ключевые слова: светочувствительные материалы, волноводная пленка, AgCl, Ag, волноводная мода, периодическая структура, оптическая бистабильность.

Introduction

The effects of optical bistability and multistability are of permanent interest when studying nonlinear optical systems [1]. Due to significant concentration of wave energy in a small region of space when light propagation is limited by the interior of the waveguide, nonlinear effects may have a significant impact on propagation of waveguide modes [2]. It has long been known that thin silver halide films with excess of silver are photosensitive. AgCl–Ag films, which are objects of study in this work, are among them [3]. Characteristic feature of photosensitivity of composite AgCl–Ag films is transfer of silver granules to the darker areas of the interference pattern, provided silver layer is thin (about 10 nm) and therefore granular. The pattern is created either by two acting beams or by single beam interference with scattered waveguide modes. Transfer of substance is the cause of proportionality of changes not to intensity I but to energy $H = It$ where t is duration of irradiation. Therefore, researchers' attention is mainly focused on the issue of film changes dependence on H and other exposure conditions.

In this paper we reveal existence of bistability in dependence of waveguide mode intensities in AgCl–Ag films on intensity of the irradiating laser beam, not on value of exposition H.

Experiment

Waveguide silver chloride films with addition of Ag were used in the experiments. AgCl film with thickness ≈ 80 nm and Ag film (≈ 10 nm) were deposited sequentially in vacuum system at a pressure of ~ 10^{-5} mm Hg on a glass substrate. AgCl film thickness was controlled by mass of the thermally vaporized substance (30 mg), and Ag thickness was controlled by frequency change of the quartz thickness meter ($\Delta\nu$ = 15 Hz). The thickness of the resulting AgCl–Ag sample was measured using lines of equal chromatic order and was 92±2 nm.

After deposition, the sample was irradiated by 'white' light of an incandescent lamp to provide more uniform distribution of silver within the matrix of AgCl. Such a distribution of silver (in the form of granules) is indicated by an absorption band in the spectrum of the optical density. The band is associated with irradiation-induced plasma oscillations of free electrons in nanometer-sized silver granules. There is a resonance behavior of these oscillations when the frequency of light matches eigenfrequency of plasma oscillations of free electrons in the granules surrounded by silver chloride. This resonance has a maximum at $\lambda \approx 500$ nm.

The layout of the recording of spontaneous gratings (SG) is shown in Fig.1a. The photosensitive waveguide AgCl–Ag film is irradiated with a normally incident beam of He-Ne laser. Due to the interference of the incident wave with scattered waveguide modes in the film, an interference pattern emerges, and Ag granules move from maxima to minima of the interference. Prior to irradiation, silver granules are statistically uniformly distributed on the surface and inside the AgCl film. During SG recording under the laser irradiation, silver is redistributed to form a periodic structure which is a diffraction grating. Experimental evidence of SG formation are microphotographs, see [3.4].

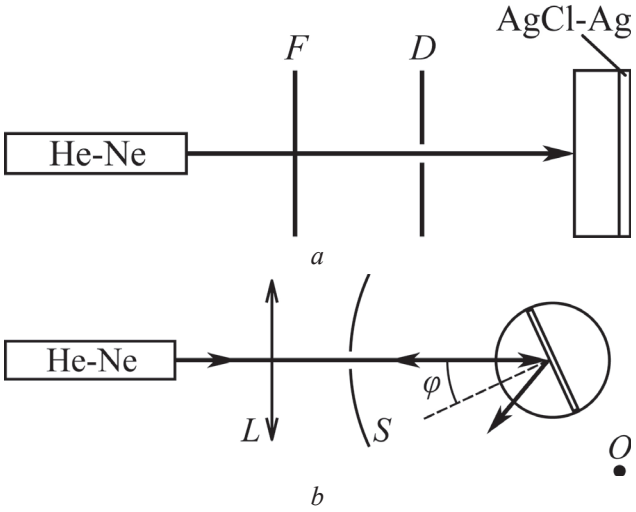

Fig.1. a) Experimental layout used to record spontaneous gratings (SG) in photosensitive waveguide AgCl–Ag films on a glass substrates using a He-Ne laser, light filter *F* and aperture *D*. b) Scheme for observation and measurements of SG periods using autocollimation diffraction after fixing film, top view. *L* is a lens to focus the beam on the sample mounted on a horizontal goniometer. *S* is a screen on which the diffraction pattern was observed in reflected light. *O* is the observation point from which the screen was photographed, see photographs in Fig.2.

After completion of grating recording, the sample was washed by photographic fixer to remove AgCl in order to eliminate photosensitivity. Silver granules remain on the surface of glass substrate and form the gratings which create diffraction reflections observable in autocollimation diffraction scheme (a diffracted beam propagates oppositely to the incident one). To increase brightness of the diffraction pattern, highly reflective aluminum layer was deposited onto the post-fixed sample. The test beam of He-Ne laser was focused at the center (or elsewhere) of the spot with the gratings recorded. Diffraction reflection from SG located within the particular area was observed on the screen installed across the laser beam with an aperture letting the beam through, see Fig.1b. According to the measured value of the rotation angle φ of the sample on goniometer under autocollimation conditions, SG period d was determined by formula $d = \lambda / 2\sin\varphi$ where λ = 632.8 nm is the wavelength of He-Ne laser beam which was used both to record SG and to observe diffraction patterns.

Experimental results

Both SG recording process according to the scheme in Fig.1a and observation of diffraction from SG according to the scheme Fig.1b are convenient to describe in terms of wave vectors. It is known that interference of two coherent waves with wave vectors $\mathbf{k}_1$ and $\mathbf{k}_2$ creates an interference pattern with vector $\mathbf{K} = \mathbf{k}_1 - \mathbf{k}_2$ in the overlapping area. On the other hand, $|\mathbf{K}| = 2\pi/d$ where d is the spatial period of the interference pattern, and direction of the vector **K** is perpendicular to the stripes of interference.

In the case of SG there is interference of the incident wave with wave vector **k** and waveguide modes with wave vector **β**. Since the AgCl–Ag waveguide is thin (less than 100 nm), only projection of the wave vector **k** to the plane of the film is important when creating the interference pattern. Assuming x axis is the crossing of the plane of incidence and the plane of the film, we get an interference pattern vector **K** as

$$\vec{K} = \pm\left(\vec{\beta} - \vec{k}_x\right). \qquad (1)$$

The vector **β** belongs to the layer plane, its value is determined by the dispersion equation for the propagation constant of the waveguide mode in a planar waveguide [5], $k_x = (2\pi/\lambda)\sin\alpha$ where α is the angle of incidence of the laser beam on the film. In the case of normal incidence

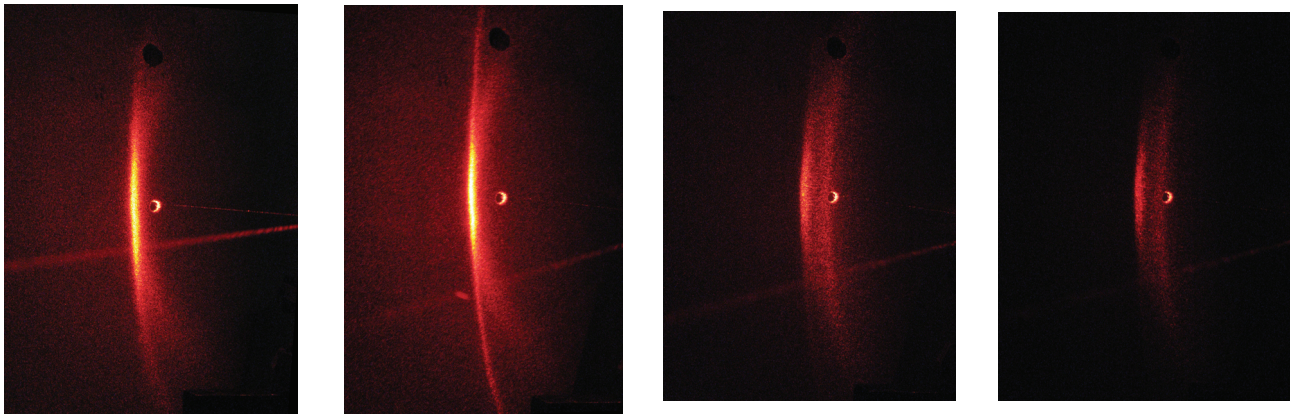

a *b* *c* *d*

Fig.2. Photographs of diffraction reflections obtained in scheme Fig.1b. In each photograph there is an aperture in the screen and vertically elongated diffraction reflections to the left of the aperture. a) The beam intensity $I = 0.75$ W/cm^2, exposure $H = 56.6$ kJ/cm^2, the test beam is focused to the center of the irradiated spot on the sample. b) $I = 7.45$ W/cm^2, $H = 58.1$ kJ/cm^2, the center of the irradiated spot. c,d) consecutive change in diffraction pattern shown in Fig.2b when shifting the test beam from the center to periphery of the spot.

of the laser wave there is $\alpha = 0$, hence $k_x = 0$, and from (1) we obtain

$$\vec{K} = \pm\vec{\beta}\ , \qquad (2)$$

i.e. the wave vector of the interference pattern is determined by a 'set' of **β** vectors of the waveguide modes. A vector **β** can be directed anywhere in the waveguide layer plane because of scattering process, therefore the ends of all the vectors **K** plotted from the point of origin in the wave vector space is a circle of radius **β**. Directions of the greatest probability of scattering of TE_0 waveguide mode are perpendicular to the polarization vector $\mathbf{E}_0$ of the incident laser wave, so the 'set' of the vectors **β** and **K** is concentrated around these directions.

Since the AgCl–Ag system is photosensitive, interference patterns are recorded as gratings with 'fan'-like vectors **K**. In this case the spatial period of the gratings corresponds to the spatial period (wavelength) of the waveguide modes because of (2).

When observing diffraction from the SG in autocollimation scheme on the screen, one can see diffraction reflections from the SG demonstrating the 'fan'-like gratings. These reflections provide information both on propagation constant of waveguide modes and spread of directions of the wave vectors **β** whose appearance caused development of the SG.

Photographs in Fig.2a,b display the diffraction reflections from the SG recorded in centers of irradiated spots at different intensities of the laser beam and approximately the same energy doses. The difference in diffraction reflection brightness indicates the difference in the amplitude of the scattered waveguide modes, and their different positions (different distances to the aperture in the screen) indicate different radii of circles, i.e. the value of propagation constant β of waveguide modes depends on intensity of the incident beam.

When shifting the focused test laser beam from the center of the spot (see Fig.2b) to the periphery of the same spot (see Fig.2c,d), we can clearly see that diffraction reflection acquires double structure. We associate such a structure with manifestation of spatial bistability affecting formation of SG.

Discussion

It is possible to describe the effect of bistability on the basis of analogy of the spatial problem of waveguide mode excitation inside a film with a grating and the problem of forced oscillations of a harmonic oscillator in time, see Fig.3.

If a pump wave *s* falls on a waveguide with a grating, its field is modulated with the spatial frequency of the grating $\beta_S = 2\pi/d$ where *d* is the grating period. The modulated field of the incident wave $s = Se^{-i\beta_S x}$ acts as a driving force for the field of the waveguide mode *a* in the film, resulting in developing of a waveguide mode $a = Ae^{-i\beta_S x}$ with forced spatial frequency β_S. However, the waveguide mode has its 'own' resonance frequency $\beta_0(1-k\,|a\,|^2)$ with attenuation factor γ. The multiplier $(1-k\,|a\,|^2)$ with nonlinearity coefficient *k* takes into account dependence of the resonant propagation constant β_0 of the waveguide mode on the value of mode amplitude $|a|$, as it follows from Fig.2. As a result, we can write down the equation for coupled modes *a* and *s* [6]:

$$\frac{\mathrm{d}a}{\mathrm{d}x} = \left[-i\beta_0\left(1-k|a|^2\right)-\gamma\right]a + qs\,, \qquad (3)$$

where *q* is coupling coefficient for waves *a* and *s*. We look

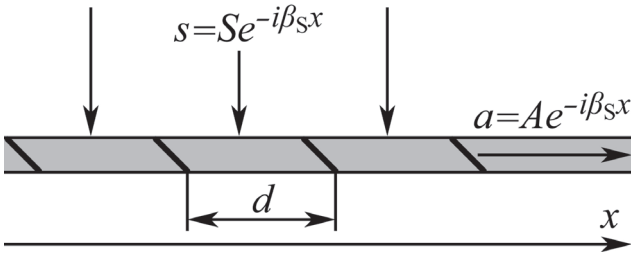

Fig.3. The scheme of spatial connection of the wave s incident on the waveguide (gray bar) with waveguide mode a through the grating with spatial frequency $\beta_S = 2\pi/d$. SG strokes are black oblique lines in the waveguide.

for a 'stationary' solution in the form $s = Se^{-i\beta_S x}$, $a = Ae^{-i\beta_S x}$, therefore

$$\begin{aligned} -i\beta_S Ae^{-i\beta_S x} &= \left[-i\beta_0\left(1-k|a|^2\right)-\gamma\right]Ae^{-i\beta_S x} + \\ +qSe^{-i\beta_S x}&\left\{-i\left[\beta_S-\beta_0\left(1-k|a|^2\right)\right]+\gamma\right\}A = qS \end{aligned}. \quad (4)$$

Similar equation must be true for the complex conjugate form, i.e.

$$\left\{i\left[\beta_S-\beta_0\left(1-k|a|^2\right)\right]+\gamma\right\}A^* = q^*S^*. \quad (5)$$

By multiplying (4) and (5), we obtain

$$\left\{\left[\beta_S-\beta_0\left(1-k|a|^2\right)\right]^2+\gamma^2\right\}|A|^2 = |qS|^2 \quad (6)$$

We introduce new variables: $I_{wm} = |A|^2 \geq 0$ is field intensity of the waveguide mode; $I_{pw} = |qS|^2 \geq 0$ is intensity of the external pump wave, at the expense of which the intensity of the waveguide mode increases, see (3). Thus (6) can be rewritten as

$$I_{pw}\left(I_{wm}\right) = I_{wm}\begin{bmatrix} k^2\beta_0^2 I_{wm}^2 + \\ +2k\beta_0\left(\beta_S-\beta_0\right)I_{wm} + \\ +\left(\beta_S-\beta_0\right)^2+\gamma^2 \end{bmatrix}. \quad (7)$$

This is a cubic equation for I_{wm}, and the shape of this curve is qualitatively shown in Fig.4 as an inverse dependence $I_{wm}(I_{pw})$.

Provided the external wave intensity is low (hence the nonlinearity may be neglected), low-intensity waveguide mode *a* is excited in the waveguide film due to the external wave *s* diffraction on the grating:

$$I_{wm} = \frac{I_{pw}}{\left(\beta_S-\beta_0\right)^2+\gamma^2}. \quad (8)$$

Dependence $I_{pw}(I_{wm})$ may be studied concerning extremums. Solving the quadratic equation in I_{wm}, obtained by equating $I'_{pw}\left(I_{wm}\right)$ to zero yields values

$$I_{wm1,2} = \frac{\left(\beta_0-\beta_S\right)^2}{3k\beta_0}\left(2 \pm \sqrt{1-\frac{3\gamma^2}{\left(\beta_0-\beta_S\right)^2}}\right). \quad (9)$$

I_{wm1} value provides the largest intensity of waveguide mode on the lower branch in Fig.4, and I_{wm2} provides the smallest one on the top branch.

At values $I_{pw} \in [I_{pw2}, I_{pw1}]$ (see Fig.4) waveguide modes with two intensity levels can be excited, which corresponds to bistability. Intermediate branch is unstable, and the states corresponding to it can not be realized [6].

Assuming absorption to be low, which means $\gamma \to 0$, we get

$$I_{wm1} \approx \frac{\beta_0-\beta_S}{3k\beta_0},\ I_{wm2} \approx \frac{\beta_0-\beta_S}{k\beta_0}. \quad (10)$$

Thus, the excitation levels of waveguide modes should differ about 3 times or more, as is observed in the images of double diffraction reflections in Fig.2c,d.

Since it is assumed that the resonant value of the propagation constant is determined as $\beta_0(1-kI_{wm})$, as it follows from (10), we obtain two values for the resonant propagation constants of the waveguide modes. The propagation constant $\beta_2 = \beta_S$ corresponds to I_{wm2} intensity level, i.e. the upper branch in Fig.4, and $\beta_1 = (2\beta_0+\beta_S)/3$ corresponds to the I_{wm1} intensity level, i.e. the lower branch. The value of β_0 is the resonant value for the 'entry' level of excitation (see (8), i.e. for the emerging SG. Grating period values $d_0 = 2\pi/\beta_0$, $d_1 = 2\pi/\beta_1$, and $d_2 = 2\pi/\beta_2$ were calculated from angles of autocollimation diffraction and are d_0 = 385.8 nm, d_1 = 392.5 nm, and d_2 = 403.7 nm. On the other hand, using two of three experimentally measured periods, one can calculate the third period. So, from d_0 and d_2 the theoretical

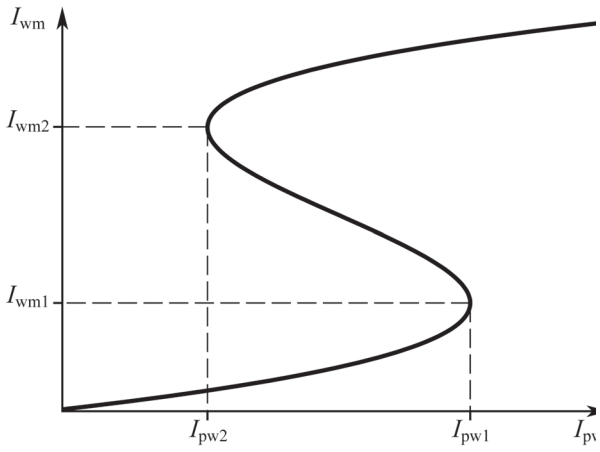

Fig.4. The qualitative form of the intensity of the waveguide mode I_{wm} on the intensity of the pump wave (laser beam) I_{pw} obtained from the equation (7).

value d_1 is

$$d_1^{\text{theor}} = \frac{6\pi}{2\beta_0 + \beta_2} = \frac{3d_0 d_2}{d_0 + 2d_2} = 391.6\,\text{nm}.$$

Divergence between d_1^{theor} and d_1 is less than 1 nm. This result may be considered as confirmation of the hypothesis of the optical bistability as the main cause of doubling the diffraction reflections observed on Fig.2c,d.

Conclusions

In this paper, an experimental study of the parameters of the plane wave diffraction on a grating in a nonlinear waveguide was conducted, and a theoretical model has been proposed to describe them. The model is based on spatial analogy with the problem of establishing forced oscillations of a harmonic oscillator. It has been shown that at diffraction on a grating in a nonlinear optical waveguide the optical bistability effect may manifest itself in dependence of the intensity of the waveguide mode on the intensity of the external incident wave. The double structure of the diffraction reflections of spontaneous gratings recorded by laser in waveguide photosensitive AgCl–Ag films is considered as a manifestation of spatial bistability effect. The calculated values of periods and intensities of grating diffraction reflections are in accordance to those observed in the experiment.

References

1. H.M. Gibbs Optical Bistability: Controlling Light with Light. – Academic Press (1985). – 471 p.
2. G.I. Stegeman. Overview of Nonlinear Integrated Optics, in “Nonlinear Waves in Solid State Physics”, ed. by A.D. Boardman, M. Bertolotti, T. Twardowski, Springer, NATO ASI Series, 247, (1990), pp. 463–494.
3. L. A. Ageev, V. B. Blokha, V.K. Miloslavsky. Quantum Electronics (Kyiv), issue 38, p.28–56 (1990) [in Russian].
4. L.A. Ageev, V.K. Miloslavsky. Opt. Engin., 34, 4, 960–972 (1995).
5. M.J. Adams. An Introduction to Optical Waveguides. – Wiley (1981). – 401 p.
6. H.A. Haus, Waves And Fields In Optoelectronics. – Prentice-Hall, New Jersey (1984), 402 p.

Вісник ХНУ, серія «Фізика», вип. 24, 2016. с. 50-54

PACS: 61.43.Dq, 07.85.−m, 29.20.−c, 61.10.Nz, 61.80.−x, 81.70.−q
УДК 544.723; 669.788

Effect of gamma irradiation on the physical properties of melt span alloys of $Ti_{30}Zr_{45}Ni_{25}$

O.E. Dmytrenko, I.V. Kolodiy, V.I. Dubinko

National Science Center "Kharkov Institute of Physics and Technology"
Kharkov 61108, Ukraine

Gamma irradiation of the melt span samples of $Ti_{30}Zr_{45}Ni_{25}$ up to the dose of 10^4 rad did not result in any substantial changes of their physical properties (micro hardness and electric resistivity), which is consistent with a high degree of disorder in the initial microstructure that does not change significantly under irradiation. The present results show that these materials can be considered as radiation resistant hydrogen absorbers (HABs) for the mitigation of hydrogen hazards in severe accidents in nuclear power plants.
Keywords: hydrogen absorption, amorphous alloys, Laves phase, irradiation.

Гамма-опромінення зразків швидко загартованого сплаву $Ti_{30}Zr_{45}Ni_{25}$ до дози 10^4 рад не призводить до суттєвих змін їх фізичних властивостей (мікротвердості і питомого електричного опору), що узгоджується з високим ступенем безладу в вихідної мікроструктурі, яка не зазнає суттєвих змін при опроміненні. Представлені результати показують, що ці матеріали можуть розглядатися в якості радіаційно-стійких водневих поглиначів для зменшення ризиків, пов'язаних з витоком водню в аварійних умовах на атомних електростанціях.
Ключові слова: поглинання водню, аморфні сплави, фази Лавеса, опромінення.

Гамма-облучение образцов быстро закаленного сплава $Ti_{30}Zr_{45}Ni_{25}$ до дозы 10^4 рад не приводит к существенным изменениям их физических свойств (микротвердости и удельного электрического сопротивления), что согласуется с высокой степенью беспорядка в исходной микроструктуре, которая существенно не изменяется при облучении. Представленные результаты показывают, что эти материалы могут рассматриваться в качестве радиационно-стойких водородных поглотителей для уменьшения рисков, связанных с утечкой водорода в аварийных условиях на атомных электростанциях.
Ключевые слова: поглощение водорода, аморфные сплавы, фазы Лавеса, облучение.

Introduction

One of the most important issues of the nuclear power plants operation is the mitigation of hydrogen hazards in severe accidents in nuclear power plants. To avoid severe damage of the containment and thus loose the confinement function for radioactivity release some hydrogen control and risk mitigation measures exist [1]. In particular, passive auto catalytic recombiners (PARs) have been developed and have become commercially available in the last decades. PARs are simple devices, consisting of catalyst surfaces arranged in an open-ended enclosure. In the presence of hydrogen (with available oxygen), a catalytic reaction occurs spontaneously at the catalyst surface and the heat of reaction produces natural convection flow through the enclosure, exhausting the warm, humid hydrogen depleted air and drawing fresh gas from below. Thus, PARs do not need external power or operator action. However, PAR capacities are ultimately subject to mass transfer limitations and may not keep up with high hydrogen rates in some scenarios so that flammability limits can be reached or exceeded (e.g. in the immediate vicinity of the hydrogen release). Thus, working in high concentrations (>8%) can initiate deflagration in the PARs due to the hot surfaces of the catalyst, which shows the need for research to create other means of hydrogen removal in addition to PARs, which is addressed in the present paper.

It is known that some metals and alloys can be very strong hydrogen absorbers (**HAB**s), and the rate and efficiency of hydrogen absorption depends strongly on temperature and material structure. Therefore HABs can be used in some scenarios where PAR capacities are not sufficient, such as high hydrogen concentrations or places where exothermic reactions taking place at PAR surfaces are not desirable. In this respect, **melt span alloys** of Ti-Zr-Ni may present a good alternative, since, according to our research, they can absorb large quantities of hydrogen (up to 1.7 wt%) without producing extra heat [2, 3]. Their absorption capacity and rate strongly depend on temperature and show the best characteristics between 400 and 500 °C, and so HABs made from these alloys can be used in the hot areas of the reactor. Application of a thin Pd coating dramatically reduces the loading time and

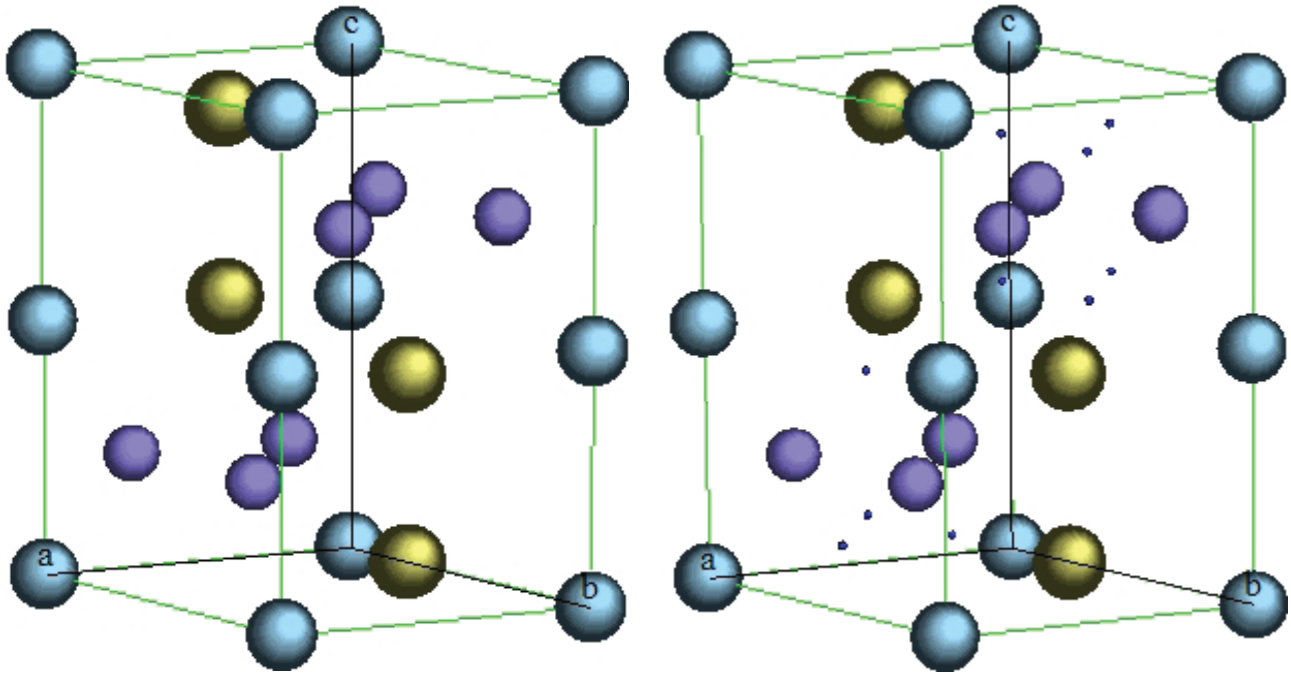

a *b*

Fig. 1. Crystal structure of the L-TiZrNi phase before hydrogenation (a) and L-TiZrNi$H_{2.12}$ after hydrogenation (b).

enables absorption at room temperature [4], which shows the potential of these materials as HABs for power plant applications.

One of the main questions concerning the applications of melt spun alloys with a complex structure as HABs for nuclear power plants is their *stability under irradiation*. The main constituent of the irradiation fields in nuclear power plants are gammas which are hard to shield. Few existing studies of the effect on gamma irradiation on **$Ti_{41,5}Zr_{41,5}Ni_{17}$ and $Ti_{41,5}Hf_{41,5}Ni_{17}$** quasicrystals have shown their resistance to the radiation-induced phase transitions in the dose range up to 10000 rad [5]. In the present study we investigate the effect of gamma irradiation on the physical properties of $Ti_{30}Zr_{45}Ni_{25}$ melt spun alloys, which demonstrate high absorption rate and capacity due to a large fraction of amorphous phase in the initial state prior to irradiation.

In the following section, the structure and hydrogen absorption kinetics of $Ti_{30}Zr_{45}Ni_{25}$ melt spun alloys are presented. In section 3, the gamma irradiation setup of the $Ti_{30}Zr_{45}Ni_{25}$ samples is described, and the effect of irradiation on their micro hardness and electric resistivity is presented.

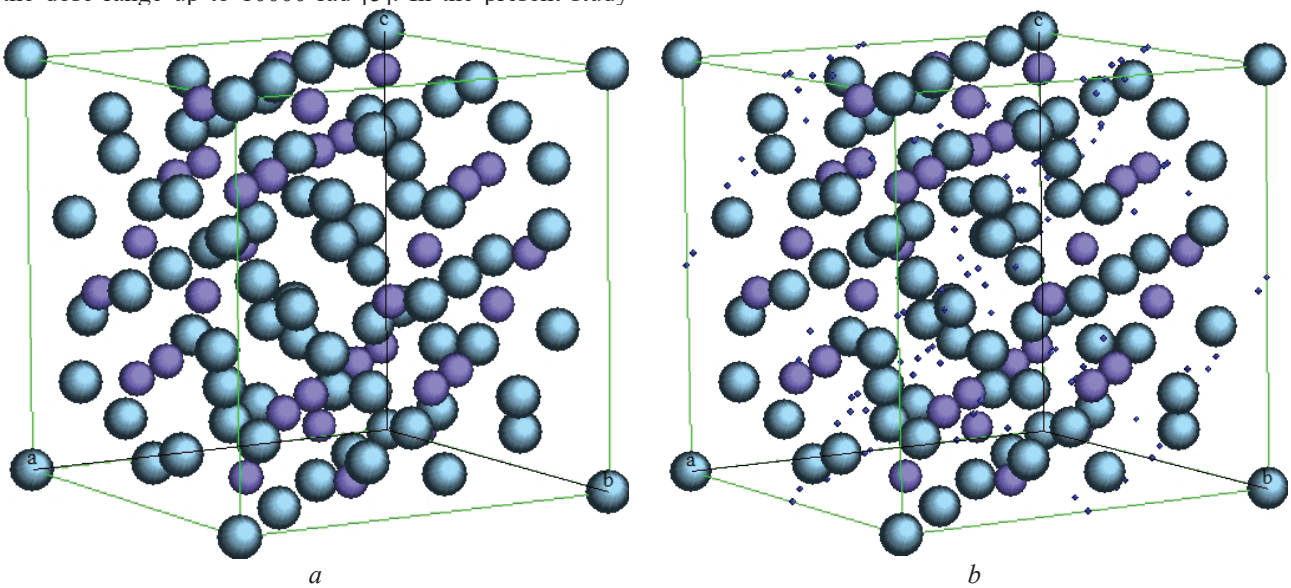

a *b*

Fig. 2. Crystal structure of the $(Ti,Zr)_2Ni$ phase before hydrogenation (a) and $(Ti,Zr)_2NiH_{2,5}$ after hydrogenation (b).

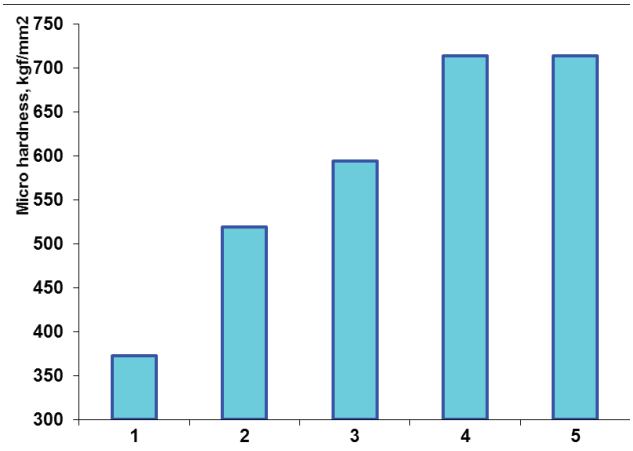

Fig. 3. Micro hardness of $Ti_{30}Zr_{45}Ni_{25}$ in different states [2] : 1 – crystalline ingot; 2 – melt span films before hydrogenation; 3- melt span films after hydrogenation at 400 °C; 4- melt span films after hydrogenation at 450 °C; 5- melt span films after hydrogenation at 500 °C.

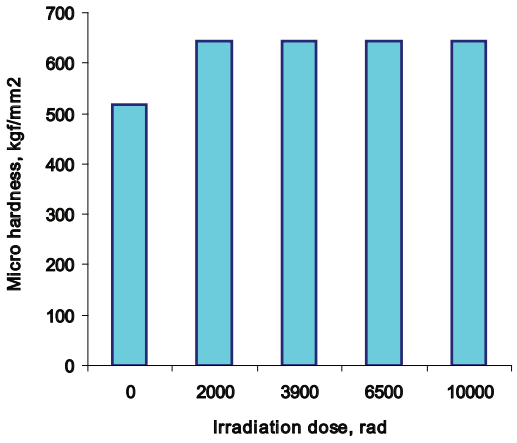

Fig. 4. Micro hardness of the melt span samples after different irradiation doses.

Structure and hydrogen absorption properties of $Ti_{30}Zr_{45}Ni_{25}$

Ingots of $Ti_{30}Zr_{45}Ni_{25}$ were made of iodine Ti (99,98%), iodine Zr (99,98%) and electrolytic Ni (99,99%) in the arc furnace with tungsten electrode in the Ar atmosphere. Melt span films of thickness 40÷60 microns were obtained at the cooling rate of 10^5 K/s [2]. The microstructure of as-received and hydrogenated samples was analyzed means of X-ray diffraction at XRD installation DRON-4-07 and scanning electron microscope QUANTA 200 3 D with micro-analyzer Pegasus 2000.

Ingots of $Ti_{30}Zr_{45}Ni_{25}$ contain two phases. 98 wt% is occupied by hexagonal Laves phase L-TiZrNi (C14, $MgZn_2$ type [6]) shown in Fig. 1a. Its lattice parameters are **a** = 5,2250Å, **c** = 8,5509Å, and the elementary cell volume **V** = 202,17Å^3. The remaining 2 wt% is taken by the α-(Ti,Zr) based solid solution.

After melt spinning, the main phase L-TiZrNi retained its geometry with somewhat increased lattice parameters: **a** = 5,2294Å; **c** = 8,5621Å, **V** = 202,78 Å^3, and decreased fraction - 86.2 wt%. Additional cubic phase occupying 13.8 wt% was formed by melt spinning - $(Ti,Zr)_2Ni$, with **a** = 11,913Å; **V** = 1690,69Å^3, which is mediated by 0.132 wt% of oxygen present in the matrix (Fig. 2).

Hydrogenation of samples was done for 4 hours in a heated vacuumed chamber under initial hydrogen pressure of 0.5 bar at 400 °C , 450 °C and 500 °C [2]. The maximum hydrogen content of 1.3 wt% was achieved at 450 °C, which resulted in a significant increase of micro-hardness from 520 to 700 kgf/mm^2 (Fig. 3).

Analysis of the microstructure of samples hydrogenated at 400 °C for 4 hours has shown that it consists of three phases. The main one (82 wt%) is the hydride of the Laves phase L-$TiZrNiH_{2.12}$ (Fig. 1b) with increased volume: **a** = 5,4280Å; **c** = 8,9191Å, **V** = 227,58Å^3. The second phase (9.6 wt%) is $(Ti,Zr)_2NiH_{2,3}$ with **a** = 12,586Å **V** = 1993,72Å^3 (Fig. 2b) and the third phase (8.4 wt%) $(Ti,Zr)_4Ni_2O$ with **a** = 11,398Å, **V** = 1480,76 Å^3. The relative increase of the volume of the first two phases, $\Delta V/V$ = 12,7% and 17,9%, respectively, corresponds to the accumulation of hydrogen in them.

Elementary cell of L-$TiZrNiH_{2.12}$ consists 12 metal atoms and 10.5 hydrogen atoms that fill about 20% of the vacant hydrogen positions. At 100% occupancy one would have the phase L-$TiZrNiH_{12}$ with 48 hydrogen atoms per 12 metal atoms, i.e. with exceedingly high ratio H:M = 4:1. On the other hand, the maximum hydrogen occupancy in the second phase $(Ti,Zr)_2NiH_4$ is 128 H per 224 positions amounting to the maximum ratio H:M = 4:3. It means that for the best performance of this material as the hydrogen absorber, we need to get rid of oxygen in the system, which mediates the transformation of L-TiZrNi into $(Ti,Zr)_2Ni$.

Effect of gamma irradiation on $Ti_{30}Zr_{45}Ni_{25}$

Gamma irradiation of the samples was done by *Bremsstrahlung* gammas produced by 350÷500 keV electrons from the impulse electron accelerator passing

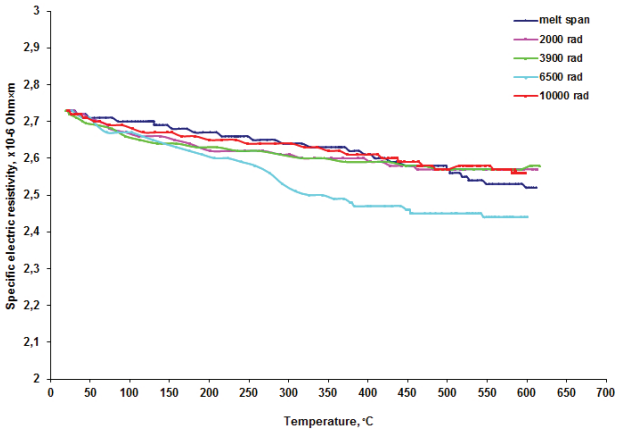

Fig. 5. Specific electric resistivity of melt span samples after different irradiation doses.

through a molybdenum converter. The electron beam current in the impulse was ~ 2÷5 kA and the impulse duration ~ (1.5÷5) 10^{-6} s. The dose rate of gamma irradiation was ~ (3.5÷5) 10^{8} rad/s.

The micro hardness of the melt span $Ti_{30}Zr_{45}Ni_{25}$ samples increases after irradiation from 520 to 700 kgf/mm^2 (Fig. 4). However, the effect quickly saturates and does not seem to depend on the irradiation dose, which may be due to the random nature of the microstructure change with increasing irradiation dose. Similarly, there is no clear tendency in the change of electric resistance of the samples with increasing irradiation dose (Fig. 5), which seems to confirm this hypothesis.

Conclusions and outlook

Hydrogenation of the melt span samples of $Ti_{30}Zr_{45}Ni_{25}$ results in formation of two phases: L-$TiZrNiH_{2.12}$ and $(Ti,Zr)_2NiH_4$. The former phase has a potential to absorb up to 4 H atoms per a metal atom. On the other hand, the maximum hydrogen occupancy in the second phase 4:3. It means that for the best performance of this material as the hydrogen absorber, we need to get rid of oxygen in the system, which mediates the transformation of L-TiZrNi into $(Ti,Zr)_2Ni$.

Gamma irradiation of the melt span samples of $Ti_{30}Zr_{45}Ni_{25}$ did not result in any substantial changes of their physical properties (micro hardness and electric resistivity) with increasing irradiation dose up to 10^4 rad, which is consistent with a high degree of disorder in the microstructure that does not change significantly under irradiation.

The present studies have been done on materials *after* irradiation. However, the problem needs further investigations, especially under *in situ* irradiation, which is hardly possible to do under reactor conditions due to obvious technical problems. Existing reports on the hydrogen behavior in metals under *in situ* electron irradiation [7] conclude that *"excitation of vibrations occurs in the hydrogen subsystem"* which greatly accelerates diffusion and release of hydrogen isotopes from metals at low temperature. The main constituent of the irradiation fields in nuclear power plants are gammas which are hard to shield as compared to electrons. Gammas are converted *inside the material* into electrons of the same energies due to the photoelectric effect and ultimately result in radiation-induced formation of defects and *localized atomic vibrations* (LAVs). The existence of LAVs, known also as *discrete breathers*, has been demonstrated in solids of different types and structures ranging from metals to insulators and from crystals to amorphous medium [8-12]. Recently the interest of researchers has extended to the study of the role of LAVs in solid state physics and their impact on the reaction rates in non-equilibrium conditions, such as exposure to irradiation, oscillating magnetic field, temperature and stress gradients [13-18]. We expect that LAVs produced in may catalyze various reactions, including the hydrogen diffusion and storage. These processes will be investigated in in a subsequent paper.

References

1. IAEA-TECDOC-1661. *Mitigation of hydrogen hazards in severe accidents in Nuclear Power Plants* http://www-pub.iaea.org/MTCD/publications/PDF/TE_1661_Web.pdf.
2. Yi.P. Bobrov, O.M. Bovda, O.E. Dmytrenko, *Hydrogen absorption-desorption behavior of melt-spun $Ti_{30}Zr_{45}Ni_{25}$ alloy.* Metallofizika i Noveyshye Tekhnologii 30 (2008) 329-336.
3. R.V. Azhazha, Yu.P. Bobrov, A.M. Bovda, A.E. Dmitrenko, *Research of processes of sorption-desorption of hydrogen from the rapidly quenched alloys of the Ti-Zr-Ni system.* VANT 17 (2008) 129-132.
4. J.Y. Kim, P.C. Gibbons , K.F. Kelton, *Hydrogenation of Pd-coated samples of the Ti–Zr-based icosahedral phase and related crystalline phases*, J. Alloys and Compounds 266 (1998) 311–317.
5. V.M. Azhazha, .D. Lavrinenko, Yu.F. Lonin, M.M. Pylypenko, B.V. Sereda, S.V. Kryachko,S.V. Malykhin, A.T. Pugachov, M.V. Reshetnyak, Changes of structure characteristics in Ti41,5Zr41,5Ni17 and Ti41,5Hf41,5Ni17 rapidly quenched ribbons under radiation influence, VANT, #2/97 (2011) 33-38.
6. E.H. Majzoubyz, R.G.Hennig and K.F. Kelton. *Rietveld refinement and ab initio calculations of a C14-like Laves phase in Ti-Zr-Ni*, Philosophical magazine letters, 83 (2003) 65–71.
7. I. P. Chernov, Yu. M. Koroteev., V. M. Silkin, Yu. I. Tyurin *Excitation of Hydrogen Subsystem in Metals by External Influence*, Proc. 8th Int. Workshop on Anomalies in Hydrogen / Deuterium Loaded Metals, (2007) p. 27-37.
8. J. F. R. Archilla, J. Cuevas, M. D. Alba, M. Naranjo, J. M. Trillo, *Discrete breathers for understanding reconstructive mineral processes at low temperatures*, J. Phys. Chem. B**110** (2006) 24112-24120.
9. M. Haas, V. Hizhnyakov, A. Shelkan, M. Klopov, *Prediction of high-frequency intrinsic localized modes in Ni and Nb*, Phys. Rev. B, **84** (2011) 144303-1-8.
10. V. Hizhnyakov, M. Haas, A. Shelkan, M. Klopov, *Theory and molecular dynamics simulations of intrinsic localized modes and defect formation in solids,* Phys. Scr. **89** (2014) 044003-1-5.
11. L.Z. Khadeeva, S.V. Dmitriev, *Discrete breathers in crystals with NaCl structure*, Phys. Rev. B **81** (2010) 214306-1-8.
12. M.E. Manley, *Impact of intrinsic localized modes of atomic motion on materials properties*, Acta Materialia, **58** (2010) 2926-2935.
13. V. I. Dubinko, P. A. Selyshchev, and J. F. R. Archilla, *Reaction-rate theory with account of the crystal anharmonicity*, Phys. Rev. E **83** (2011) No 4, doi: 10.1103/PhysRevE.83.041124.
14. V.I. Dubinko, F.M. Russell, *Radiation damage and recovery due to the interaction of crystal defects with anharmonic lattice excitations*, J. Nuclear Materials, 419 (2011) 378-385.
15. V. I. Dubinko, A. V. Dubinko, *Modification of reaction rates under irradiation of crystalline solids: contribution from intrinsic localized modes*, Nuclear Inst. and Methods in Physics Research, B **303** (2013) 133–135.
16. V.I. Dubinko, F. Piazza, *On the role of disorder in catalysis driven by discrete breathers*, Letters on Materials (2014), 4 (2014) 273-278.
17. V. I. Dubinko, J. F. R. Archilla, S. V. Dmitriev, V. Hizhnyakov: *Rate theory of acceleration of defect annealing driven by discrete breathers*. In: J.F.R. Archilla, N. Jiménez, Sánchez-Morcillo, L.M. García-Raffi (eds.) Quodons in mica: nonlinear localized travelling excitations in crystals. Springer (2015).
18. D. Terentyev, A. Dubinko, V. Dubinko, S. Dmitriev, E. Zhurkin, *Interaction of discrete breathers with primary lattice defects in bcc Fe*. Modelling Simul. Mater. Sci. Eng. 23 (2015) 085007-085030.

Вісник ХНУ, серія «Фізика», вип. 24, 2016. с. 55-59

UDK 530.122, 514.823, 523.163
PACS 95.30.Sf, 98.62.Sb

Estimating the number of solutions equation of N-point gravitational lenses algebraic geometry methods

A.T. Kotvytskiy[1], S.D. Bronza[2], S.R. Vovk[3]

V.N.Karazin Kharkov National University, Ukraine[1,3]
Ukrainian State University of Railway Transport[1,2]
kotvytskiy@gmail.com[1], bronza_semen@mail.ua[2]

One of the main problems in the study of system of equations of the gravitational lens, is the computation of coordinates from the known position of the source.

In the process of computing finds the solution of equations with two unknowns. The difficulty lies in the fact that, in general, is not known constructive or analytical algorithm for solving systems of polynomial equations In this connection, use numerical methods like the method of tracing.

For the N-point gravitational lenses have a system of polynomial equations. Systems Research is advisable to start with an assessment of the number of solutions. This can be done by methods of algebraic geometry.

Keywords: gravitational lenses, algebraic geometry, Bézout's theorem.

Однією з основних завдань, при дослідженні системи рівнянь гравітаційної лінзи, є обчислення координат зображення за відомим положенням джерела.

У процесі обчислень доводиться знаходити рішення системи рівнянь з двома невідомими. Складність полягає в тому, що в загальному випадку не відомий конструктивний або аналітичний алгоритм для вирішення систем нелінійних рівнянь. У зв'язку з цим вдаються до чисельних методів подібним методу трасування.

У разі N-точкових гравітаційних лінз система рівнянь є полиномиальной. Дослідження такої системи доцільно почати з оцінки числа рішень. Ми проводимо це дослідження методами алгебраїчної геометрії.

Ключові слова: гравітаційні лінзи, алгебраїчна геометрія, теорема Безу.

Одной из основных задач, при исследовании системы уравнений гравитационной линзы, есть вычисление координат изображения по известному положению источника.

В процессе вычислений приходится находить решение системы уравнений с двумя неизвестными. Трудность состоит в том, что в общем случае не известен конструктивный или аналитический алгоритм для решения систем нелинейных уравнений. В связи с этим прибегают к численным методам подобным методу трассировки.

В случае N-точечных гравитационных линз система уравнений является полиномиальной. Исследование такой системы целесообразно начать с оценки числа решений. Мы проводим данное исследование методами алгебраической геометрии.

Ключевые слова: гравитационные линзы, алгебраическая геометрия, теорема Безу.

Introduction

According to the general theory of relativity, the light beam, which passes close to a point source of gravity (gravitational lens) at a distance ξ from it (in case $\xi >> r_g$) is deflected by an angle

$$\vec{\alpha} = \frac{2 \cdot r_g}{\xi^2} \vec{\xi} = \frac{4 \cdot G \cdot M}{c^2 \cdot \xi^2} \vec{\xi}, \qquad (1)$$

where r_g - gravitational radius; M - mass point of the lens; G - gravity constant; c - velocity of light in vacuum.

The detailed derivation of the formula (1) can be found in many classic books [1-3]. For N - point of the gravitational lens, in the case of small tilt angles have the following equation in dimensionless variables [4], [5]:

$$\vec{y} = \vec{x} - \sum_i m_i \frac{\vec{x} - \vec{l}_i}{\left| \vec{x} - \vec{l}_i \right|^2}, \qquad (2)$$

where $\vec{l}_i$ - dimensionless radius vector of point masses outside the lens, and the mass m_i satisfy the relation $\Sigma m_i = 1$.

The Equation (2) in coordinate form has the form of system:

$$\begin{cases} y_1 = x_1 - \sum_{i=1}^{N} m_i \dfrac{x_1 - a_i}{(x_1 - a_i)^2 + (x_2 - b_i)^2} \\ y_2 = x_2 - \sum_{i=1}^{N} m_i \dfrac{x_2 - b_i}{(x_1 - a_i)^2 + (x_2 - b_i)^2} \end{cases}, \quad (3)$$

where a_i and b_i are the coordinates of the radius-vector $\vec{l}_i$, i.e. $\vec{l}_i = (a_i, b_i)$.

The right parts the equations of system (3), are rational functions of the variables x_1 and x_2. We transform each equation of the system (3) in a polynomial equation, and we obtain a system of equations:

$$\begin{cases} F_1(x_1, x_2, y_1) = 0 \\ F_2(x_1, x_2, y_2) = 0 \end{cases}, \quad (4)$$

To study the solutions of the system (4), it will be convenient methods of algebraic geometry.

Indeed, the main object of study of classical algebraic geometry, as well as in a broad sense and modern algebraic geometry, are the set of solutions of algebraic systems, in particular polynomial, equations. This situation gives us the opportunity to apply the techniques of algebraic geometry in the theory of *N*-point gravitational lenses [6] - [9].

Most of the results that we need stated in terms of homogeneous coordinates to projective curves that are defined in the projective plane.

Therefore, we need, in the beginning, the system transform (4) to a form convenient for evaluation. To transform the system (4) we need the following terms and definitions.

Mathematical definitions and theorems

Before that provide definitions, we describe the projective plane and homogeneous (projective) coordinates. The real projective plane can be thought of as the Euclidean plane with additional points added, which are called points at infinity, and are considered to lie on a new line, the line at infinity. There is a point at infinity corresponding to each direction (numerically given by the slope of a line), informally defined as the limit of a point that moves in that direction away from the origin. Parallel lines in the Euclidean plane are said to intersect at a point at infinity corresponding to their common direction. Given a point (x, y) on the Euclidean plane, for any non-zero real number S, the triple (xS, yS, S) is called a set of homogeneous coordinates for the point. By this definition, multiplying the three homogeneous coordinates by a common, non-zero factor gives a new set of homogeneous coordinates for the same point. In particular, $(1,2)$ is such a system of homogeneous coordinates for the point (x, y). For example, the Cartesian point $(x, y, 1)$ can be represented in homogeneous coordinates as $(1,2.1)$ or $(2,4.2)$. The original Cartesian coordinates are recovered by dividing the first two positions by the third. Thus unlike Cartesian coordinates, a single point can be represented by infinitely many homogeneous coordinates.

Some authors use different notations for homogeneous coordinates which help distinguish them from Cartesian coordinates. The use of colons instead of commas, for example $(x : y : z)$ instead of (x, y, z), emphasizes that the coordinates are to be considered ratios [10]. Square brackets, as in $[x, y, z]$ emphasize that multiple sets of coordinates are associated with a single point [11]. Some authors use a combination of colons and square brackets, as in $[x : y : z]$ [12].

The properties of homogeneous coordinates on the plane:

We define homogeneous projective coordinates for the first points of the projective plane not lying on a straight ∞.

At all points of the projective plane, in addition to lying on a straight ∞ (the line at infinity) are homogeneous coordinates of the projective: three numbers, not both zero.

The basic points for arithmetization projective plane (i.e., the introduction of non-homogeneous projective coordinates) are the origin Systems; ∞_x (infinity on the x-axis), ∞_y (infinity on the y-axis), $(1,1)$ - unit. Obviously, the line at infinity passes through the points ∞_x and ∞_y.

We give a precise definition. Homogeneous coordinates of a point M is said to be three numbers X_1, X_2, X_3, not both zero and such that $X_1 / X_3 = x$; $X_2 / X_3 = y$, where x and y - projective heterogeneous (affine) position. Homogeneous coordinates of points M_∞ lying on a line, ∞, call three numbers

X_1, X_2, X_3 under conditions:

1. $X_3 = 0$;

2. Of two numbers X_1, X_2 is at least one non-zero;

3. The ratio X_1 / X_2 is equal to $B/(-A)$, where *A* and *B* - coefficients of each line $Ax + By + C = 0$, passing through M_∞.

Let us look at some of the properties of homogeneous coordinates in the projective plane.

1) Each point of the projective plane is the homogeneous coordinates.

2) If X_1, X_2, X_3 - homogeneous coordinates of the point *M*, then sX_1, sX_2, sX_3 (where *s* - any non-zero number), too, are homogeneous coordinates of the point *M*.

3) different points correspond to different attitudes X_1 / X_3; X_2 / X_3 their homogeneous coordinates.

4) Direct A_1A_2 - is the line at infinity - it is in homogeneous coordinates the equation $X_3 = 0$.

5) The axes have their usual equation.

6) If the equation of the line $Ax + By + C = 0$ substitute homogeneous coordinates of a point *M*, lying on the straight line ($X_1 / X_3 = x$; $X_2 / X_3 = y$), then we get: $AX_1 + BX_2 + CX_3 = 0$, linear equation in a homogeneous form (there is no free member).

7) The equation of any curve in homogeneous coordinates is a homogeneous equation, and its degree is called the degree of the curve.

8) A polynomial $g(x, y)$ of degree *k* can be turned into a homogeneous polynomial by replacing *x* with X_1 / X_3, *y* with $/$, and multiplying by $X_3{}^k$, in other words by defining.

The resulting function *P* is a polynomial so it makes sense to extend its domain to triples where $X_3 = 0$. The equation $P(X_1, X_2, X_3) = 0$ can then be thought of as the homogeneous form of $g(x, y)$, and it defines the same curve when restricted to the Euclidean plane.

Transform the system (3) into the equation system in homogeneous coordinates. We introduce the notation of homogeneous coordinates.

Let $x_1 = \frac{X_1}{X_0}$, $x_2 = \frac{X_2}{X_0}$. We have a system of equations in homogeneous coordinates:

$$\begin{cases} y_1 = \dfrac{X_1}{X_0} - \sum\limits_{i=1}^{N} m_i \dfrac{\dfrac{X_1}{X_0} - a_i}{\left(\dfrac{X_1}{X_0} - a_i\right)^2 + \left(\dfrac{X_2}{X_0} - b_i\right)^2} \\ y_2 = \dfrac{X_2}{X_0} - \sum\limits_{i=1}^{N} m_i \dfrac{x_2 - b_i}{\left(\dfrac{X_1}{X_0} - a_i\right)^2 + \left(\dfrac{X_2}{X_0} - b_i\right)^2} \end{cases} . \quad (5)$$

We transform the system (5)

$$\begin{cases} y_1 = \dfrac{X_1}{X_0} - \sum\limits_{i=1}^{N} m_i \dfrac{\left(X_1 - a_i X_0\right) X_0}{\left(X_1 - a_i X_0\right)^2 + \left(X_2 - b_i X_0\right)^2} \\ y_2 = \dfrac{X_2}{X_0} - \sum\limits_{i=1}^{N} m_i \dfrac{\left(X_2 - b_i X_0\right) X_0}{\left(X_1 - a_i X_0\right)^2 + \left(X_2 - b_i X_0\right)^2} \end{cases} . \tag{6}$$

We transform the system (6) to form: $\begin{cases} F_1\left(X_0, X_1, X_2, y_1\right) = 0 \\ F_2\left(X_0, X_1, X_2, y_2\right) = 0 \end{cases}$

$$\begin{cases} F_1\left(X_0, X_1, X_2, y_1\right) = 0 \\ F_2\left(X_0, X_1, X_2, y_2\right) = 0 \end{cases} \tag{7}$$

where F_1 $F_1\left(X_0, X_1, X_2, y_1\right)$ and $F_2 = F_2\left(X_0, X_1, X_2, y_2\right)$ - homogeneous polynomials.

In equations of system (6), under the sign of the amount we give to a common denominator. We have:

$$\begin{cases} y_1 = \dfrac{X_1}{X_0} - \dfrac{X_0 \sum\limits_{j=1}^{N} m_j \left(X_1 - a_j X_0\right) \left\{ \prod\limits_{i=1, i\neq j}^{N} \left[\left(X_1 - a_i X_0\right)^2 + \left(X_2 - b_i X_0\right)^2 \right] \right\}}{\prod\limits_{i=1}^{N} \left[\left(X_1 - a_i X_0\right)^2 + \left(X_2 - b_i X_0\right)^2 \right]} \\ y_2 = \dfrac{X_2}{X_0} - \dfrac{X_0 \sum\limits_{j=1}^{N} m_j \left(X_2 - b_j X_0\right) \left\{ \prod\limits_{i=1, i\neq j}^{N} \left[\left(X_1 - a_i X_0\right)^2 + \left(X_2 - b_i X_0\right)^2 \right] \right\}}{\prod\limits_{i=1}^{N} \left[\left(X_1 - a_i X_0\right)^2 + \left(X_2 - b_i X_0\right)^2 \right]} \end{cases} \tag{8}$$

Let denominator through:

$$L = L\left(X_0, X_1, X_2\right) = \prod_{i=1}^{N} \left[\left(X_1 - a_i X_0\right)^2 + \left(X_2 - b_i X_0\right)^2 \right].$$

Transforming further we have:

$$\begin{cases} y_1 = \dfrac{X_1}{X_0} - \dfrac{X_0 \sum\limits_{j=1}^{N} m_j \left(X_1 - a_j X_0\right) \left\{ \prod\limits_{i=1, i\neq j}^{N} \left[\left(X_1 - a_i X_0\right)^2 + \left(X_2 - b_i X_0\right)^2 \right] \right\}}{L\left(X_0, X_1, X_2\right)} \\ y_2 = \dfrac{X_2}{X_0} - \dfrac{X_0 \sum\limits_{j=1}^{N} m_j \left(X_2 - b_j X_0\right) \left\{ \prod\limits_{i=1, i\neq j}^{N} \left[\left(X_1 - a_i X_0\right)^2 + \left(X_2 - b_i X_0\right)^2 \right] \right\}}{L\left(X_0, X_1, X_2\right)} \end{cases}$$

We transform the equation to a polynomial form.

$$\begin{cases} \left(X_1 - y_1 X_0\right) L\left(X_0, X_1, X_2\right) - X_0^2 \sum\limits_{j=1}^{N} m_j \left(X_1 - a_j X_0\right) \left\{ \prod\limits_{i=1, i\neq j}^{N} \left[\left(X_1 - a_i X_0\right)^2 + \left(X_2 - b_i X_0\right)^2 \right] \right\} = 0 \\ \left(X_2 - y_2 X_0\right) L\left(X_0, X_1, X_2\right) - X_0^2 \sum\limits_{j=1}^{N} m_j \left(X_2 - b_j X_0\right) \left\{ \prod\limits_{i=1, i\neq j}^{N} \left[\left(X_1 - a_i X_0\right)^2 + \left(X_2 - b_i X_0\right)^2 \right] \right\} = 0 \end{cases} \tag{9}$$

Note that the polynomial in the left side of the first (second) equation is homogeneous.

For the degrees of these polynomials we have:

$$deg\left\{(X_1 - y_1X_0)L(X_0, X_1, X_2) - X_0^2\sum_{j=1}^{N} m_j(X_1 - a_jX_0)\left\{\prod_{i=1, i\neq j}^{N}\left[(X_1 - a_iX_0)^2 + (X_2 - b_iX_0)^2\right]\right\}\right\} = 2N+1,$$

$$deg\left\{(X_2 - y_2X_0)L(X_0, X_1, X_2) - X_0^2\sum_{j=1}^{N} m_j(X_2 - b_jX_0)\left\{\prod_{i=1, i\neq j}^{N}\left[(X_1 - a_iX_0)^2 + (X_2 - b_iX_0)^2\right]\right\}\right\} = 2N+1.$$

It's obvious that:

$$deg\, F_1 = deg\, F_2 = 2N+1. \quad (10)$$

Estimating the number of solutions of homogeneous polynomials

Let the number of solutions of (7), of course. The case in which the number of solutions endlessly, it is found out quite simple, and does not need to move to the projective coordinates, see. e.g., [6].

To estimate the number of solutions of homogeneous polynomials (7) we apply the following Bézout's theorem, see. e.g., [10], which says: that if *C* and *D* are plane curves of degrees $deg\, C = m$, $deg\, D = n$, then the number of points of intersection of *C* and *D* is $m \cdot n$, provided that

(i) the field is algebraically closed;

(ii) points of intersection are counted with the right multiplicities;

(iii) we work in to take right account of intersections 'at infinity'.

See for example [10].

Note that the equations $F_1(X_0, X_1, X_2, y_1) = 0$ and $F_2(X_0, X_1, X_2, y_2) = 0$ define two curves in the projective space, and considered over an algebraically closed field of complex numbers. Thus we are in the conditions of application of the Bézout's theorem.

Conclusions

- Number of complex solutions of equations (7), taking into account the multiplicity, in the projective plane P^2 equal $(2N+1)^2$;

-The number of real solutions of the system of equations (7), taking into account the multiplicity equal to $(2N+1)^2 - 2n$ in the projective plane P^2, where *n* - a natural number, that is less than or equal to *N*, that is $n \le N$. The last relation occurs because the systems of equations (7), although considered over the field of complex numbers, but have real coefficients. The fact, that in such equations, complex roots come in pairs.

-number $(2N+1)^2 - 2n$ - odd number. The number of real solutions of the system of equations (7), taking into account the multiplicity, in the affine plane A^2, is also equal to this number, if the curves do not intersect at infinity.

Note that each real solution of system has an obvious physical meaning: the coordinates of the point - image plane of the lens. Our results, about the oddness of the number of images are in good agreement with the theorem proved in [4], [5]. At the same time, our approach is based on the methods of algebraic geometry.

References

1. P. V. Bliokh, A. A. Minakov, Gravitational Lenses, Naukova Dumka, Kiev 1989. P. 249.
2. Weinberg S. Gravitation and Cosmology, 1972. P 657.
3. Landau L.D., Lifshitz E.M. The classical Theory of Fields, 1988, V.2 P. 512.
4. Zakharov A.F. Gravitacionnye linzy i mikrolinzy, 1997, P. 328.
5. Schneider P., Ehlers J., Falco E.E. Gravitational lenses. Springer-Verlag Berlin Heidelberg 1999 P. 560.
6. Kotvytskiy A.T., Bronza S.D. // Odessa Astronomical Publications, vol. 29 (2016), P.31-33.
7. Lang S. Algebra. Columbia University. New York, 1965. P.564.
8. Walker R.J. Algebraic curves. Pringeton. New Jersey. 1950, P. 236.
9. Van Der Waerden B.L. Algebra I,II. Achte auflage der modernen algebra Springer-Verlag Berlin Heidelberg New York 1971 P. 456.
10. Reid M. Undergraduate Algebraic Geometry. Math Inst., University of Warwick, Cambridge 1988, P. 136.
11. Garner, Lynn E. An Outline of Projective Geometry, North Holland, 1981, P.220.
12. Bocher, Maxime. Introduction to Higher Algebra. Macmillan, 1907, P.292.

ІНФОРМАЦІЯ ДЛЯ АВТОРІВ СТАТЕЙ

журналу «Вісник ХНУ». Серія «Фізика»

У журналі «Вісник ХНУ». Серія «Фізика» друкуються статті та стислі за змістом повідомлення, в яких наведені оригінальні результати теоретичних та експериментальних досліджень, а також аналітичні огляди літературних джерел з різноманітних актуальних проблем фізики за тематикою видання.

Мова статей – українська, англійська та російська.

ТЕМАТИКА ЖУРНАЛУ

1. Теоретична фізика.
2. Фізика твердого тіла.
3. Фізика низьких температур.
4. Фізика магнітних явищ.
5. Оптика та спектроскопія.
6. Загальні питання фізики і серед них: методологія та історія фізики, математичні методи фізичних досліджень, методика викладання фізики у вищій школі, техніка та методика фізичного експерименту тощо.

ВИМОГИ ДО ОФОРМЛЕННЯ РУКОПИСІВ СТАТТЕЙ

Загальний обсяг тексту рукопису статті повинен займати не більше, ніж 15 сторінок.

Рукопис статті складається з титульної сторінки, на якій вказанно: назва статті; ініціали та прізвища авторів; поштова адреса установи, в якій була виконана робота; класифікаційний індекс за системами PACS та УДК; анотації на окремому аркуші з прізвищем та ініціалами авторів і назвою статті, викладені українською, російською та англійською мовами; основний текст статті; список літератури; підписи під рисунками; таблиці; рисунки: графіки, фотознімки.

Анотація повинна бути за об'ємом не меньш ніж 500 сімволів. Стаття повинна бути структорована. Висновки потрібно пронумеровати та в них потрібні бути висновки а не переписана анотація.

Електронний варіант рукопису статті повинен відповідати таким вимогам: текст рукопису статті повинен бути набраний у форматі MicrosoftWord версії 2013, вирівнювання тексту повинне бути здійснене за лівим краєм, гарнітураTimesNewRoman, без прописних букв у назвах, букви звичайні рядкові, з полями ліворуч, праворуч, зверху і знизу по 2,5 см, формули повинні бути набрані в MathType (не нижче версії 6,5), у формулах кирилиця не допускається, символи з нижніми і верхніми індексами слід набирати в MicrosoftWord, ширина формули не більше 70 мм, графіки та фотографії необхідно подавати в графічному форматі, розрізнення не менше 300 dpi, поширення файлів повинно бути *.jpg, шириною в одну чи дві колонки, для однієї колонки розміри: завширшки 8 мм, для двох колонок – 16 мм. Масштаб на мікрофотографіях необхідно представляти у вигляді масштабної лінійки.

ВИМОГИ ДО ОФОРМЛЕННЯ ГРАФІКІВ

Товщина ліній не більше 0,5 мм, але не менше 0,18 мм. Величина літер на підписах до рисунків не більш 14 pt , але не менше 10 pt, гарнітура Arial.

ПРИКЛАД ОФОРМЛЕННЯ СПИСКУ ЛІТЕРАТУРИ

1. Л.Д. Ландау, Е.М. Лифшиц. Теория упругости, Наука, М. (1978), 730 с.
2. И.И. Іванов. ФТТ, 25, 7, 762 (1998).
3. A.D. Ashby. Phys.Rev., A19, 213 (1985).
4. D.V. Vert. In Progress in Metals, ed. by R. Speer, USA, New York (1976), v.4, p.17.

ДО РЕДАКЦІЇ НАДАЄТЬСЯ

1. Два роздруковані примірники рукопису статті, які підписані її авторами.
2. Електронна версія рукопису та дані щодо контактів для спілкування з її авторами. Для цього потрібно надіслати електронною поштою, тільки на адресу **physics.journal@karazin.ua**.
3. Направлення від установи, де була виконана робота, і акти експертизи у двох примірниках; адресу, прізвище, повне ім’я та батькові авторів; номери телефонів, E-mail, а також зазначити автора рукопису, відповідального за спілкування з редакцією журналу.

Матеріали рукопису статті потрібно направляти за адресою: Редакція журналу «Вісник Харківського національного університету імені В.Н. Каразіна. Серія: фізика», Лебедєву С.В., фізичний факультет, майдан Свободи, 4, Харківський національний університет імені В.Н. Каразіна. тел. (057)707-53-83.

Наукове видання

Вісник Харківського національного університету імени В.Н.Каразіна

Серія “Фізика”

випуск 24

Збірник наукових праць

Українською, російською та англійською мовами.

Комп’ютерне верстання С.В. Лебедєв

Підписано до друку 28.01.2017. Формат 60x84 1/8.

Папір офсетний. Друк ризограф. Ум. друк. арк. 11,9. Обл.-вид. арк 18,7.

Наклад 100 пр. Зам. №

Надруковано: ХНУ імені В.Н. Каразіна
61022, Харків, майдан Свободи, 4.
Тел.705-24-32

Свідоцтво суб'єкта видавничої справи ДК №3367 від 13.01.09